



University of Kentucky
UKnowledge

Theses and Dissertations--Plant and Soil
Sciences

Plant and Soil Sciences


2021

Topographic Gradients in Bulk Soil Properties in Central Kentucky Karst Sinkholes

Anne Kathryn McGraw

University of Kentucky, akmcgraw47@gmail.com

Author ORCID Identifier:

 <https://orcid.org/0000-0002-1070-3418>

Digital Object Identifier: <https://doi.org/10.13023/etd.2021.438>

[Right click to open a feedback form in a new tab to let us know how this document benefits you.](#)

Recommended Citation

McGraw, Anne Kathryn, "Topographic Gradients in Bulk Soil Properties in Central Kentucky Karst Sinkholes" (2021). *Theses and Dissertations--Plant and Soil Sciences*. 150.
https://uknowledge.uky.edu/pss_etds/150

This Master's Thesis is brought to you for free and open access by the Plant and Soil Sciences at UKnowledge. It has been accepted for inclusion in Theses and Dissertations--Plant and Soil Sciences by an authorized administrator of UKnowledge. For more information, please contact UKnowledge@lsv.uky.edu.

STUDENT AGREEMENT:

I represent that my thesis or dissertation and abstract are my original work. Proper attribution has been given to all outside sources. I understand that I am solely responsible for obtaining any needed copyright permissions. I have obtained needed written permission statement(s) from the owner(s) of each third-party copyrighted matter to be included in my work, allowing electronic distribution (if such use is not permitted by the fair use doctrine) which will be submitted to UKnowledge as Additional File.

I hereby grant to The University of Kentucky and its agents the irrevocable, non-exclusive, and royalty-free license to archive and make accessible my work in whole or in part in all forms of media, now or hereafter known. I agree that the document mentioned above may be made available immediately for worldwide access unless an embargo applies.

I retain all other ownership rights to the copyright of my work. I also retain the right to use in future works (such as articles or books) all or part of my work. I understand that I am free to register the copyright to my work.

REVIEW, APPROVAL AND ACCEPTANCE

The document mentioned above has been reviewed and accepted by the student's advisor, on behalf of the advisory committee, and by the Director of Graduate Studies (DGS), on behalf of the program; we verify that this is the final, approved version of the student's thesis including all changes required by the advisory committee. The undersigned agree to abide by the statements above.

Anne Kathryn McGraw, Student

Dr. Christopher Shepard, Major Professor

Dr. Ole Wendroth, Director of Graduate Studies

TOPOGRAPHIC GRADIENTS IN BULK SOIL PROPERTIES
IN CENTRAL KENTUCKY KARST SINKHOLES

THESIS

A thesis submitted in partial fulfillment of the
requirements for the degree of Master of Science in the
College of Agriculture, Food and the Environment
at the University of Kentucky

By

Anne Kathryn McGraw

Lexington, Kentucky

Director: Dr. Christopher Shepard, Assistant Professor of Critical Zone Pedology

Lexington, Kentucky

2021

Copyright © Anne Kathryn McGraw 2021
<https://orcid.org/0000-0002-1070-3418>

ABSTRACT OF THESIS

TOPOGRAPHIC GRADIENTS IN BULK SOIL PROPERTIES IN CENTRAL KENTUCKY KARST SINKHOLES

The Bluegrass physiographic region of Kentucky is underlain by the late Ordovician Lexington Limestone formation. This area has many identifiable karst features, including sinkholes. Karst sinkholes and associated soils coevolve, which may influence the distribution of bulk soil properties and storage of carbon across karst landscapes. Two sinkholes on the University of Kentucky's C. Oran Little Animal Research Center in Woodford County, central Kentucky, were selected for analysis. We described and sampled nine pedons at the dominant landscape positions (e.g., summit, shoulder, backslope, footslope, and toeslope) within the two sinkholes; we characterized the physical, chemical, and mineralogical soil properties across the hillslope gradient (i.e., toposequence). As a general trend, total carbon content decreased with sampling depth, and the toeslope and footslope positions contained higher carbon stocks relative to other landscape positions. Total carbon and silt tended to accumulate in the base of sinkholes, whereas summit positions exhibited higher clay contents and iron and aluminum oxide concentrations. The relationship between silt and carbon, and negative relationships between carbon and clay content, exchangeable Ca, and dithionite-extractable Fe and Al may suggest that the carbon in the base of these features is less likely to be minerally associated. An estimated 20% of the world's land surface is underlain by lithologies favorable for karst terrain formation making the characterization of the soil in these landscapes applicable outside of Kentucky's Inner Bluegrass. Measuring the properties of soils in karst sinkholes will allow for a better understanding of their place in karst landscapes, as well as their role in carbon cycling.

KEYWORDS: Pedology, Toposequences, Catena, Hillslope

Anne Kathryn McGraw
(Name of Student)

12/09/2021

Date

TOPOGRAPHIC GRADIENTS IN BULK SOIL PROPERTIES
IN CENTRAL KENTUCKY KARST SINKHOLES

By
Anne Kathryn McGraw

Dr. Christopher Shepard

Director of Thesis

Dr. Ole Wendroth

Director of Graduate Studies

12/09/2021

Date

DEDICATION

To Marco, my most constant companion in this endeavor.

ACKNOWLEDGMENTS

This would not have been possible without the guidance, support, and encouragement of many people. First and foremost, my advisor, Dr. Chris Shepard, who supported me throughout this entire process and stuck with me even as my confidence in myself wavered. I cannot thank him enough for his support, never-ending knowledge of soils and statistics, and calm attitude. The Shepard Critical Zone Pedology Lab would not be functional without its amazing manager, Ms. Rebecca Ramsey. Her guidance both in and out of the lab made my time at UK enjoyable and productive. Dr. Pamela Obura not only helped me with many technical aspects of my project (especially mineralogical analyses) but was also a comforting presence in the lab, always answering my questions and demonstrating a work ethic that seems almost impossible.

My committee members, Drs. Chris Matocha and Dave McNear, provided helpful insights and comments on my project. The XRD analysis of my clay slides would not have been possible without the guidance of Dr. Matocha and Martin Vandiviere; they were kind enough to let me have use of their lab space and XRD machine.

I finally thank my friends and family for their support. I especially need to thank my lab mate, Ms. Hannah Somerville. From day one she has been my partner in lab work and other shenanigans. The relationships I've built here will stay with me forever. Thank you all.

TABLE OF CONTENTS

ACKNOWLEDGMENTS.....	III
LIST OF TABLES.....	V
LIST OF FIGURES.....	VI
CHAPTER 1. INTRODUCTION.....	1
1.1 Thesis Rationale.....	1
1.2 Karst topography: formation, morphology, functioning, and geographic extent.....	2
1.2.1 Karst formation processes and morphology.....	2
1.2.2 Karst is widespread throughout the world.....	5
1.2.3 Hydrologic functioning of karst systems and relationship to soil properties.....	7
1.3 Hillslope controls on soil formation and properties.....	9
1.3.1 Influence of karst topography on pedogenesis.....	12
1.3.2 Soil carbon dynamics in karst regions.....	13
1.4 Thesis objectives.....	15
CHAPTER 2. PRESENT STUDY.....	16
2.1 Introduction.....	16
2.2 Materials and Methods.....	20
2.2.1 Study Location and Field Descriptions.....	20
2.2.2 Bulk Soil Characterization.....	23
2.2.3 Soil Mineralogy and Metal Concentrations.....	26
2.2.4 Carbon and Nitrogen Determination.....	29
2.2.5 Geospatial data and statistical analyses.....	29
2.3 Results.....	31
2.3.1 Field Descriptions and Morphology.....	31
2.3.2 Soil Properties as Function of Topography.....	37
2.3.3 Controls on total carbon, total nitrogen, and C:N ratios.....	47
2.3.4 Soil Trends with Depth.....	59
2.3.5 Clay Mineralogy.....	67
2.4 Discussion.....	73
2.4.1 Topographic Controls on Bulk Soil Properties.....	73
2.4.2 Soil Carbon Storage in Karst Environments.....	79
2.4.3 Implications for Karst Sinkhole Evolution.....	81
2.5 Conclusions.....	82
CHAPTER 3. SUMMARY.....	83
APPENDIX.....	86
REFERENCES.....	99
VITA.....	112

LIST OF TABLES

Table 1. Morphologic data for study pedons.	32
Table 2. Regression coefficients for the full PLSR model using a suite of geomorphic, chemical, and physical properties using two components.	54
Table 3. Regression coefficients for the simple PLSR model using a suite of geomorphic, chemical, and physical properties using one component.	55

LIST OF FIGURES

Figure 1. Idealized rendering of karst topography. Karst topography is highly variable and heterogeneous with extensive underground drainage systems. Sinkholes and disappearing streams are common features of karst landscapes and are direct conduits between surface and groundwater. Figure taken from USGS.	3
Figure 2. Example of a subsidence sinkhole, note the soil mantle. This sinkhole was one of the study locations of the present thesis and is located in Versailles, KY in the Inner Bluegrass Region.	4
Figure 3. Extent of karst regions in the contiguous United States. Most karst in Kentucky is formed from carbonate rocks at or near the surface. From Weary and Doctor (2014).	6
Figure 4. Idealized (A) and actual (B) hillslopes demonstrating the relative positions of the summit, shoulder, backslope, footslopes, and toeslopes.	10
Figure 5. Map of the study area. Digital elevation data from the KY Division of Geospatial Information was used in ArcMap 10.6 (ESRI, Redlands, CA).	22
Figure 6. Catena profiles with elevation (m) and marked sampling locations for both study sinkholes.	24
Figure 7. Sinkhole 1 summit profile with labeled horizons at approximate depths described in the field. ...	33
Figure 8. Sinkhole 1 toeslope profile with labeled horizons at approximate depths described in the field. ...	34
Figure 9. Sinkhole 2 summit profile with labeled horizons at approximate depths described in the field. ...	35
Figure 10. Sinkhole 2 toeslope profile with labeled horizons at approximate depths described in the field. ...	36
Figure 11. Dithionite-extractable Al (kg m^{-2}) exhibited a positive relationship with relative elevation, not supporting our second hypothesis. (Spearman's ρ : 0.45, p-value: 0.22, df: 7).	38
Figure 12. Dithionite-extractable Fe (kg m^{-2}) exhibited a positive relationship with relative elevation, which does not support our second hypothesis. (Spearman's ρ : 0.81, p-value: 0.0079, df: 7).	39
Figure 13. Dithionite-extractable Si (kg m^{-2}) exhibited a positive relationship with relative elevation (m), which did not support our second hypothesis. (Spearman's ρ : 0.83, p-value: 0.0058, df: 7).	40
Figure 14. Total C (kg m^{-2}) exhibited a negative relationship with relative elevation (m). (Spearman's ρ : -0.50, p-value: 0.17, df: 7).	41
Figure 15. Total N (kg m^{-2}) exhibited a negative relationship with relative elevation (m). (Spearman's ρ : -0.523, p-value: 0.14, df: 7).	42
Figure 16. C:N exhibited a negative relationship with relative elevation (m). (Spearman's ρ : -0.5, p-value: 0.17, df: 7).	43
Figure 17. Total clay (%) showed a positive relationship with relative elevation (m), meaning we saw more clay, in general, at the higher hillslope positions than in the base. (Spearman's ρ : 0.51, p-value: 0.16, df: 7).	44
Figure 18. Dithionite-extractable Fe (kg m^{-2}) exhibited a positive relationship with curvature (m^{-1}). Here, negative values are concave positions and positive values are convex positions. (Spearman's ρ : 0.85, p-value: 0.006, df: 7).	45
Figure 19. Dithionite-extractable Si (kg m^{-2}) exhibited a positive relationship with curvature (m^{-1}). (Spearman's ρ : 0.73, p-value: 0.031, df: 7).	46
Figure 20. Total C (kg m^{-2}) exhibited a negative relationship with dithionite-extractable Al (kg m^{-2}). This did not support our third hypothesis. (Spearman's ρ : -0.47, p-value: 0.21, Degrees of Freedom: 7).	49
Figure 21. Total C (kg m^{-2}) exhibited a negative relationship with dithionite-extractable Fe (kg m^{-2}). This did not support our third hypothesis. (Spearman's ρ : -0.55, p-value: 0.13, Degrees of Freedom: 7).	50
Figure 22. Total C (kg m^{-2}) showed a negative relationship with exchangeable Ca ($\text{cmol}_c \text{kg}^{-1}$). (Spearman's ρ : -0.08, p-value: 0.84, Degrees of Freedom: 7).	51
Figure 23. Total C (kg m^{-2}) exhibited a weak negative relationship with total clay (kg m^{-2}). (Spearman's ρ : -0.37, p-value: 0.41, Degrees of Freedom: 7).	52
Figure 25. Relationships between Fe_o/Fe_d ratios with Total C (kg m^{-2}), Total N (kg m^{-2}), and C:N ratio. ...	53
Figure 24. Relationships between Fe_p/Fe_d ratios with Total C (kg m^{-2}), Total N (kg m^{-2}), and C:N ratio. ...	53

Figure 27. Change in root mean square error of the prediction from the PLSR with the number of included components for total C, total N, and C:N for the full PLSR model. Unadjusted RMSEP (left) indicated that substantial differences in RMSEP do not occur following two components. Cross-validated RMSEP demonstrated the lowest RMSEP with included components.....	55
Figure 28. Change in r^2 with PLSR model components for the full PLSR model. Similar to RMSEP, no significant differences were observed in r^2 following two components (left). Cross-validated was greatest using two components (right).....	56
Figure 29. PLSR loadings biplot between the explanatory variables, represented as different shapes and colors, and the response variables, represented as arrows for the full PLSR model. The orientation of the arrows relative to the explanatory variables explain the positive and negative drivers of total C, total N, and C:N.....	57
Figure 30. PLSR loadings biplot for the simplified PLSR model with only variables that had coefficient values either <-0.1 or >0.1	58
Figure 31. Total C (kg m^{-2}) generally decreased with depth (cm), and was overall higher in sinkhole 2.	61
Figure 32. Total N (kg m^{-2}) generally decreased with depth (cm) and was higher in the lower hillslope positions.	62
Figure 33. C:N was generally higher in sinkhole 2, and stayed higher with depth (cm) from the soil surface at most hillslope positions.....	63
Figure 34. Total clay content (%) increased the most with depth (cm) at the summit locations of both study sinkholes.....	64
Figure 35. Dithionite-extractable Al (Al_d ; g kg^{-1}) was slightly higher in sinkhole 1, and remained relatively constant with depth (cm).....	65
Figure 36. Dithionite-extractable Fe (Fe_d ; g kg^{-1}) was much higher in sinkhole 1 with depth (cm).	66
Figure 37. Diffractogram for sinkhole 1, summit pit. Select horizons are shown with 2 treatments.	69
Figure 38. Diffractogram for sinkhole 1, toeslope pit. Select horizons with two treatments are shown.	70
Figure 39. Diffractogram for sinkhole 2, summit pit. Select horizons with two treatments are shown.	71
Figure 40. Diffractogram for sinkhole 2, toeslope pit. Select horizons with two treatments are shown.....	72
Figure 41. Depth-weighted C (%) showed a negative relationship with relative elevation (m) for both the current study sites and Prawito (1996).....	74
Figure 42. Depth-weighted clay (%) exhibited a positive relationship with relative elevation (m) for both this study's sites and the sites from Prawito (1996).	75

CHAPTER 1. INTRODUCTION

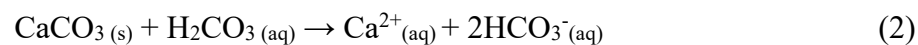
1.1 Thesis Rationale

Karst is a unique type of landscape that forms as the result of the dissolution of soluble lithologies such as limestone, dolomite, and gypsum (Ford and Williams, 2007). Karst terrain is characterized by surface and subsurface features that are generally unique to these areas: sinkholes, sinking streams, caves, and springs. These features are responsible for the high connectivity of surface- to groundwater, another characteristic of karst terrain (Rugel et al., 2016; Chen et al., 2018). Karst terrains are responsible for providing upwards of 25% of the world's drinking water, as such most research on karst systems have focused on their hydrologic functioning. A key knowledge gap in our understanding of karst systems, particularly their hydrologic functioning, is the distribution of bulk soil physical, chemical, and mineralogical properties across karst landscapes. Soil properties have a significant influence on vadose zone water dynamics and the movement of water to the epikarst and phreatic zone (Taylor and Greene, 2005). As such, quantifying the distribution of bulk soil properties is needed to better predict hydrologic functioning of these landscapes particularly under future climate change scenarios. This thesis seeks to fill this knowledge gap by characterizing the bulk soil properties across two karst features in the Inner Bluegrass region of central Kentucky. The Bluegrass physiographic region of central Kentucky (divided into the Inner and Outer Bluegrass) is an example of karst terrain with its rolling hills and fields pockmarked by vegetated depressions (Paylor and Currens, 2001) and is analogous to other humid, mesic karst regions in Kentucky and the eastern United States.

1.2 Karst topography: formation, morphology, functioning, and geographic extent

1.2.1 Karst formation processes and morphology

Karst has a unique morphology that other landscapes do not exhibit. Karst topography is characterized by the rapid dissolution of soluble lithologies, such as limestones, dolostones, gypsum, and other carbonate rocks (Dreybrodt, 1988; Ford and Williams, 2007). In general, dissolution of these soluble lithologies occurs through the action of carbonic acid (Dreybrodt, 1988). Carbonic acid (H_2CO_3) is formed through the dissolution of carbon dioxide (CO_2) into rainwater or the dissolution of respired CO_2 from plant roots and microbes and organic matter decomposition into soil water (White, 1988; Ford and Williams, 2007; Phillips, 2016). The carbonic acid, along with the release of organic acids by plants and microbes, dissolves the carbonate bedrock (Jakucs, 1977; Jennings, 1985; Dreybrodt, 1988; Gillieson, 1996). For example, dissolution of calcium carbonate (e.g., limestone) proceeds as:



Dissolution is continually occurring in karst sinkholes as long as the needed reactants are present: soluble rock, liquid water, and carbon dioxide (or other dissolution agent) (White, 1997). The products of these reactions are then leached from the system, which may leave physical voids within the bedrock forming caves or depressions, which form sinkholes on the land surface. Soils, specifically soil thickness, may play an important role in controlling the rates of limestone dissolution and chemical weathering in karst (Dong et al., 2019). The dissolution of soluble lithologies generates variable hydrologic flowpaths, which

concentrates dissolution processes and creates the heterogeneous geomorphological and hydrologic patterns found in karst environments (Miller, 1990; Worthington, 2009).

Karst topography is characterized by extensive underground drainage systems (i.e., little surface drainage), abundant springs, disappearing streams, cave systems, and sinkholes (**Fig. 1**) (adapted from Kentucky Geologic Survey adapted from Paylor and Currens, 2001).

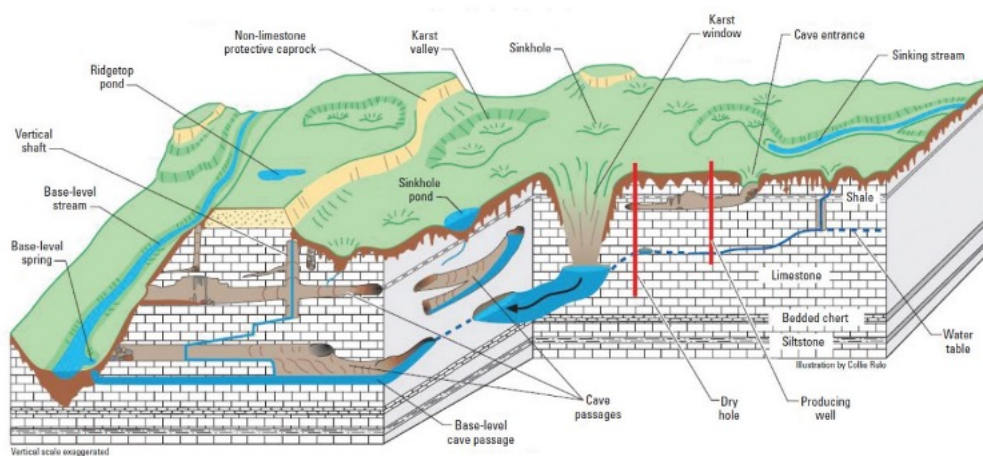


Figure 1. Idealized rendering of karst topography. Karst topography is highly variable and heterogeneous with extensive underground drainage systems. Sinkholes and disappearing streams are common features of karst landscapes and are direct conduits between surface and groundwater. Figure taken from USGS.

There are 6 main types of sinkholes: solution/dissolution, cover-collapse, caprock, dropout, suffusion/subsidence, and buried (Waltham et al., 2005). Karst sinkholes, also called dolines, are notorious for the challenges they present to engineering structures in karst regions; the uncertainty that a soil bridge overlying a karst cave could collapse increases financial risk and the potential loss for human life. In Kentucky alone, 4,000-8,000 cover-collapse sinkholes develop each year (Currens, 2012). These features can damage buildings and roads, causing upwards of \$20 million in damage annually in

Kentucky (Currens, 2012). Techniques that use LiDAR, ground-penetrating radar (GPR), spatial statistics, and machine learning have been used to identify and predict the formation and growth of sinkholes in karst regions (e.g., Cahalan and Milewski, 2018; Hofierka et al., 2018; Panno and Luman, 2018; Sevil et al., 2020; Zhu et al., 2020).



Figure 2. Example of a subsidence sinkhole, note the soil mantle. This sinkhole was one of the study locations of the present thesis and is located in Versailles, KY in the Inner Bluegrass Region.

Subsidence sinkholes are the most common type found in the Inner Bluegrass physiographic region of central Kentucky and these features are the focus of this study (Fig. 2). Subsidence sinkholes generally form via the down-washing of soil and dissolved

solutes into cracks, faults, and fissures in bedrock (Waltham et al., 2005), which concentrates dissolution processes. Subsidence sinkholes also have a soil mantle over the soluble bedrock, which may aid in weathering and influence their hydrologic functioning. The soil mantle overlying the subsidence sinkhole is the focus of this thesis, as this soil cover may vary across these features and this variability is poorly constrained. Subsidence sinkholes differ from dissolution sinkholes (although the terms are often used interchangeably) which have no soil mantle overlying the bedrock (Waltham et al., 2005).

1.2.2 Karst is widespread throughout the world

Karst topography is common throughout the world, with large regions of karst on most continents. Approximately 20% of the earth's ice-free terrestrial surface is underlain by carbonate lithologies (Hartmann and Moosdorf, 2012), and 12% of the world has karst terrain, with notable karst regions in southern China, Mexico's Yucatan Peninsula, and much of the midwestern United States (Sedov et al., 2008). Karst is found extensively throughout the US, with most karst forming from carbonate lithologies and evaporites (**Fig. 3**; Weary and Doctor, 2014), which makes the current work directly applicable to similar carbonate karst regions.

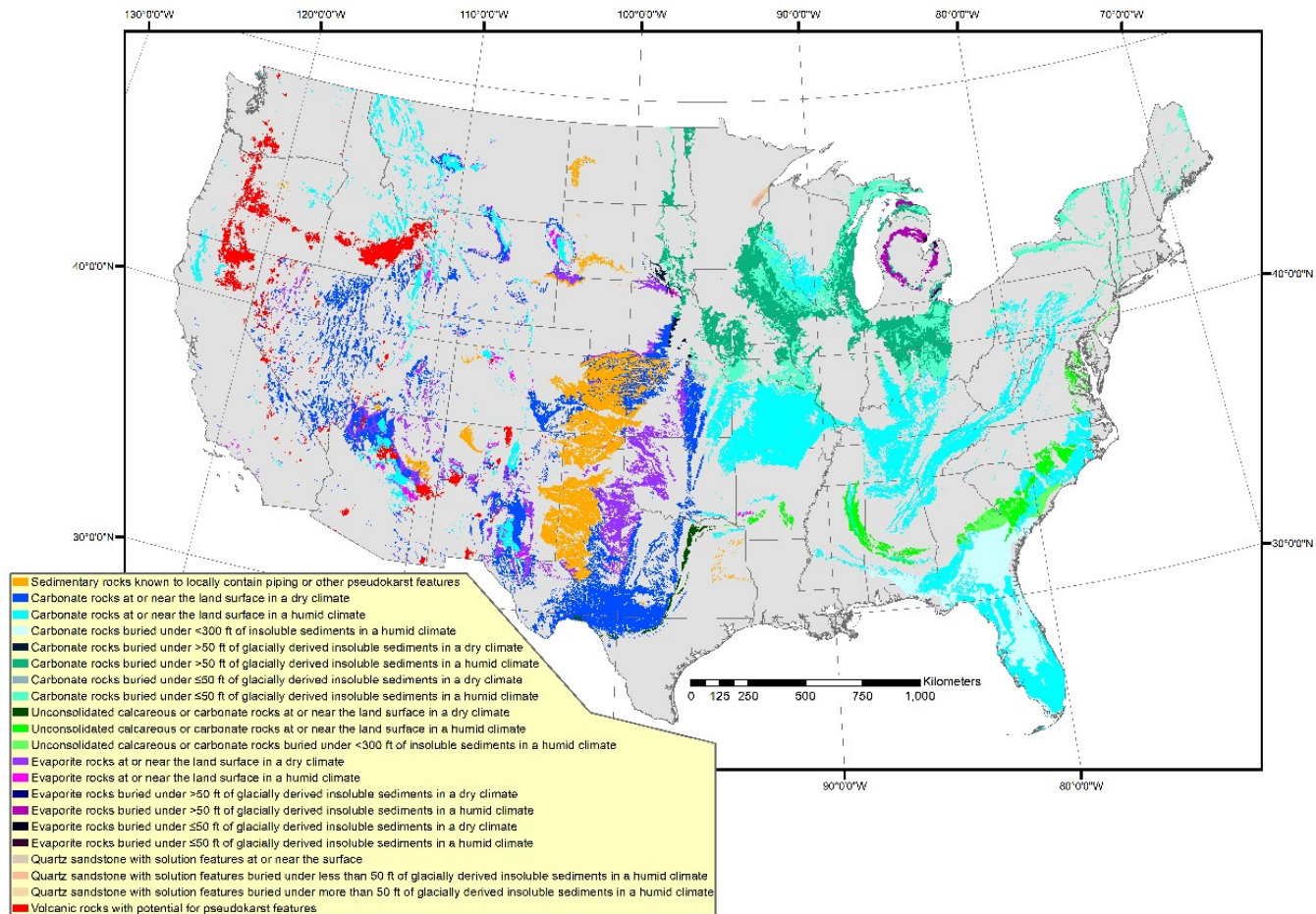


Figure 3. Extent of karst regions in the contiguous United States. Most karst in Kentucky is formed from carbonate rocks at or near the surface. From Weary and Doctor (2014).

Different karst regions have slightly different structural and geologic controls which influence the visual and functional characterization of surface karst features (Scanlon and Thrailkill, 1987). Factors such as the time of platform or geologic unit emergence, climate, rock type (for example, CaCO_3 versus MgCO_3), and macro- and microtopography all impact the appearance of karstic features in the landscape (Bautista et al., 2011). For example, the Upper Tanglewood Member of the Lexington Limestone (lithologic unit of the present study) has interbedded layers including shales, which are less prone to karst feature formation and may disrupt karst expression (Koirala et al., 2016). The different expressions of karst topography due to these factors also likely has an influence on the distribution of soil properties as well, but this influence remains uncertain. Aside from any differences in dissolution rates, all factors controlling karst sinkhole formation were assumed to be the same between the two present study features, thus, the present study will examine the influences of topography on soil properties.

1.2.3 Hydrologic functioning of karst systems and relationship to soil properties

Karst systems provide drinking water for approximately 20-25% of the world's population (Parise et al., 2015). In karst regions, surface and groundwater are usually directly connected, often via conduits and sinking streams (Jeannin et al., 2016). However, unlike non-carbonate terrains, in karst regions surface drainage usually does not mirror belowground systems, complicating watershed delineations (Luo et al., 2016). As such, much of the existing research on karst has focused on the hydrology of these regions. Several studies have investigated the geologic controls on the hydrology of karstic regions around the world (Jeannin et al., 2016; Nerantzaki and Nikolaidis, 2020; Alves et al., 2021). These studies found that the identification of underground flow paths in karst regions is

vital to identifying potential sources of contamination, managing water in karst regions, and predicting the evolution of these systems. These studies also noted the potential anthropogenic impacts on carbonate dissolution, which affects above- and belowground expression of karst features. In addition, there has been a significant focus on the composition of water in karst regions. The concentrations of dissolved substances (including dissolved organic and inorganic carbon) have been the focus of numerous studies which have found that lithology controls the concentrations of many nutrients (e.g., Gonnee et al., 2014; Opsahl et al., 2017; Long et al., 2018; Xu et al., 2020). There has been particular attention paid to the impacts from urban and agricultural areas, and how land use changes and management decisions are impacting karst waters (e.g., Grimmeisen et al., 2016; Bonneau et al., 2017; Galvão et al., 2017; Robinson and Hasenmueller, 2017; Buckerfield et al., 2020; Yue et al., 2020).

Compared to the hydrologic functioning of karst terrains, the role of soils in karst systems are understudied. Given that approximately 12% (Bosák, 2008) of the terrestrial surface has karst terrain and the global importance of karst systems for drinking water there is an increased need to better understand how karst systems respond to disturbance, and the role soils may have in these regions (Sullivan et al., 2019). For example, soil thickness may be an important control on carbonate dissolution, chemical weathering, and karst development (Dong et al., 2019), which may have implications for how karst responds to further disturbance. Bulk soil properties can exert large control over water movement and material transport (i.e., dissolved solids, sediment, contaminants) (Hillel, 2003). Understanding the soils in these systems should be a part of complete comprehension of these delicate environments. Connecting soil hydrologic functioning to groundwater and

phreatic processes is vital for understanding interactions between soils and hydrologic systems in karst regions, but to accomplish this long-term goal we need to quantify changes in soil properties within karst features. The significant global coverage of karst terrains means that soils may potentially exert a large and less understood control on karst evolution.

1.3 Hillslope controls on soil formation and properties

Hans Jenny (1941) identified the main soil forming factors: time, parent material, topography (relief), biota, and climate. Each of these five factors influence soil evolution, and their combined interactions produce observed soil properties. Description and quantification of soils as a function of topography are commonly referred to as a toposequence (Jenny, 1941, 1961). A toposequence was defined by Milne (1935) and Ruhe (1960) as a catena (L. “chain”) where relief is the only non-constant soil forming factor across a series of soils. Each of the five common landscape positions: summit, shoulder, backslope, footslope, and toeslope (**Fig. 4**) have unique local soil forming processes which influence how soil properties change and are expressed at each position (Ruhe and Walker, 1968). Several aspects of topography exert an influence on pedogenesis including slope orientation (referred to here as aspect), slope gradient, curvature, and landscape or slope position.

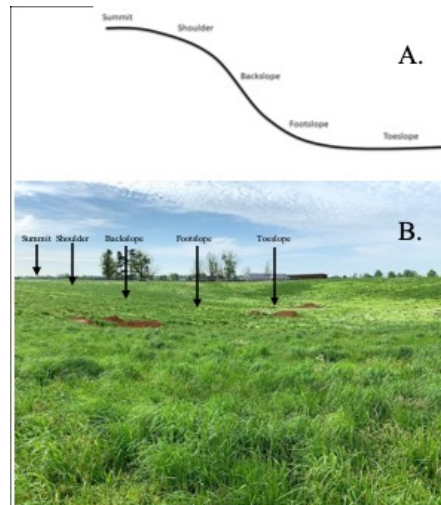


Figure 4. Idealized (A) and actual (B) hillslopes demonstrating the relative positions of the summit, shoulder, backslope, footslopes, and toeslopes.

Pedogenesis along a toposequence is dependent on several factors, including slope position, slope, aspect, and curvature (Huggett, 1975; Yoo et al., 2007). Toposequence studies identified the most common lateral changes in bulk soil properties as a function of topography (e.g., Martini and Mosquera, 1972; Stolt et al., 1993a; b; Egli et al., 2008; Chirinda et al., 2014; Ibrahim and Lal, 2014; Rasmussen et al., 2015; Lan et al., 2021). Aspect exerts a strong influence on microclimate, which alters soil temperature and moisture status and moderates the rate and degree of pedogenesis (Birkeland, 1999). In the midlatitudes, aspect may be one of the stronger influences on pedogenesis compared to climate or vegetation alone (Hunckler and Schaetzl, 1997). One example are the strong differences in the degree of podzolization in northern Michigan between north- and south-facing slopes (Hunckler and Schaetzl, 1997). Locally in Kentucky, differences in aspect leads to greater organic matter content, cooler soil temperatures, and less development (i.e., cambic horizons) on north-facing slopes; south-facing slopes exhibited stronger soil development (i.e., argillic horizons) and higher soil temperatures (Franzmeier et al., 1969).

Commonly, aspect may contribute to differences in soil properties within karst sinkholes, however, the scale of these features may limit the ability to observe strong differences.

Slope gradient and position are also tied to moisture and erosion regime (Huggett, 1975); divergent landscape positions erode and export matter and energy, whereas convergent landscape positions accumulate and import matter and energy (Rasmussen et al., 2015). Divergent landscape positions such as the backslope and shoulder positions are characterized by their linearity and convexity and corresponding material loss. Soils in these positions are generally thinner and likely well-drained, minimizing observed profile development (e.g., Ping et al., 2005; Badía et al., 2013; Lybrand and Rasmussen, 2015). Simple horizonation relative to more stable hillslope positions is likely as is shallower depth to a C horizon or bedrock (Catani et al., 2010; Lebedeva and Brantley, 2013). The movement of water quickly off these positions also slows the rates of chemical weathering that are responsible for much of soil development (Yoo and Mudd, 2008a).

In contrast, the convergent foot- and toeslope positions are depositional environments, accumulating sediments and water. Both gravity and water transport sediment and other materials down slope where they collect in lower slope positions (Hancock et al., 2019). Depositional slope positions generally accumulate finer particles, silts in particular, that have moved downslope (Zádorová et al., 2015; Borden et al., 2020). These soils are also generally deeper and not as well-drained as compared to divergent positions (Birkeland, 1999). As such, drainage issues and redoximorphic features are more likely in the foot- and toeslope (Reuter and Bell, 2003; Ticehurst et al., 2007).

1.3.1 Influence of karst topography on pedogenesis

While many soil toposequences/catenas have been described in karst regions, soil toposequence studies in specific features of karst regions are less common. However, several investigations of pedogenesis in karst features have been performed, predominantly in the tropics of Central America and Southeast China (e.g., Shang and Tiessen, 2003; Sedov et al., 2007, 2008; Cabadas-Báez et al., 2010; Bautista et al., 2011; Frago-so-servón et al., 2020; Maranhão et al., 2020; Lan et al., 2021). For example, a soil toposequence in the karst of central Florida, USA exhibited lower pH values in lower landscape positions, but generally little differences in other properties (Banker et al., 1995). A similar toposequence in the Cerrado region of Brazil indicated strong variation in cation exchange capacity and pH between landscape positions (Silva et al., 2017); however, soils in this toposequence also exhibit significant secondary CaCO₃ formation, which is unlikely in the current study region. The Florida and Cerrado toposequences may indicate that toposequences in the karst features in the Inner Bluegrass may only be demonstrably different in certain key bulk soil properties. Chen (2012) found higher SOC and total N in karst areas in their study from the southwest karst region of China when compared to levels from non-karst soils. While the present study examined only soils developed over carbonate lithologies, and therefore soils likely to be developing on karst terrain, it is expected that this trend would hold when compared to soils outside of the Bluegrass in non-karst regions.

1.3.2 Soil carbon dynamics in karst regions

Soils are the largest terrestrial carbon pool, storing more carbon than the atmosphere and plants combined (Malhi et al., 1999; Stockmann et al., 2013). The soil organic carbon pool specifically is one of the largest in the terrestrial environment (Chaopricha and Marín-Spiotta, 2014) holding an estimated 2344Pg of organic carbon (Stockmann et al., 2013). Topography has recently been recognized as an important control on the movement and stability of SOC across landscapes (Berhe et al., 2007, 2018); where erosion may be a globally important carbon sink. As karst systems are dynamic and sensitive to change and are a significant global pool of inorganic C (Du et al., 2013), there is potential for variable SOC stocks and a greater need for understanding karst SOC dynamics (Gaillardet et al., 2019). Further, since karst naturally forms depressional features (i.e., sinkholes), these landscapes may store significant quantities of soil carbon. Understanding if and how sinkhole SOC dynamics differ from trends seen on traditional hillslopes will be useful in making informed land management decisions and quantifying the contribution of these features to the soil carbon cycle.

Karst and limestone-derived features may also have different soil organic matter stabilization mechanisms. Shang and Tiessan (2003) examined the soil organic carbon stabilization mechanisms of limestone-derived soils of the Yucatan Peninsula. They identified high SOM content in these soils, and noted the potential stabilization was due to secondary carbonates. It has been assumed that soil texture (clay content in particular) is the most important physical property controlling SOC variation between soils (Schillaci et al., 2017). While texture remains an important driver of SOC persistence, other factors such as exchangeable calcium or iron- and aluminum-oxyhydroxides are equally as

important for SOC persistence (Torn et al., 1997; Kaiser and Guggenberger, 2000; Percival et al., 2000; Lawrence et al., 2014; Rasmussen et al., 2018); however, Shang and Tiessen (2003) found that clays and metal oxides were not related to OM stability in the limestone-derived soils of the Yucatan. We can therefore expect to see changes in SOC levels at each hillslope position not only because of textural differences arising from hillslope processes, but because of changes in bulk soil properties that control SOC retention; further, these dynamics may potentially be unique to karst landscapes and soils. Water and sediment movement downslope may also explain the increased carbon measured in downslope positions regardless of the hillslope soil properties (Brevik and Homburg, 2004).

The properties of the soils overlying soluble lithologies (e.g., limestones, dolostones), the dominant soil forming processes occurring in karst sinkholes, and the relationships between sinkhole features and soil-landscape patterns remain poorly constrained in karst regions (Chen et al., 2018). Subsidence sinkhole soils in mesic climates such as that of the Inner Bluegrass have not been studied in terms of their pedogenic development. Further, sinkholes are usually only discussed in terms of potential hazards to human structures or disruption of farming activities, with little consideration of soil properties or classification. Quantifying the physical, chemical, and mineralogical properties of the soils forming in these features have the potential to better inform our understanding of the hydrologic and carbon cycles of karst landscapes. The results of this study are applicable to other karst regions in Kentucky outside of the Inner Bluegrass. Approximately half of the state is underlain by rocks with the potential for karst feature development, and around 25% already has significant karst drainage (Blair et al., 2012), a

better understanding of the bulk soil properties within the features has the potential to contribute to stronger understanding of karst flowpaths within Kentucky.

1.4 Thesis objectives

The present study seeks to alleviate these uncertainties by describing and quantifying the bulk soil properties as a function of elevation in karst sinkholes (see Chapter 2). This thesis addresses this gap by characterizing and describing two karst soil toposequences in the Inner Bluegrass Region of central Kentucky. The objectives of this thesis were:

1. Sample and describe soils in karst sinkhole features as a function of landscape position (i.e., elevation)
2. Quantify the soil physical, chemical, and mineralogical properties of karst soils as a function of landscape position (i.e., elevation)
3. Correlate soil physical, chemical, and mineralogical properties to soil carbon and nitrogen content in karst features

CHAPTER 2. PRESENT STUDY

2.1 Introduction

Karst topography is heterogeneous; the rapid dissolution of carbonates leads to unique landscape features such as disappearing streams, abundant springs, extensive cave systems, lack of surface drainage, and sinkholes. Karst hydrology is highly interconnected with rapid flowpaths that connect the soil surface to deeper groundwater. As karst topography develops, heterogeneous drainage develops which likely impacts the soil forming processes across these landscapes, however, much less is known about the impact of karst landscape features on soil-landscape patterns. We investigated the changes in soil physical, chemical, and mineralogical properties across landscape positions (soil toposequence) in two karst dissolution sinkholes in central Kentucky. Our results indicated that not only are soil properties variable between landscape positions, but also potentially variable between individual karst features.

Toposequences quantify changes in soils as a function of relief or topography, while holding the other soil forming factors (climate, biota, parent material, and time) constant (Jenny, 1941, 1961). Toposequences are commonly established using the catena concept, first formulated by Ruhe (1960) based off the work of Milne (1935). A toposequence requires that soils in the sequence are pedologically linked, usually by water and sediment movement (Borden et al., 2020). Previous toposequence studies have identified the most common changes in bulk soil properties as well as the changes in biogeochemical cycles as a function of slope, aspect, and landscape position (Chirinda et al., 2014; Ibrahim and Lal, 2014; Lan et al., 2021).

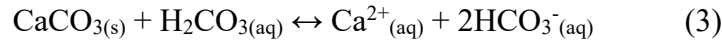
Topography controls the microclimate and additions and losses to soil profiles (Birkeland, 1999), which in turn drives pedogenesis or haplodization (Johnson and Watson-Stegner, 1987). Slope aspect, or the cardinal direction a hillslope faces, modulates the local microclimate, controlling the amount and duration of solar radiation, rate of evapotranspiration, and soil temperature (Pelletier et al., 2018). Locally in Kentucky, differences between slope aspect are responsible for greater soil organic matter and weaker horizonation (e.g. cambic horizons) on north-facing slopes; and, stronger horizonation (e.g. argillic horizons) and greater soil temperatures on south-facing slopes (Franzmeier et al., 1969). Slope gradient controls the additions and losses from the soil profile. In a loess-sandstone toposequence in west-central Kentucky, soil thickness decreased with increasing slope gradient, and the authors found increasing soil thickness and argillic horizon development in the lower backslope and footslope positions (Karathanasis et al., 1991). These local examples largely focused on loess and mixed lithologies, however, similar examples in karst landscapes and limestone lithologies are limited. A single example of a soil toposequence in a karst landscape was performed by Prawito (1996). Prawito investigated three soil toposequences in three sinkholes in central Kentucky, however, this study focused on describing lithologic discontinuities in karst features, and there was less interest in their potential for soil carbon storage.

Karst topography is characterized by a heterogeneous landscape with significant underground drainage (Waltham et al., 2005). Closed depressions are diagnostic features of karst terrain, and subsidence sinkholes are common in the Inner Bluegrass (Currens, 2012). They most often appear as circular depressions in the landscape, varying greatly in size, which depends on local fractures and hydrology (Radulovic, 2013). Their shape

indicates that they have internal drainage, resulting in a wide moisture gradient from rim to the base, with the base generally wetter (Frumkin et al., 2015). Surface topography is always evolving in subsidence sinkholes (Lambrecht and Miller, 2006; Waele, 2017). As they age, they generally deepen and widen which alters local topography. By sampling along a toposequence within sinkholes, differences in profile development and bulk soil characteristics may indicate the relative ages of these features (Lambrecht and Miller, 2006; Frumkin et al., 2015) and how their evolution may alter pedogenic processes. Relative age can be helpful in determining relative rates of bedrock dissolution, differences in surface subsidence between features, as well as common pedogenic pathways for soils forming in these features.

Dissolution is the primary process weathering limestone (and other soluble rocks like dolomite and gypsum) and generating sinkholes and other karst features (Šušteršič et al., 2009). The lack of an overlying resistant lithologic layer increases susceptibility to dissolution, as does increased purity of soluble bedrock (Dreybrodt, 1988; Stumm and Morgan, 1996). In short, dissolution occurs when water and carbon dioxide in the soil react to form carbonic acid (among other acids) which dissolves the calcium carbonate (limestone) through carbonation (Eq. 3). Nitric and sulfuric acid are also known to dissolve limestone (Spence and Telmer, 2005; Lerman and Wu, 2006; Calmels et al., 2007; Perrin et al., 2008), and these acids can both be the result of anthropogenic actions, such as the burning of coal (Xu and Liu, 2007; Li et al., 2008). Plant roots also exude organic acids that increase carbonate dissolution (Li et al., 2016). Following dissolution, the soluble products can then be transported to groundwater and exported from the system (Liu et al., 2004; Waele, 2017). The rate at which products are removed depends on the

connections between the soil and belowground conduits, as well as soil depth (Bonacci, 1987).



Equation 1. Calcium carbonate dissolution reaction resulting in bicarbonate.

Dissolution is continually occurring in karst sinkholes so long as the needed reactants are present: soluble rock (reactants), liquid water, and carbon dioxide (Bautista et al., 2011). As products of the reaction build (mainly cations), the reaction will slow; slower dissolution means slower surface subsidence (Liu et al., 2004; Bautista et al., 2011). However, if reactants are being leached from the systems, as is likely in karst systems, the reaction will proceed, and dissolution rates will increase (Dreybrodt, 1988).

Soil may play an important role in the formation of karst features, as the thickness of soil overlying limestone bedrock can impact the rates of dissolution in these systems, with an intermediate soil cover of approximately 1.5m corresponding to the maximum observed weathering rates (Dong et al., 2019). Production of biogenic carbon dioxide, carbon dioxide produced by microbial respiration, organic material decomposition, and plant roots, also enhances dissolution and is necessary for karst formation (Jakucs, 1977; Jennings, 1985; Ford and Williams, 2007; Phillips, 2016). The soils in the sinkholes will be affected by the continual dissolution and subsequent changes in surface topography, specifically changes in slope.

There is a need to understand soils in karst sinkholes and how topography controls bulk soil physical, chemical, and mineralogical properties. Subsidence sinkhole soils in mesic climates such as that of the Inner Bluegrass have been understudied in terms of their

pedogenic development and potential for increased carbon sequestration. The objectives of the present study were to sample and describe soils in karst sinkhole features as a function of landscape position (i.e., elevation), quantify the bulk soil properties as a function of landscape position (i.e., elevation), and relate the measured properties to carbon and nitrogen content. We hypothesize that:

1. Clay content exhibits a generally negative relationship with elevation but has intermediate concentrations at the summit positions.
2. Concentrations of crystalline Fe and Al oxides (dithionite-extractable) have negative relationships with elevation, with the greatest concentrations in the sinkhole bases (toeslopes) and lowest concentrations in the summit.
3. Total carbon content exhibits a negative relationship with elevation but a positive relationship with clay content, exchangeable Ca, and dithionite-extractable Fe and Al oxides.

2.2 Materials and Methods

2.2.1 Study Location and Field Descriptions

Study sites were located at the University of Kentucky's C. Oran Little Research Farm in Versailles, Woodford County, central Kentucky. Two subsidence sinkholes were chosen for this study. Both sinkholes were fairly circular (**Fig. 5**) and comparable in size based on the geophysical dataset used to determine location; sinkhole 1 had a total area of 1.5 hectares, and sinkhole 2 had a total area of 0.1 hectares (Paylor et al., 2003). The different sizes of the two study sinkholes could indicate different sized openings and cracks to the underlying limestone and karst system below. Sinkhole 1 was located at 38.0772 N,

-84.7400 W with elevation above sea level ranging from 262.1 m to 268.7 m, and sinkhole 2 was located at 38.0964 N, -84.7419 W with the summit at 260.2 m above sea level and the base at 254.4 m (**Fig. 6**).

Woodford County is located in the Inner Bluegrass physiographic region of central Kentucky. The Inner Bluegrass is underlain almost entirely by the Lexington Limestone Formation, a phosphatic limestone (Anstey and Fowler, 1969). The study sites in the Inner

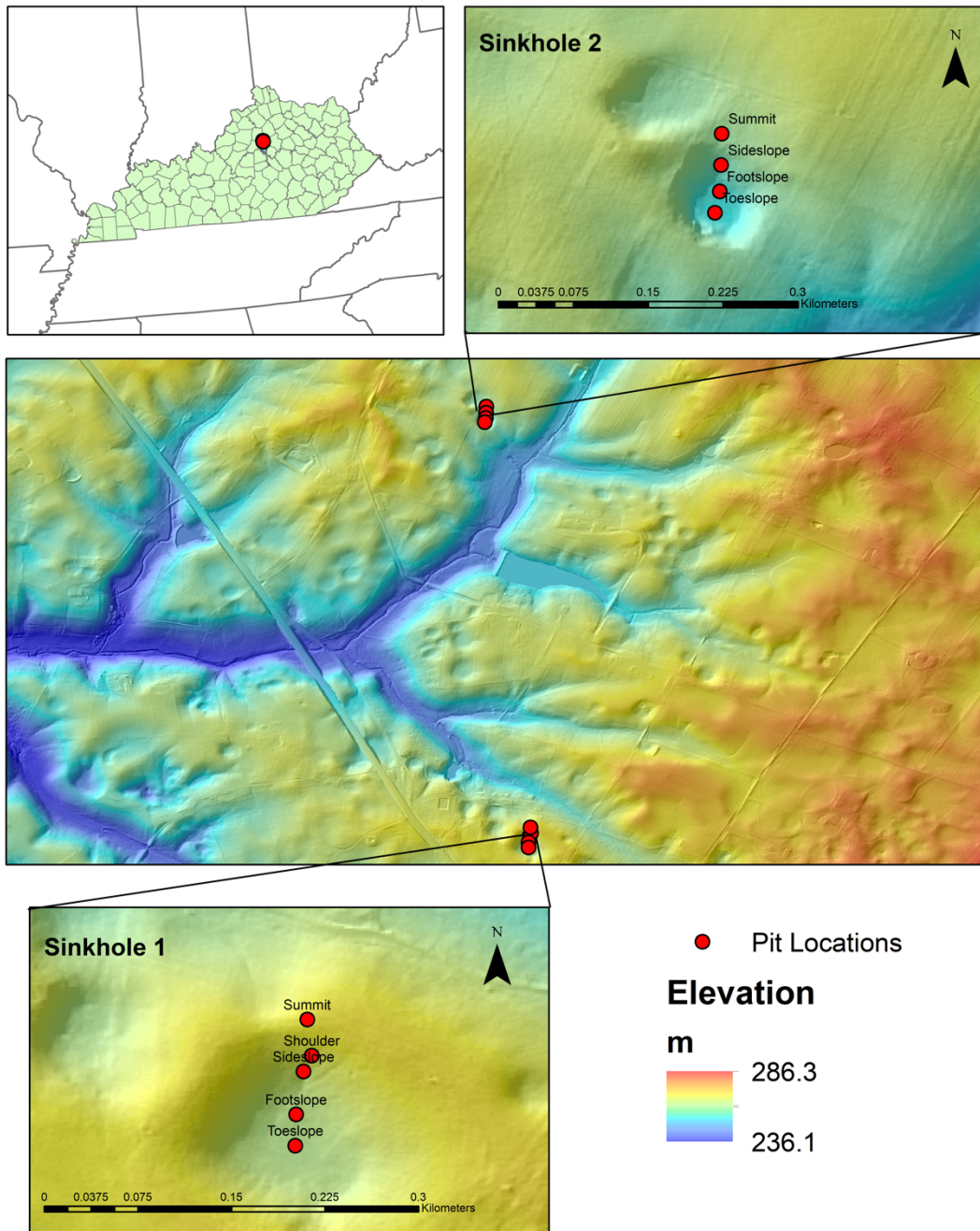


Figure 5. Map of the study area. Digital elevation data from the KY Division of Geospatial Information was used in ArcMap 10.6 (ESRI, Redlands, CA).

Bluegrass are both dominated by naturalized cool season European grasses. Sinkhole 1 is generally ungrazed, and sinkhole 2 seasonally grazed by cattle (approximately once or twice per season). The regional climate is characterized as udic and mesic (Soil Survey Staff, 1999). Woodford County receives an average of 115 cm of mean annual precipitation, with a mean annual temperature of 15°C (Kentucky Climate Center).

Hillslope positions on the south-facing slope of both sinkholes were identified and soil pits were excavated with a backhoe. Profile descriptions were completed in-field between May and June of 2019 (including horizonation, Munsell color, structure, and hand texture). Samples were collected according to genetic soil horizon following standard procedures (Schoeneberger et al., 2012). Coordinates for each excavated pit were collected using a handheld Garmin GPSMAP 64s unit in the WGS84 projection.

2.2.2 Bulk Soil Characterization

Bulk density samples were collected in the field using a slide hammer corer. Collected samples were transported to the lab in ziplock bags to prevent moisture loss. Gravimetric water content was calculated using the difference between air-dry soil weight and oven-dry soil weight after oven drying overnight at 105°C (Soil Survey Staff, 2014).

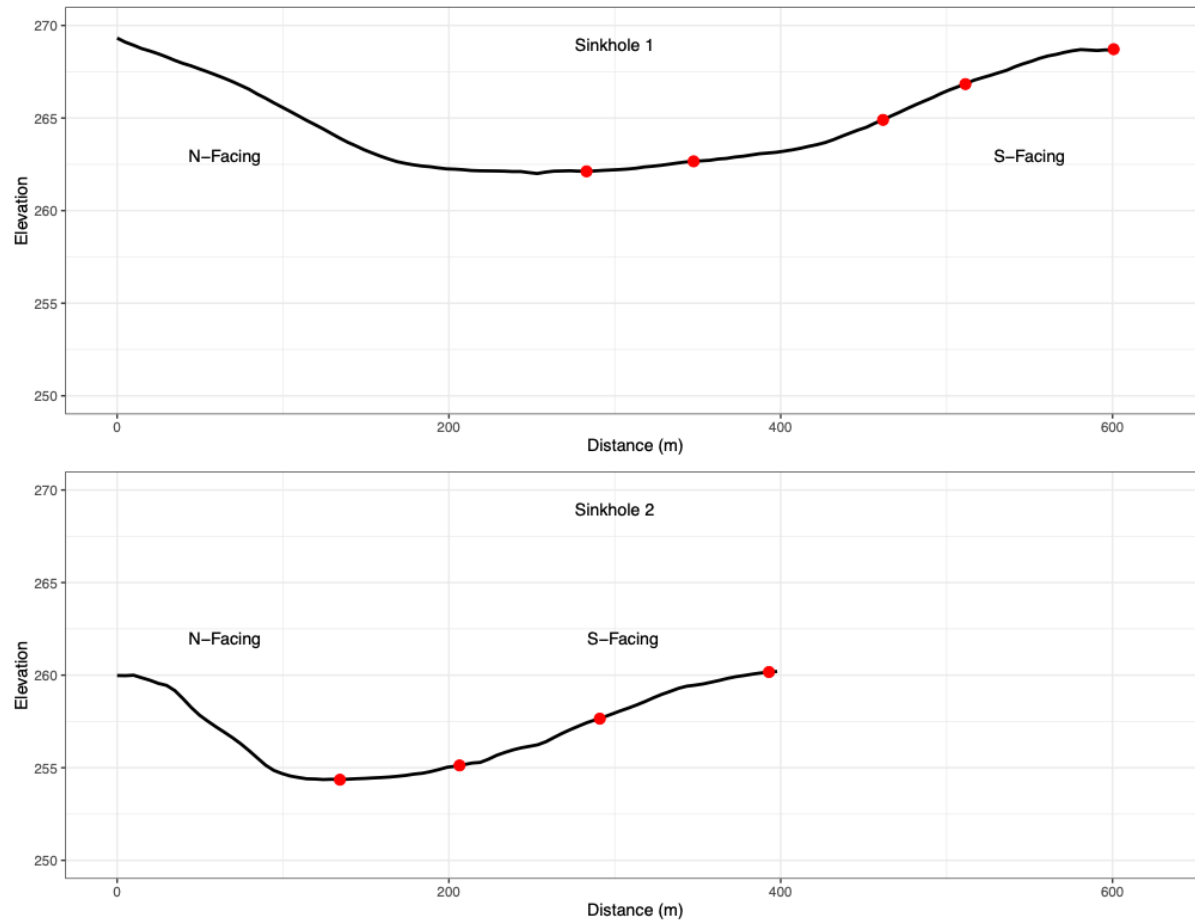


Figure 6. Catena profiles with elevation (m) and marked sampling locations for both study sinkholes.

All samples were air-dried and sieved to 2 mm to separate the coarse from the fine earth fraction; all subsequent analyses were performed on the fine earth fraction. Soil pH and electrical conductivity were measured utilizing a Denver Instruments Model 250 pH-EC-ISI meter using a 1:2 ratio (soil:solution) (Soil Survey Staff, 2014). A 0.02 M CaCl₂ solution (10 mL) was added to the suspension and pH measured (1:4 soil:solution), and pH was also measured in 1:2 ratio of 1 M KCl (Soil Survey Staff, 2014). The average hue, value, and chroma were recorded from four air-dry and moist measurements per sample according to the Munsell color system using a Konica Minolta CR400 chromameter. Total volatile content of samples was determined using loss on ignition (LOI) at 550°C (Soil Survey Staff, 2014). Particle size analysis was performed using the pipette method as described in the Kellogg Soil Survey Laboratory Methods Manual (p. 48-89). To remove excess salts and any potential carbonates, 20 to 30 grams of soil was pretreated with 200 mL of 1M sodium acetate, placed in a hot water bath (80-85°C) for 45 minutes, centrifuged at 3600RPM for 15 minutes, and the supernatant discarded. Following carbonate removal samples were pretreated to remove organic matter; soils were treated with 100 mL sodium hypochlorite (bleach; pH adjusted to 9.5 using 3M HCl), placed in a hot water bath (80-85° C), centrifuged and the supernatant was discarded. This process was repeated 3 times, or until the sample no longer bubbled in the hot water bath. A final rinse with DDI water was performed as the last step.

Ten grams of pre-treated soil was dispersed using 10 mL of a solution of sodium hexametaphosphate and sodium carbonate (dispersant) and 175 mL DDI water. Samples and solution were shaken overnight (16 hours) on low. The next morning, sands were wet-sieved out, and the suspended clays and silts were added to 1L water columns (brought to

volume with DDI water), stirred, and allowed to settle. The total clay and sand masses were subtracted from the weight of pre-treated soil added to the column to determine the mass of silts. Sands were subdivided into very coarse (2.0-1.0 mm), coarse (1.0-0.5 mm), medium (0.5-0.25 mm), fine (0.25-0.1 mm), and very fine (0.1-0.05 mm) fractions.

Samples were treated overnight with 1N ammonium acetate (pH 7.0) to quantify the concentration of base cations (Na, K, Mg, and Ca) and to determine cation exchange capacity. Samples were then filtered through #42 Whatman paper on a Buchner funnel assembly using additional ammonium acetate until reaching a total solution volume of 100 mL. Base cation concentration was determined using a 1:10 dilution with 1% nitric acid and measured using an Agilent Tech 5110 inductively coupled plasma optical emission spectrometer (ICP-OES). Prior to analysis for ammonium, samples were rinsed with 150 mL of methanol to remove remaining excess NH_4OAc . A 10% sodium chloride replacing solution (250 mL; pH 3.0) was filtered through each sample and the leachate was collected for analysis. Ammonium concentration was measured on diluted samples (1:25) and used as a proxy for cation exchange capacity (CEC) (Chaney and Marbach, 1962; Weatherburn, 1967; Ngo et al., 1982). Base cations and CEC were reported in $\text{cmol}_{(+)} \text{kg}^{-1}$, and used to calculate base saturation (%).

2.2.3 Soil Mineralogy and Metal Concentrations

Concentrations of secondary metal (oxy)hydroxides were determined using the citrate-dithionite, ammonium oxalate, and sodium pyrophosphate extractions. Citrate-dithionite extracts Fe, Al, and Mn from organo-metal complexes, amorphous, or poorly crystalline metal oxides, and crystalline secondary oxides (McKeague et al., 1971; Wada, 1989). Two grams of $\text{Na}_2\text{S}_2\text{O}_4 \cdot 2\text{H}_2\text{O}$ (sodium hydrosulfite/sodium dithionite) and 100mL of 0.3M

sodium citrate was added to 4 grams of soil. This mixture was shaken overnight (16 hours), then centrifuged (at 2390 RPM for 10 minutes) and the supernatant was collected. Samples were diluted and digested with 1% nitric acid before analysis on an Agilent Tech 5110 ICP-OES. Metal concentrations were calculated on an oven-dry basis.

Ammonium oxalate targets iron and aluminum organo-metal complexes, and amorphous and poorly crystalline metal oxides, and not from crystalline phases (Schwertmann, 1958; McKeague and Day, 1966; McKeague et al., 1971; Fey and le Roux, 1976; Hodges and Zelazny, 1980; Rasmussen et al., 2005). One hundred milliliters of acid oxalate solution (pH of 3.0) was added to 1 gram of soil in a foil-covered 250mL bottle. They were shaken for 4 hours in the dark, centrifuged at 2390 RPM for 10 minutes, and the supernatant was collected. Supernatant was diluted before digestion with 1% nitric acid and analysis on ICP-OES. Metal concentrations were calculated on an oven-dry basis.

Sodium-pyrophosphate extracts organically associated iron and aluminum (McKeague and Day, 1966; Swift, 1996; Shang and Zelazny, 2008). One gram of soil and 100mL of 0.1M sodium pyrophosphate ($\text{Na}_4\text{P}_2\text{O}_7$) were added to a bottle and shaken overnight (16 hours). The sample was then centrifuged at 3380 RPM for 30 minutes and the supernatant collected. Samples were diluted and digested with 1% nitric acid and analyzed using the ICP-OES to determine concentrations of Fe, Al, and Mn. Metal concentrations were calculated on an oven-dry basis.

Three horizons were selected for XRD analysis from the summit and toeslope of each sinkhole. In general, the top Ap, an upper Bt, and a lower BC horizon were chosen. These three horizons were selected to give a representative sample of the profile mineralogy. Briefly, sample preparation for oriented clay slides; three to five grams of air-dry soil were

added to centrifuge bottles with 200 mL sodium carbonate (pH 9.5-10), then centrifuged at 1000 RPM for 5 minutes. If the supernatant was clear, it was removed, and the first steps were repeated. Once the supernatant was cloudy, sands were wet-sieved out. The remaining silts and clays were separated by repeated centrifuging (750 RPM for 3 minutes) with sodium carbonate (Jackson, 2005). Once the supernatant was clear, a final rinse with DDI water was done (750 RPM, 3 minutes) before silt-sized particles were collected to dry. The clay fraction was collected into dialysis tubing (Spectra/Por molecularporous membrane tubing, 64mm diameter), clipped, and submerged in DDI water. Once water in buckets tested negative for sodium carbonate (tested with silver nitrate; Soukup et al., 2008), suspended clay was transferred into 50 mL centrifuge tubes, lyophilized, and weighed.

Two-hundred micrograms of the prepared clays were added to 50 mL centrifuge bottles, and either 25 mL of magnesium chloride (1M) or potassium chloride (0.5M) was added. Samples were centrifuged at 2000 RPM for 5 minutes, and the process was repeated twice more. A final rinse with DDI water at the same velocity was performed. After pouring off most of the rinse supernatant, samples were vortexed to resuspend the clays before being filtered using a Millipore system to prepare clay slides. The nature of study samples meant only 0.1 grams of clay were needed to produce one slide. Prepared Mg- and K-saturated slides were kept in desiccators with magnesium chloride to maintain a humidity of approximately 50%.

All clay slides were analyzed using a Malvern PANalytic X'Pert Pro. After Mg-saturated samples were run on the XRD at room temperature (25 °C), they were sprayed with a 30% glycerol solution and left to sit overnight before analysis. K-saturated slides underwent three additional heat treatments after being run at room temperature (25°C):

100°C, 300°C, and 550°C. Slides were heated for one hour at each temperature and cooled in a desiccator before being run on the XRD. HighScore software (Malvern Panalytical) was used to identify peaks and extract data for visualization.

2.2.4 Carbon and Nitrogen Determination

Total carbon and nitrogen were determined by the University of Kentucky's Division of Regulatory Services. Briefly, following the methods of Bremner and Edwards (1965) and Yeomans and Bremner (1991), a small soil sample (0.15-0.25 g of homogenized sample) is added to a LECO Elemental Analyzer and combusted at 950°C in an environment of pure oxygen. The resulting gases are analyzed for CO₂ and N₂; the volumes of these gases are converted to total C and N values. Samples were tested for the presence of inorganic carbonates using 1M HCl; no reaction was observed.

2.2.5 Geospatial data and statistical analyses

The geographic coordinates of each excavated pit were used to extract elevation (m), slope (°), aspect (°), and curvature (m⁻¹) for each pit location. Elevation was determined using the KYAPED 5-foot Digital Elevation Model (Kentucky Division of Geospatial Data) and reported as relative to the elevation of the sinkhole base. Slope, aspect and curvature were calculated using ArcMap 10.6 (ESRI, 2018). Curvature represents the rate of change of the slope (m⁻¹), positive values of curvature indicate convex surfaces and negative values of curvature indicate concave surfaces.

Soil property values were aggregated across all horizons within each profile. Where noted, soil property values were calculated on a mass per area basis and summed across the profile according to:

$$total_x(kg\ m^{-2}) = \sum_{i=1}^k x_i \cdot \left(\frac{z_i}{100}\right) \cdot \rho_i \quad (4)$$

Where, k is an individual soil horizon or layer, x_i is a soil property on a mass per mass basis ($kg\ kg^{-1}$ or $cmol_+ kg^{-1}$) per horizon, z_i is the horizon thickness (m), and ρ_i is the horizon oven dry bulk density ($kg\ m^{-3}$). For values that were percentage based and unitless, a horizon thickness or depth weighted average was calculated according to:

$$\sum_{i=1}^i x_i \cdot \left(\frac{z_i}{\sum z}\right) \quad (5)$$

Where, x_i is a soil property on a percent or unitless basis, z_i is the horizon thickness (m), and $\sum z$ is the total horizon thickness.

All statistical analyses were performed in R (R Core Team, 2013) . Due to the small number of pedons described and sampled, non-parametric Spearman's rho values were calculated for the association between various measured variables. A partial least squares regression was used to test the relationships between total carbon (TC), total nitrogen (TN), and carbon:nitrogen (C:N) ratios and other soil physical, chemical, and mineralogical properties, and to determine the primary drivers of TC, TN, and C:N. Partial least squares regression was calculated in R using the "pls" package (Mevik et al., 2020) using leave-one-out-cross-validation. The number of components retained in the model was based on minimizing the root mean square error of the prediction and maximizing the cross-validated R^2 .

2.3 Results

2.3.1 Field Descriptions and Morphology

Select morphological data have been compiled for the summits and toeslopes of both sinkholes in Table 1. Based on field descriptions and photos of profile faces (**Figs. 7-10**), consistent differences were observed between the two study sinkholes, including redder colors, stronger structure, stronger horizonation, and greater clay content in sinkhole 1. Wet and dry color was recorded for each sample as was redness rating. Higher moist redness ratings (2.88 ± 0.61 ; $\mu \pm 1\sigma$) and moist chromas (3.8 ± 0.29) were observed in sinkhole 1 compared to sinkhole 2 (RR: 1.9 ± 0.21 ; chroma: 3.24 ± 0.16); this implies older, more weathered soils in sinkhole 1, which was also the larger feature.

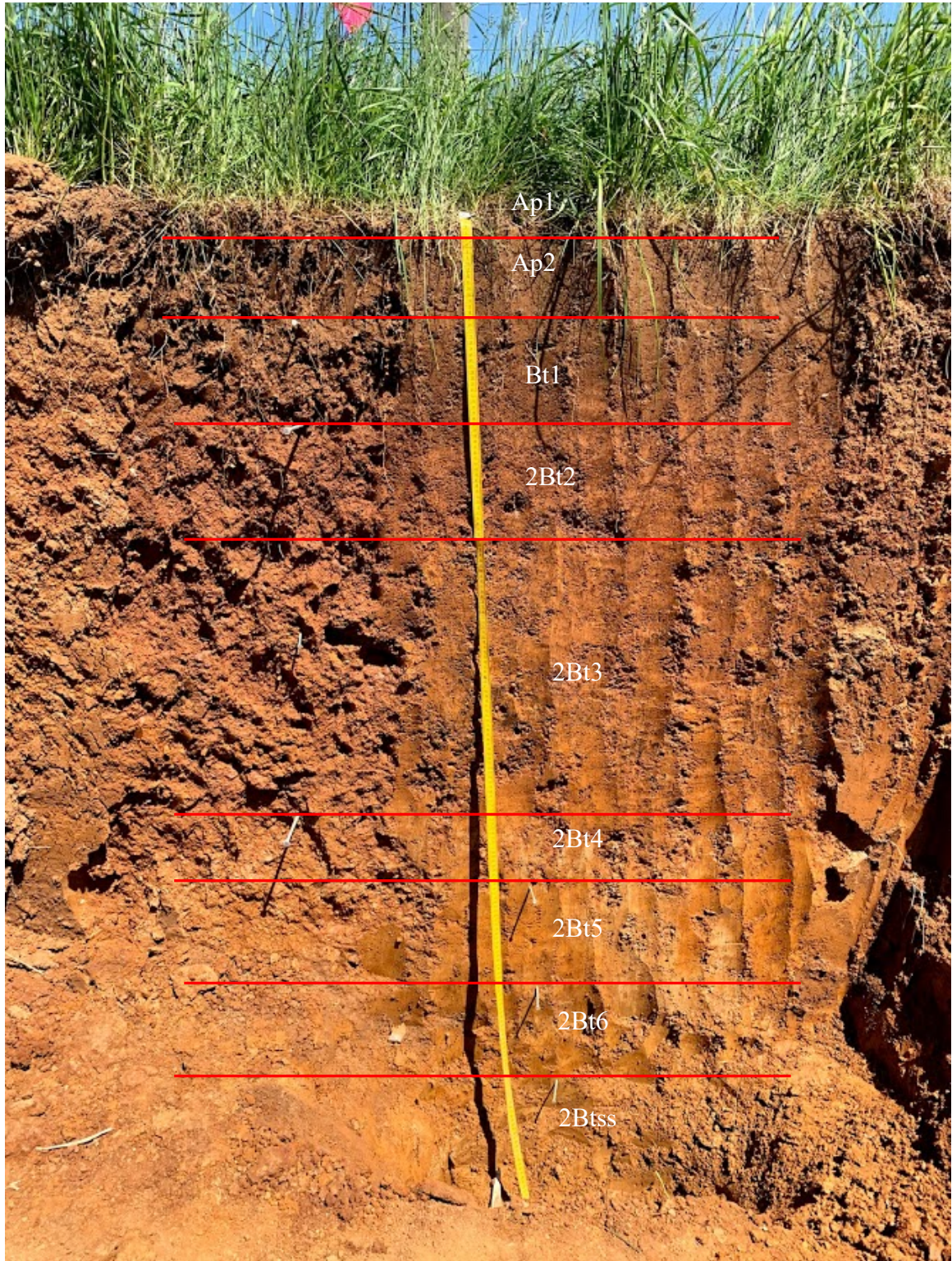


Figure 7. Sinkhole 1 summit profile with labeled horizons at approximate depths described in the field.

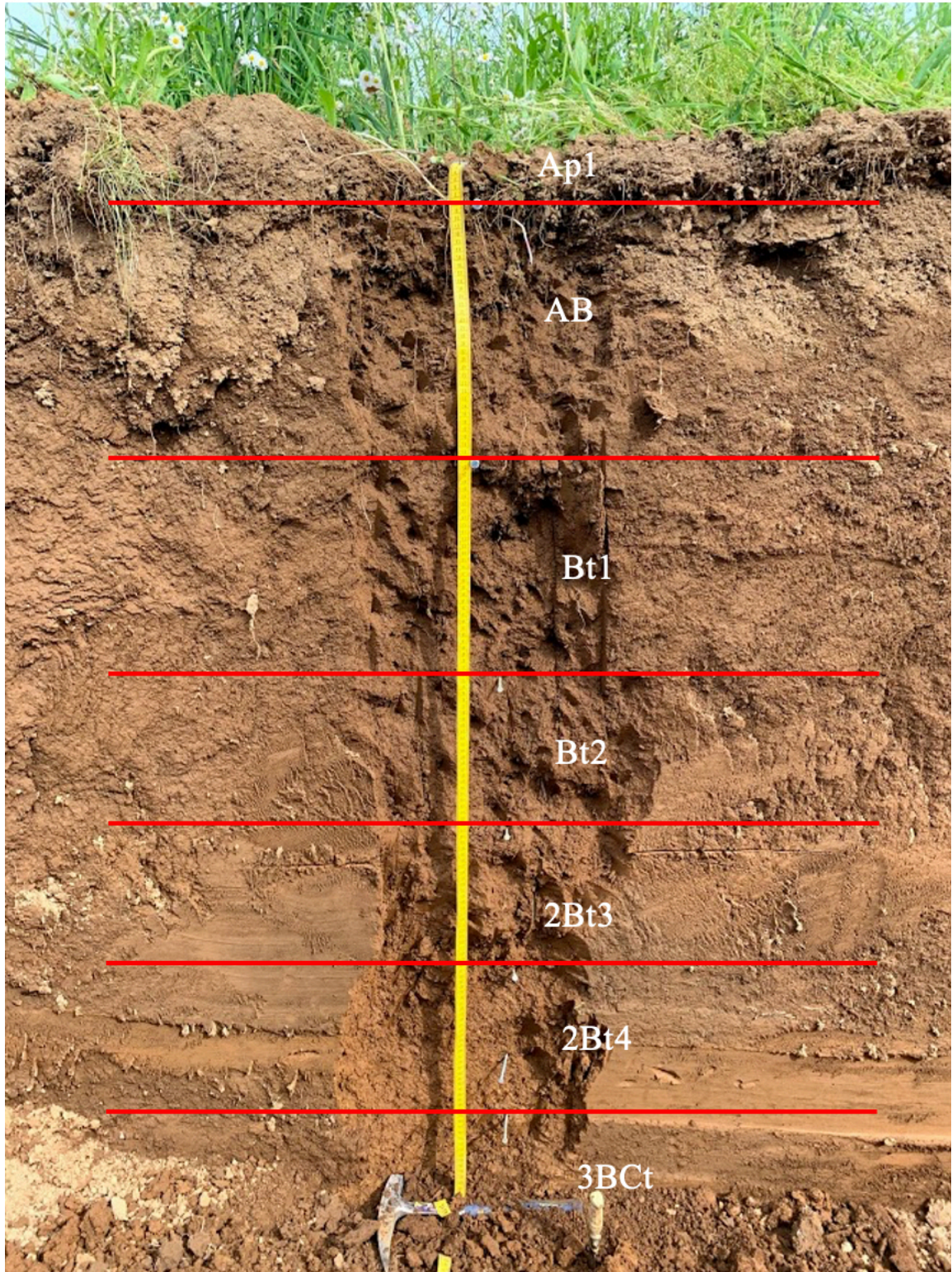


Figure 8. Sinkhole 1 toeslope profile with labeled horizons at approximate depths described in the field.

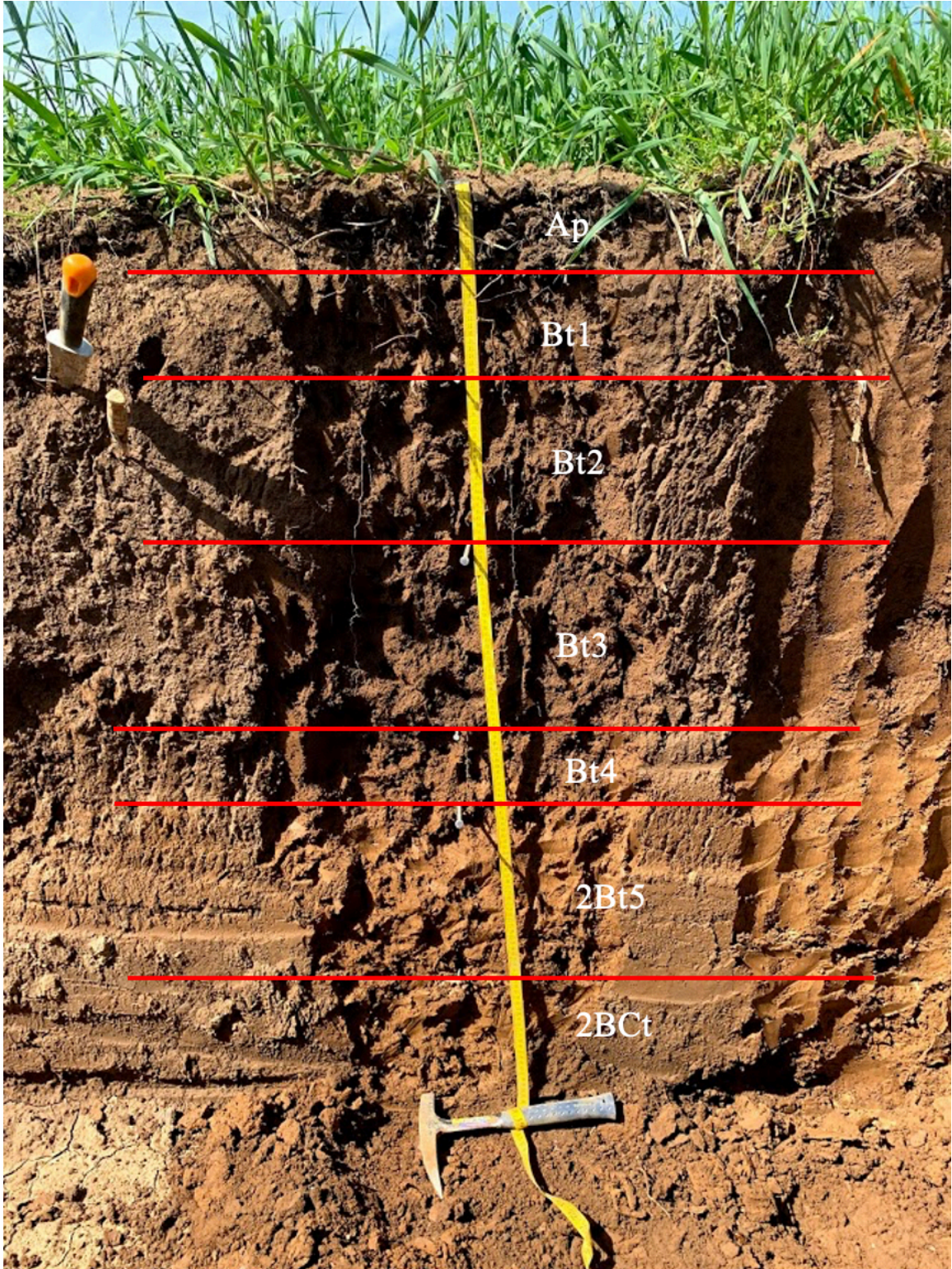


Figure 9. Sinkhole 2 summit profile with labeled horizons at approximate depths described in the field.

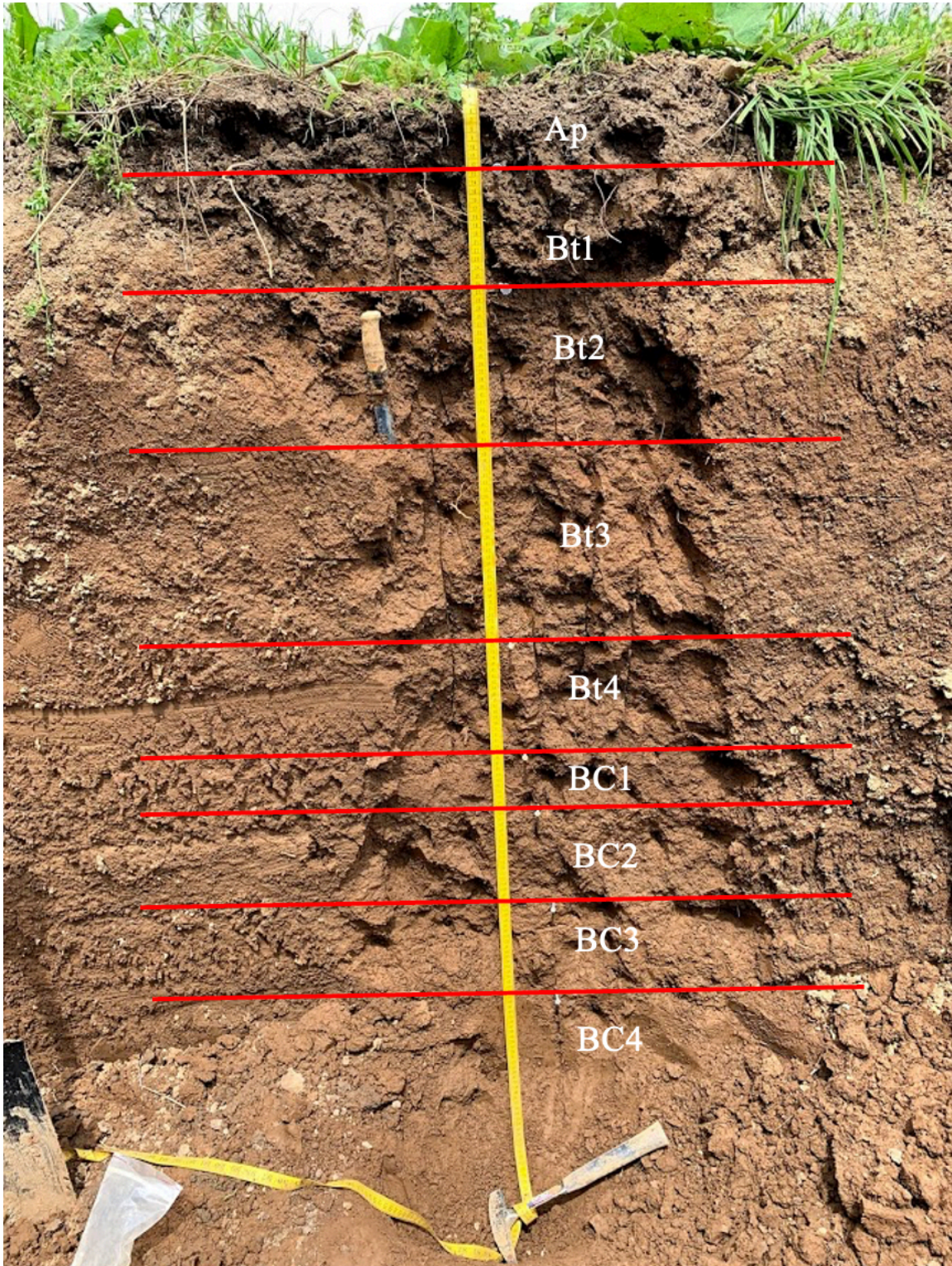


Figure 10. Sinkhole 2 toeslope profile with labeled horizons at approximate depths described in the field.

2.3.2 Soil Properties as Function of Topography

Similar to other toposequences in temperate regions, we found that elevation, slope, and curvature exerted strong controls on bulk soil physical and chemical properties. The relationship between elevation and dithionite-extractable Al (Al_d ; **Fig. 11**) was not significant (Spearman's ρ : 0.45) but exhibited a positive trend. A strong positive relationship (Spearman's ρ : 0.81) was observed between dithionite-extractable Fe (Fe_d) and relative elevation (**Fig. 12**). Similarly, dithionite-extractable Si (Si_d , $kg\ m^{-2}$) had a positive relationship with relative elevation (m) (**Fig. 13**). This was a relatively strong relationship (Spearman's ρ : 0.83) compared to other extractable metals, but did not support our hypothesis that there would be a negative or inverse relationship between these properties and elevation. The influence of relative elevation on Al_d , Fe_d , and Si_d was the opposite as expected and did not confirm our second hypothesis, but the strength of trends suggested that karst features likely influence the distribution of Al, Fe, and Si across the elevation gradient.

In general, sinkhole 2 had greater concentrations of total C for each hillslope location sampled. The relationship between total C and relative elevation was negative, which supported our third hypothesis; more C was observed in the base of study sinkholes than at higher relative sampling locations (Spearman's ρ : -0.50; **Fig. 14**). Similar results were observed between total N (**Fig. 15**; Spearman's ρ : -0.53) and C:N ratio (**Fig. 16**; Spearman's ρ : -0.5). Percent clay (**Fig. 17**; Spearman's ρ : 0.51) also exhibited a relatively strong positive trend with relative elevation; we observed higher clay values in the higher landscape positions such as the summit than in the sinkhole bases. Total C and clay

exhibited inverse trends with relative elevation, implying a weak relationship between these two variables.

Both dithionite-extractable Fe and Si had positive relationships with curvature (**Fig. 18** and **19**, respectively). Again, we had hypothesized that the opposite trends would be observed. The relationships between Fe_d and Si_d and the topographic variables of relative elevation and curvature highlight the importance of topography in controlling the concentrations of certain elements in sinkhole soils.

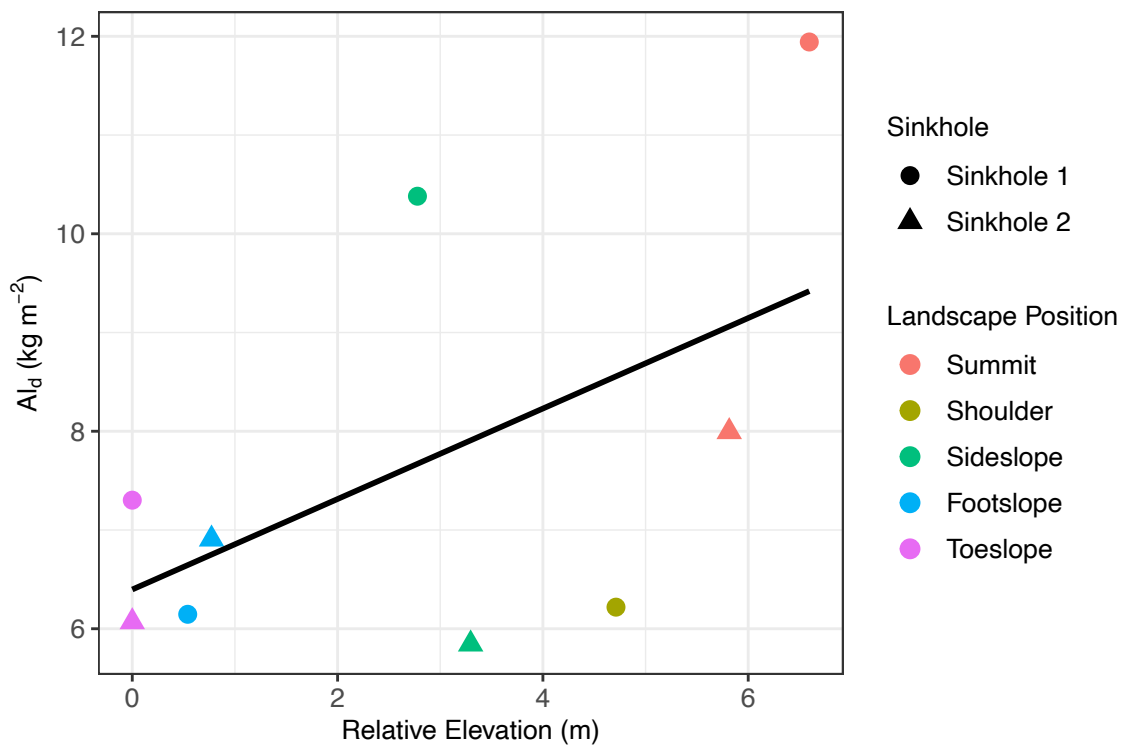


Figure 11. Dithionite-extractable Al ($kg\ m^{-2}$) exhibited a positive relationship with relative elevation, not supporting our second hypothesis. (Spearman's ρ : 0.45, p-value: 0.22, df: 7).

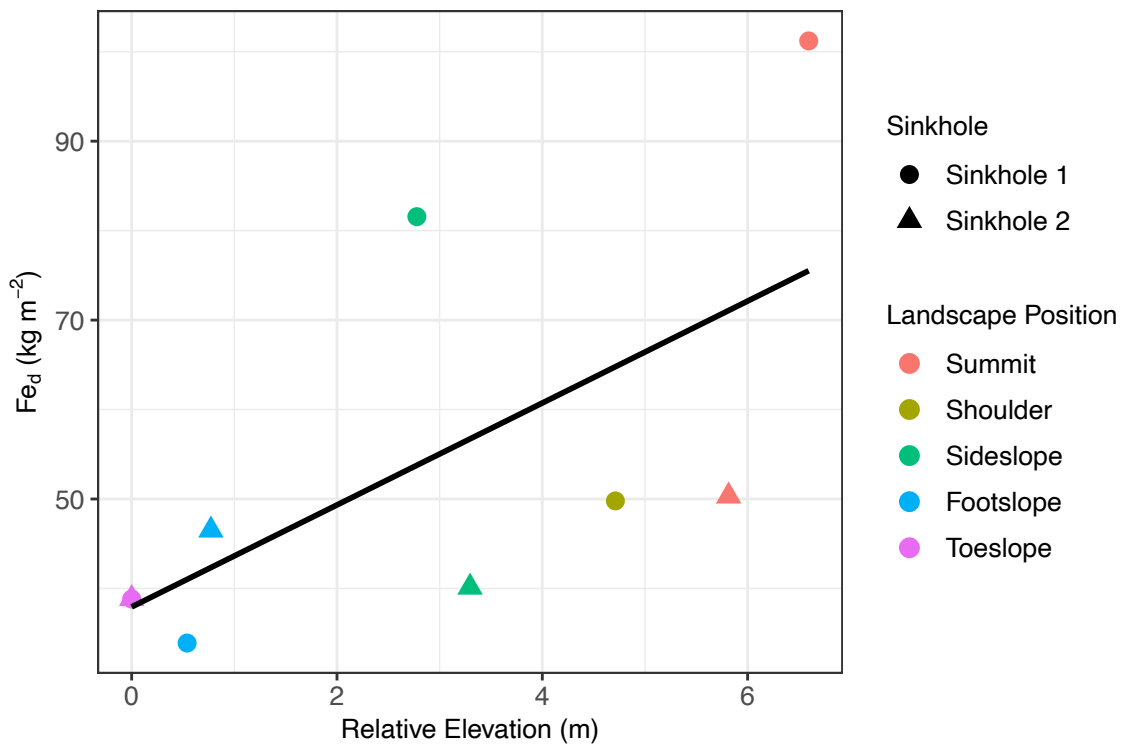


Figure 12. Dithionite-extractable Fe (kg m^{-2}) exhibited a positive relationship with relative elevation, which does not support our second hypothesis. (Spearman's ρ : 0.81, p-value: 0.0079, df: 7).

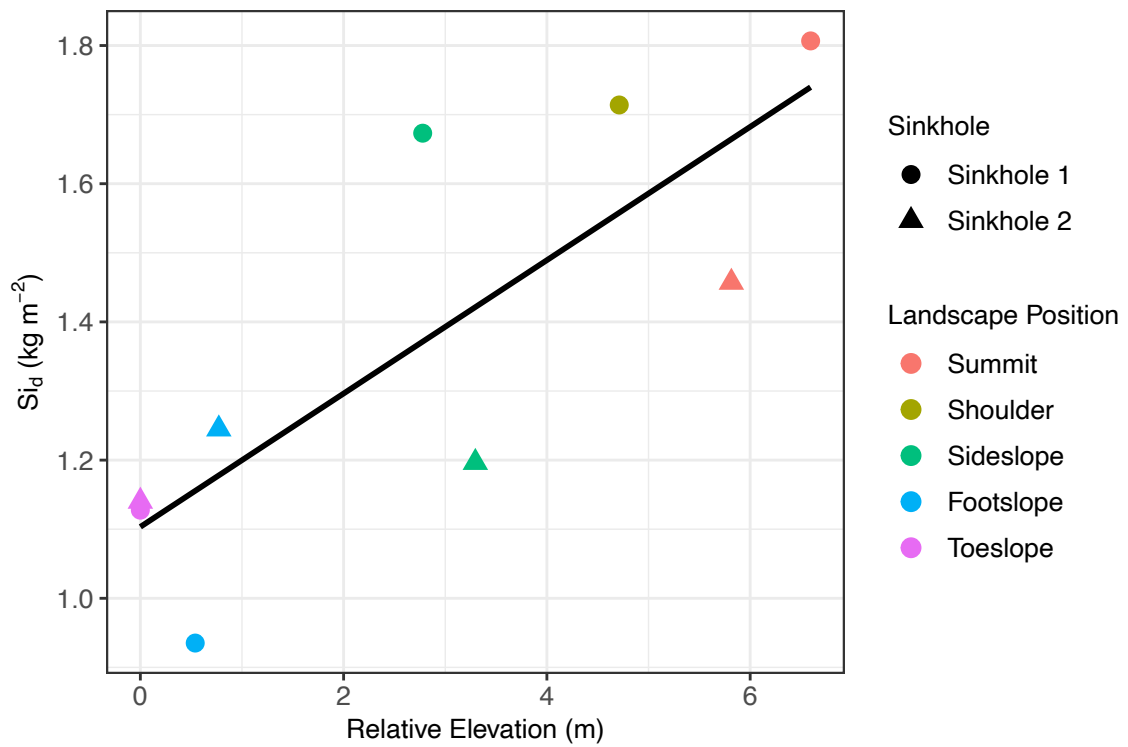


Figure 13. Dithionite-extractable Si (kg m^{-2}) exhibited a positive relationship with relative elevation (m), which did not support our second hypothesis. (Spearman's ρ : 0.83, p-value: 0.0058, df: 7).

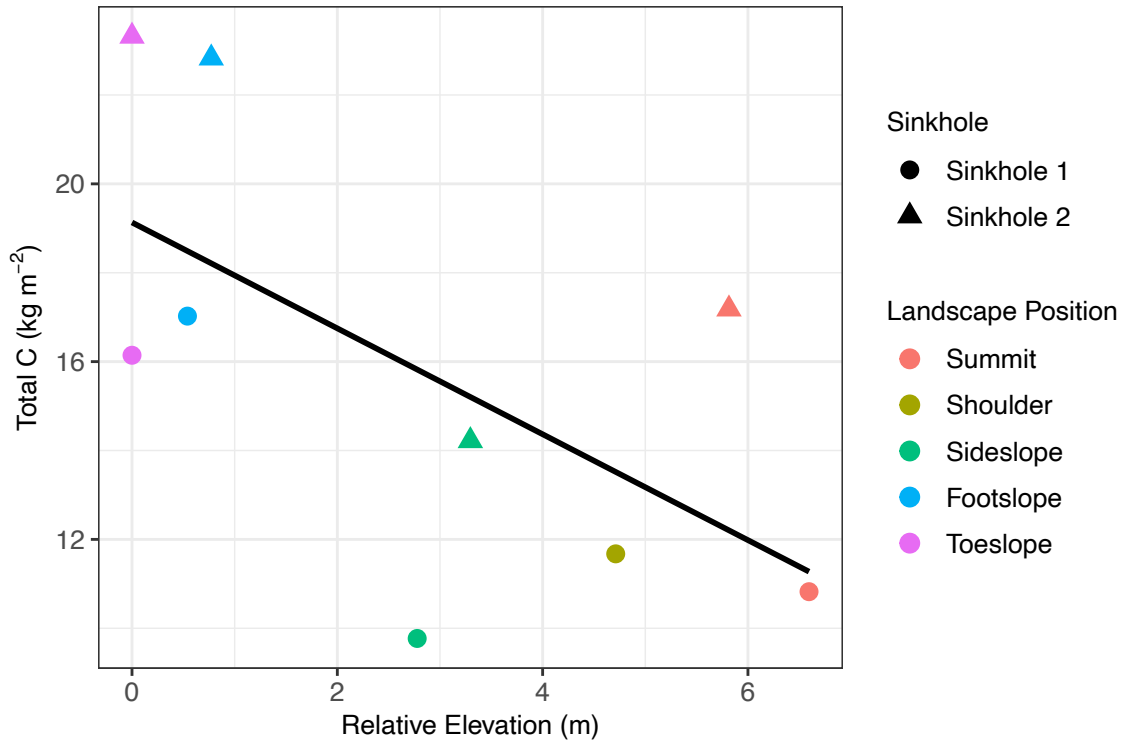


Figure 14. Total C (kg m⁻²) exhibited a negative relationship with relative elevation (m). (Spearman's ρ : -0.50, p-value: 0.17, df: 7).

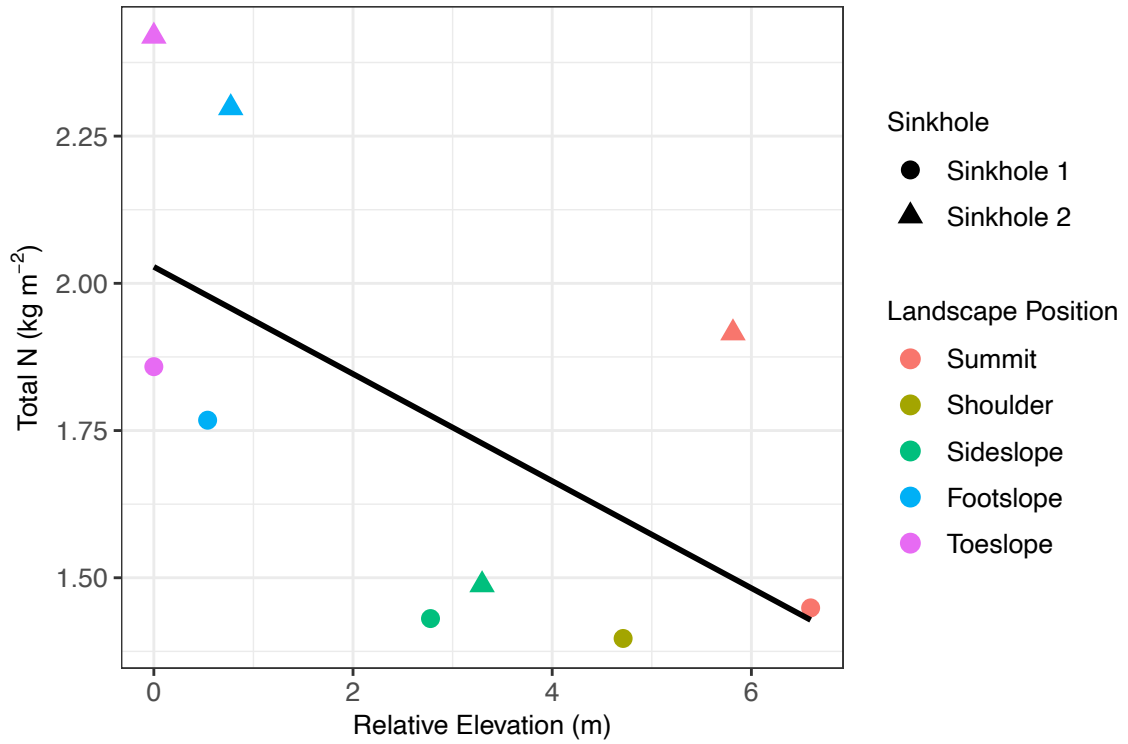


Figure 15. Total N (kg m⁻²) exhibited a negative relationship with relative elevation (m). (Spearman's ρ : -0.523, p-value: 0.14, df: 7).

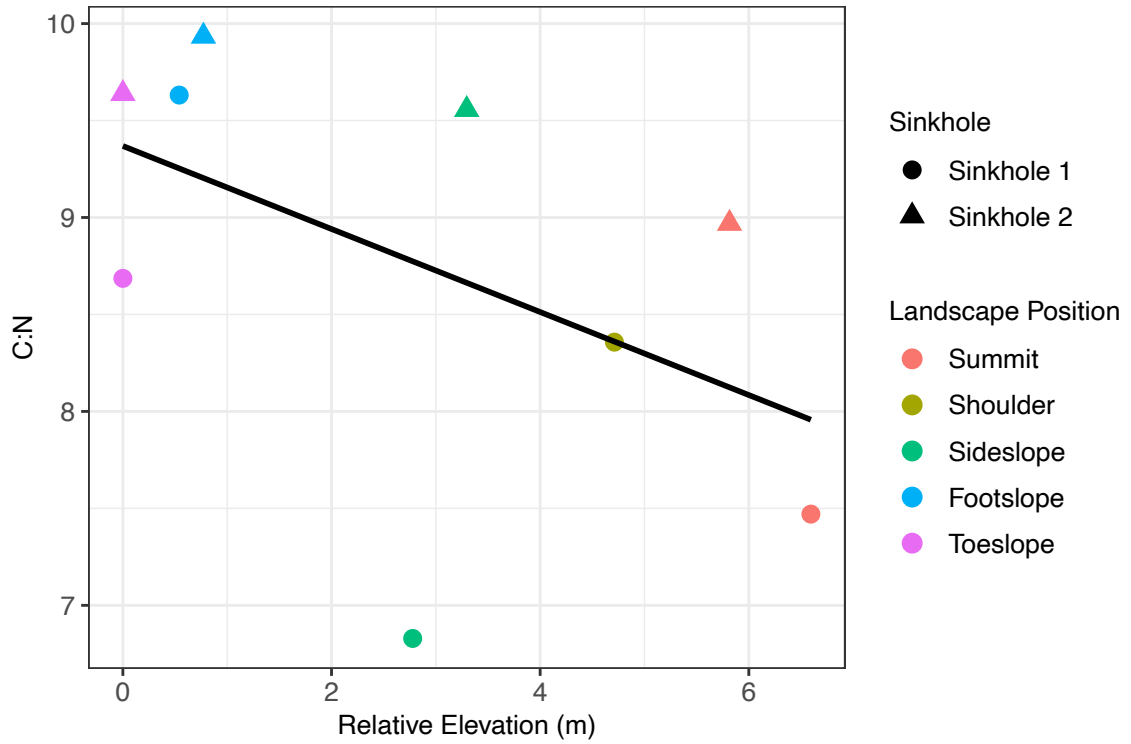


Figure 16. C:N exhibited a negative relationship with relative elevation (m). (Spearman's ρ : -0.5, p-value: 0.17, df: 7).

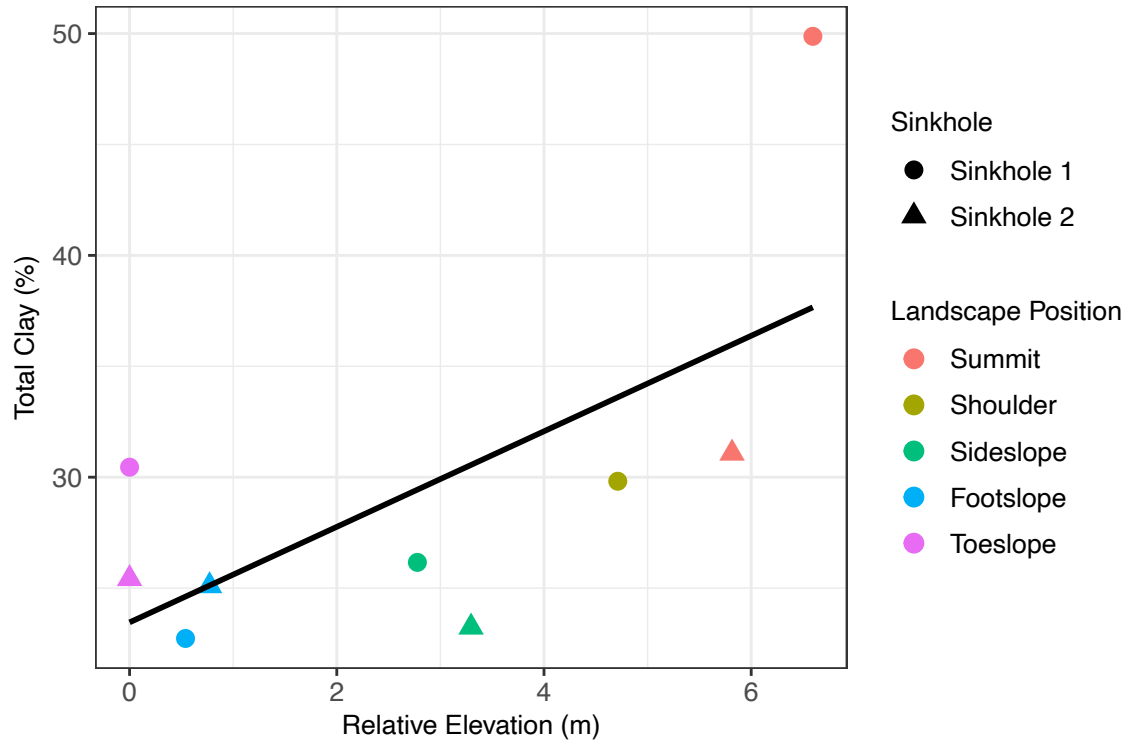


Figure 17. Total clay (%) showed a positive relationship with relative elevation (m), meaning we saw more clay, in general, at the higher hillslope positions than in the base. (Spearman's ρ : 0.51, p-value: 0.16, df: 7).

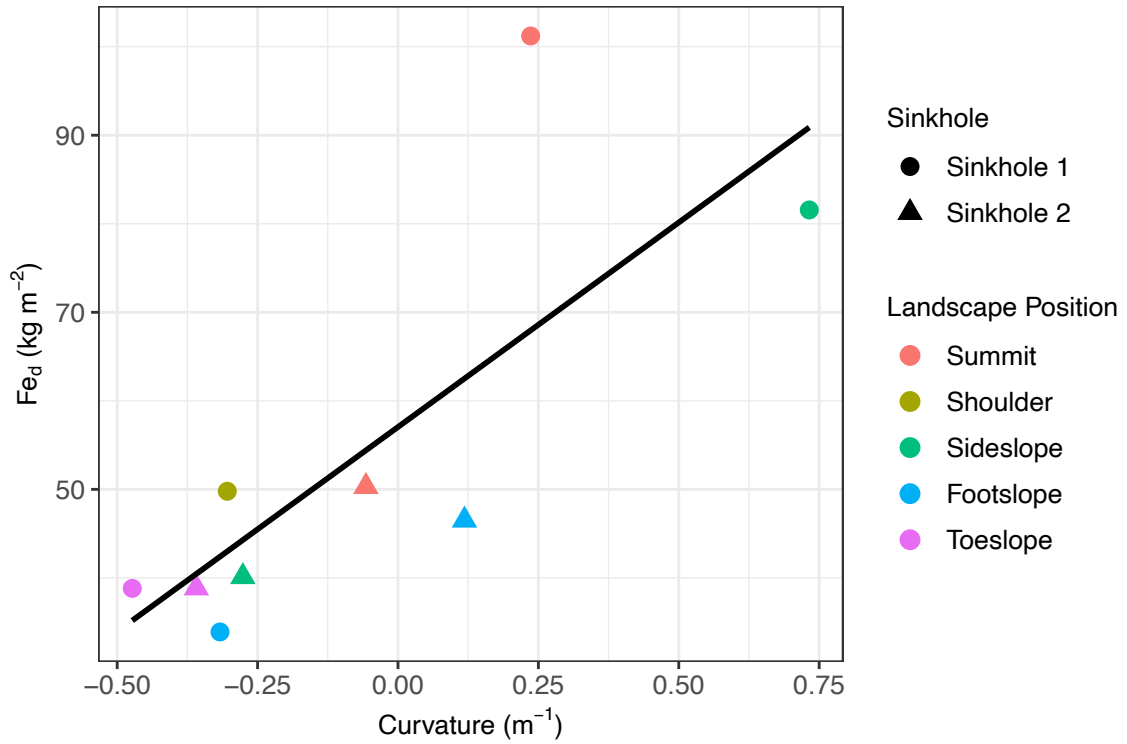


Figure 18. Dithionite-extractable Fe (kg m⁻²) exhibited a positive relationship with curvature (m⁻¹). Here, negative values are concave positions and positive values are convex positions. (Spearman's ρ : 0.85, p-value: 0.006, df: 7).

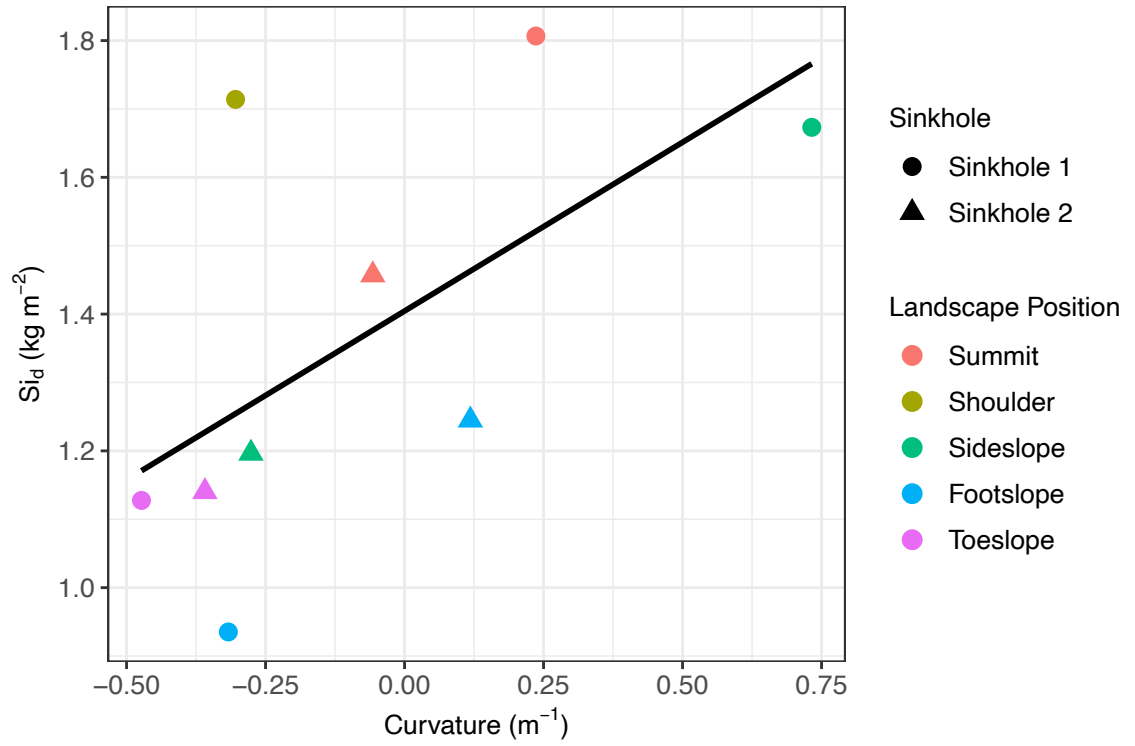


Figure 19. Dithionite-extractable Si ($kg\ m^{-2}$) exhibited a positive relationship with curvature (m^{-1}). (Spearman's ρ : 0.73, p-value: 0.031, df: 7).

2.3.3 Controls on total carbon, total nitrogen, and C:N ratios

There were several dominant controls on total carbon, total nitrogen, and C:N ratios in the sinkhole toposequences. Total carbon exhibited a negative relationship with both Al_d (Spearman's ρ : -0.47; **Fig. 20**) and Fe_d (Spearman's ρ : -0.55; **Fig. 21**), which did not support our third hypothesis. Further, we did not find significant relationships between exchangeable Ca (Spearman's ρ : -0.08; **Fig. 22**) or clay content (Spearman's ρ : -0.32; **Fig. 23**) and total carbon. Since these trends were weaker and opposite than what was expected, this result suggested that these soil components were less associated with soil C storage.

While the absolute magnitude of dithionite-extractable Fe and Al did not relate to total C, total N, or C:N ratios, the ratios of short-range-order or organo-complexed metals to crystalline metal oxides indicated strong significant relationships across the toposequence. The ratio of Fe_o/Fe_d provides a measure of the fraction of short-range-order/poorly crystalline Fe oxyhydroxides and organo-complexed Fe to crystalline Fe oxide phases (Schwertmann and Taylor, 1989; Kleber et al., 2005); whereas the Fe_p/Fe_d ratio indicates the fraction of organo-complexed Fe to crystalline Fe oxides. We observed strong, significant relationships between both Fe_o/Fe_d and Fe_p/Fe_d and total C, total N, and C:N (**Figs. 24-25**). Relationships between Fe_o/Fe_d and total C, total N, and C:N resulted in Spearman's ρ of 0.87 ($p= 0.0025$), 0.88 ($p= 0.0016$), and 0.75 ($p= 0.02$), respectively. Relationships between Fe_p/Fe_d and total C, total N, and C:N resulted in Spearman's ρ of 0.82 ($p= 0.0072$), 0.93 ($p= 0.0002$), and 0.68 ($p= 0.04$), respectively.

Following partial least squares regression model fitting, a PLSR model with two components explained the greatest variation in total C, total N, and C:N (**Fig. 26 and 27**). The coefficients for the PLSR model with two components are in **Table 2**. Based on the

PLSR results, silt, exchangeable potassium (Exch. K), and pyrophosphate extractable Mn (Mn_p) exhibited positive relationships with total C, total N, and C:N ratios (**Fig. 28**). In general, elevation and slope, exhibited negative relationships with total C, total N, and C:N ratios. In addition, sand content, exchangeable sodium (Exch. Na), and oxalate extractable Si (Si_o) exhibited negative relationships with total C, total N, and C:N ratios. Soil physical and chemical properties, such as clay content and dithionite-extractable Fe and Al, exhibit weak relationships with total C, total N, and C:N. This was surprising as these variables are routinely correlated with total C and N soil stocks.

Based on the coefficients from the full PLSR model, we produced a more parsimonious model (**Fig. 29**). We included variables with coefficient values that were either <-0.1 or >0.1 , which included: Slope, Mn_p , Silt, Exch. K, pH KCl, and EC (electrical conductivity). Using this smaller set of variables, the best model was fit using one component; the cross-validated R^2 values for total C, total N, and C:N were 0.80, 0.91, and 0.04, respectively, and the cross-validated RMSEP values were 0.43, 0.28, and 0.92, respectively. The model performed well for total C and N, but performed poorly for C:N, and was largely not capable of reproducing the observed C:N values.

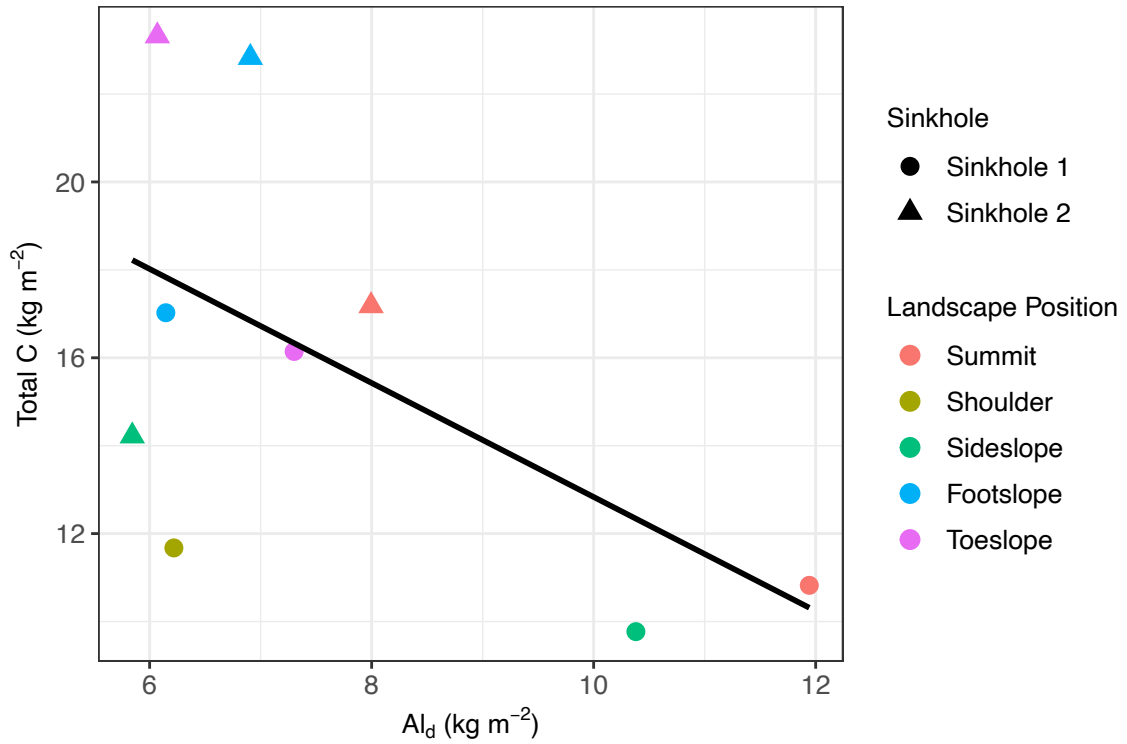


Figure 20. Total C ($kg\ m^{-2}$) exhibited a negative relationship with dithionite-extractable Al ($kg\ m^{-2}$). This did not support our third hypothesis. (Spearman's ρ : -0.47, p-value: 0.21, Degrees of Freedom: 7).

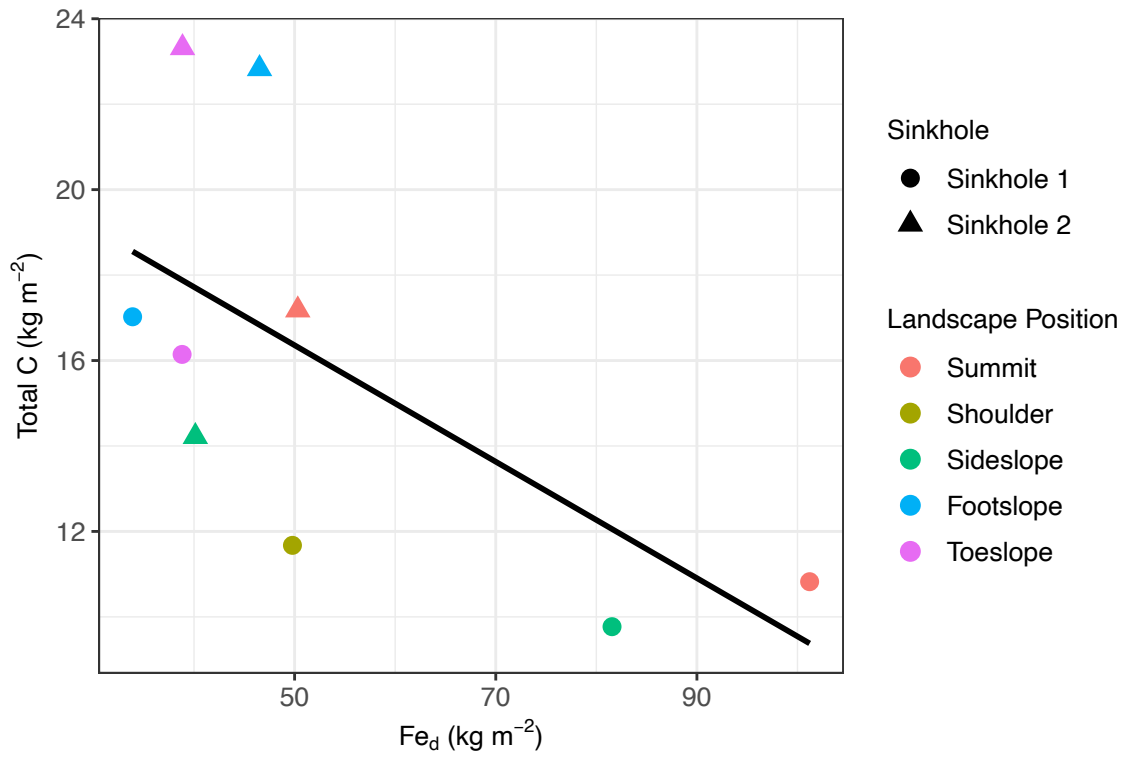


Figure 21. Total C (kg m⁻²) exhibited a negative relationship with dithionite-extractable Fe (kg m⁻²). This did not support our third hypothesis. (Spearman's ρ : -0.55, p-value: 0.13, Degrees of Freedom: 7).

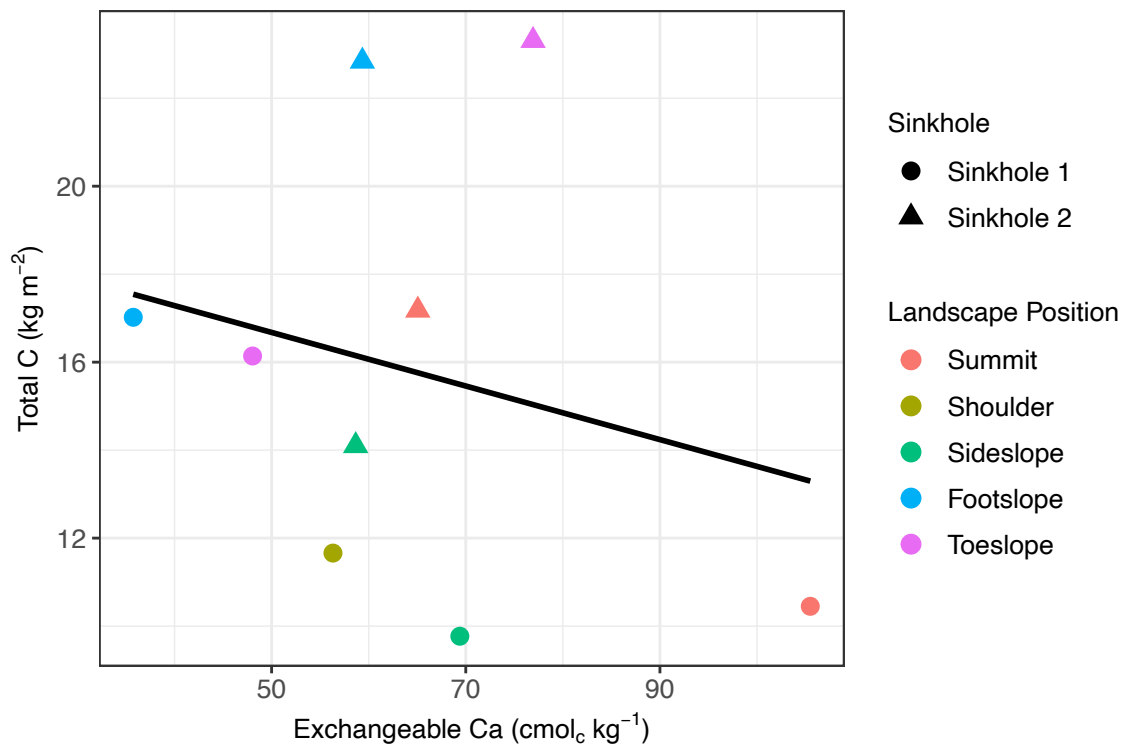


Figure 22. Total C (kg m⁻²) showed a negative relationship with exchangeable Ca (cmol_c kg⁻¹). (Spearman's ρ : -0.08, p-value: 0.84, Degrees of Freedom: 7).

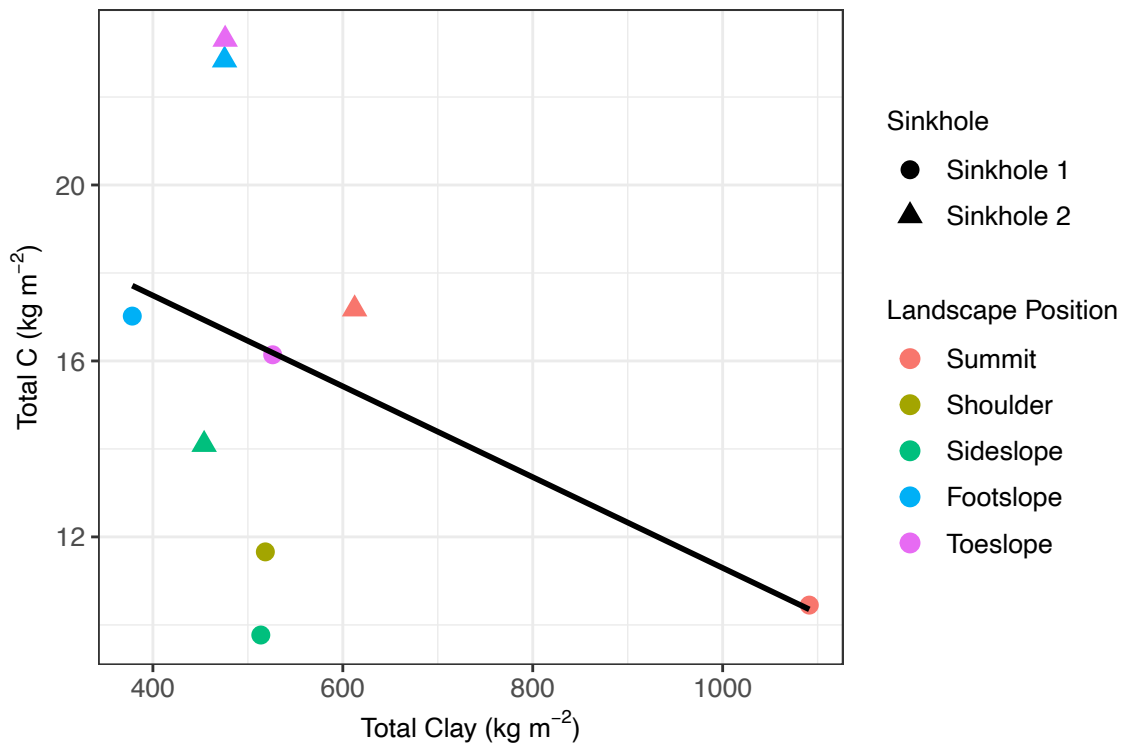


Figure 23. Total C (kg m⁻²) exhibited a weak negative relationship with total clay (kg m⁻²). (Spearman's ρ : -0.37, p-value: 0.41, Degrees of Freedom: 7).

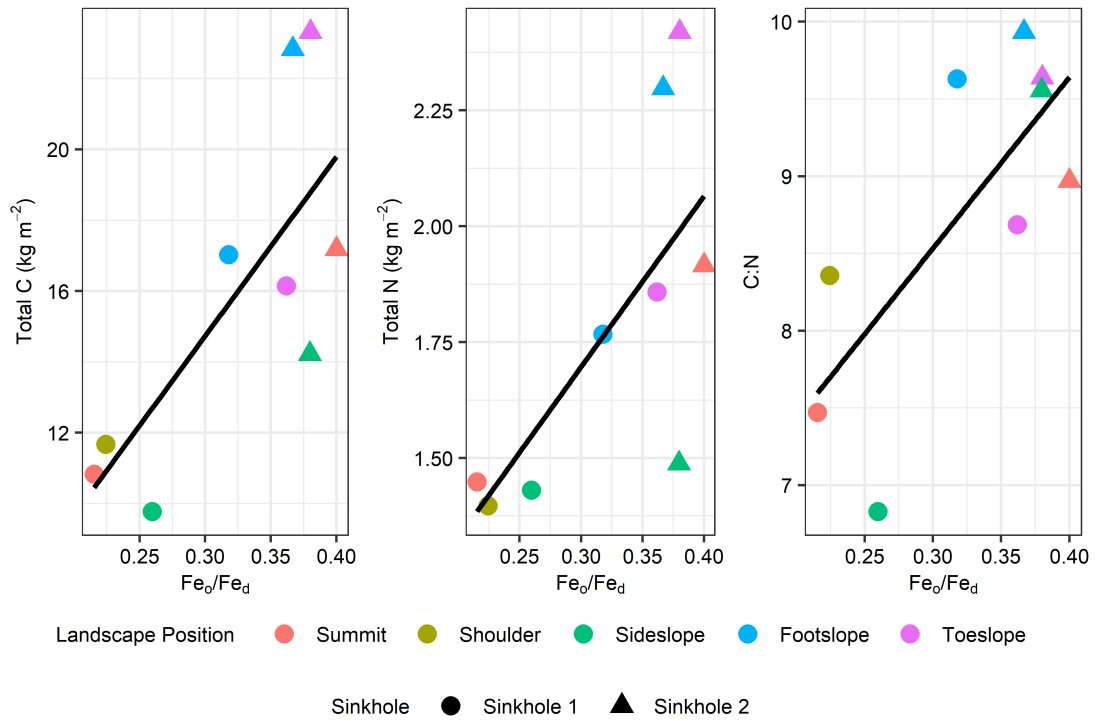


Figure 24. Relationships between Fe_o/Fe_d ratios with Total C ($kg\ m^{-2}$), Total N ($kg\ m^{-2}$), and C:N ratio.

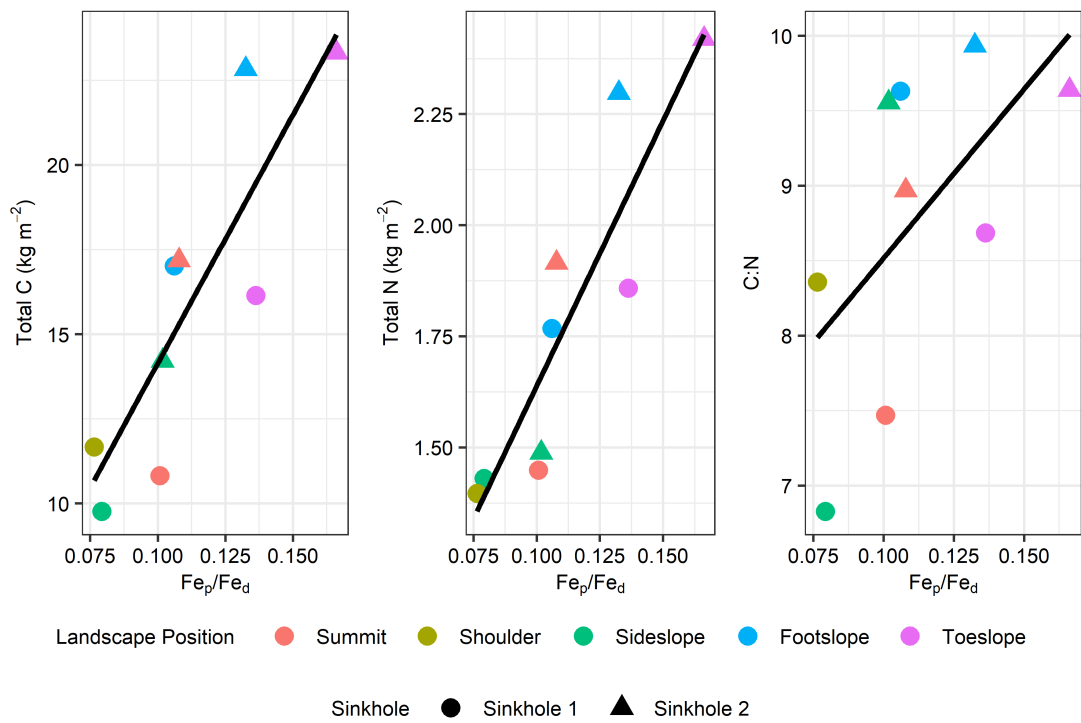


Figure 25. Relationships between Fe_p/Fe_d ratios with Total C ($kg\ m^{-2}$), Total N ($kg\ m^{-2}$), and C:N ratio.

Table 2. Regression coefficients for the full PLSR model using a suite of geomorphic, chemical, and physical properties using two components.

	Total C (kg m⁻²)	Total N (kg m⁻²)	C:N
Elevation (m)	-0.084	-0.083	-0.068
Slope (%)	-0.122	-0.130	-0.073
Aspect (radians)	-0.090	-0.091	-0.068
Curvature (unitless)	-0.046	-0.037	-0.058
Fe_d (kg m⁻²)	-0.075	-0.067	-0.080
Al_d (kg m⁻²)	-0.064	-0.055	-0.074
Mn_d (kg m⁻²)	0.007	0.014	-0.013
Si_d (kg m⁻²)	-0.093	-0.089	-0.082
Fe_o (kg m⁻²)	-0.008	0.006	-0.043
Al_o (kg m⁻²)	0.040	0.054	-0.003
Mn_o (kg m⁻²)	-0.002	0.009	-0.029
Si_o (kg m⁻²)	0.013	0.018	-0.001
Fe_p (kg m⁻²)	0.013	0.030	-0.031
Al_p (kg m⁻²)	-0.017	-0.003	-0.049
Mn_p (kg m⁻²)	0.112	0.115	0.081
Si_p (kg m⁻²)	-0.082	-0.074	-0.083
Clay (kg m⁻²)	-0.038	-0.028	-0.054
Silt (kg m⁻²)	0.116	0.122	0.077
Sand (kg m⁻²)	-0.030	-0.030	-0.021
Exch. Ca (cmol₍₊₎ kg⁻¹)	-0.003	0.011	-0.038
Exch. Na (cmol₍₊₎ kg⁻¹)	-0.083	-0.092	-0.042
Exch. K (cmol₍₊₎ kg⁻¹)	0.134	0.145	0.075
Exch. Mg (cmol₍₊₎ kg⁻¹)	0.019	0.035	-0.024
pH H₂O	0.041	0.057	-0.007
pH KCl	0.101	0.118	0.036
pH CaCl₂	0.071	0.087	0.015
Electrical Conductivity (μS cm⁻¹)	0.132	0.148	0.063

Table 3. Regression coefficients for the simple PLSR model using a suite of geomorphic, chemical, and physical properties using one component.

	Total C (kg m ⁻²)	Total N (kg m ⁻²)	C:N
Slope (%)	-0.222	-0.230	-0.151
Mn_p (kg m⁻²)	0.235	0.244	0.160
Silt (kg m⁻²)	0.234	0.243	0.160
Exch. K (cmol₍₊₎ kg⁻¹)	0.233	0.242	0.159
pH KCl	0.139	0.144	0.095
Electrical Conductivity (μS cm⁻¹)	0.206	0.214	0.141

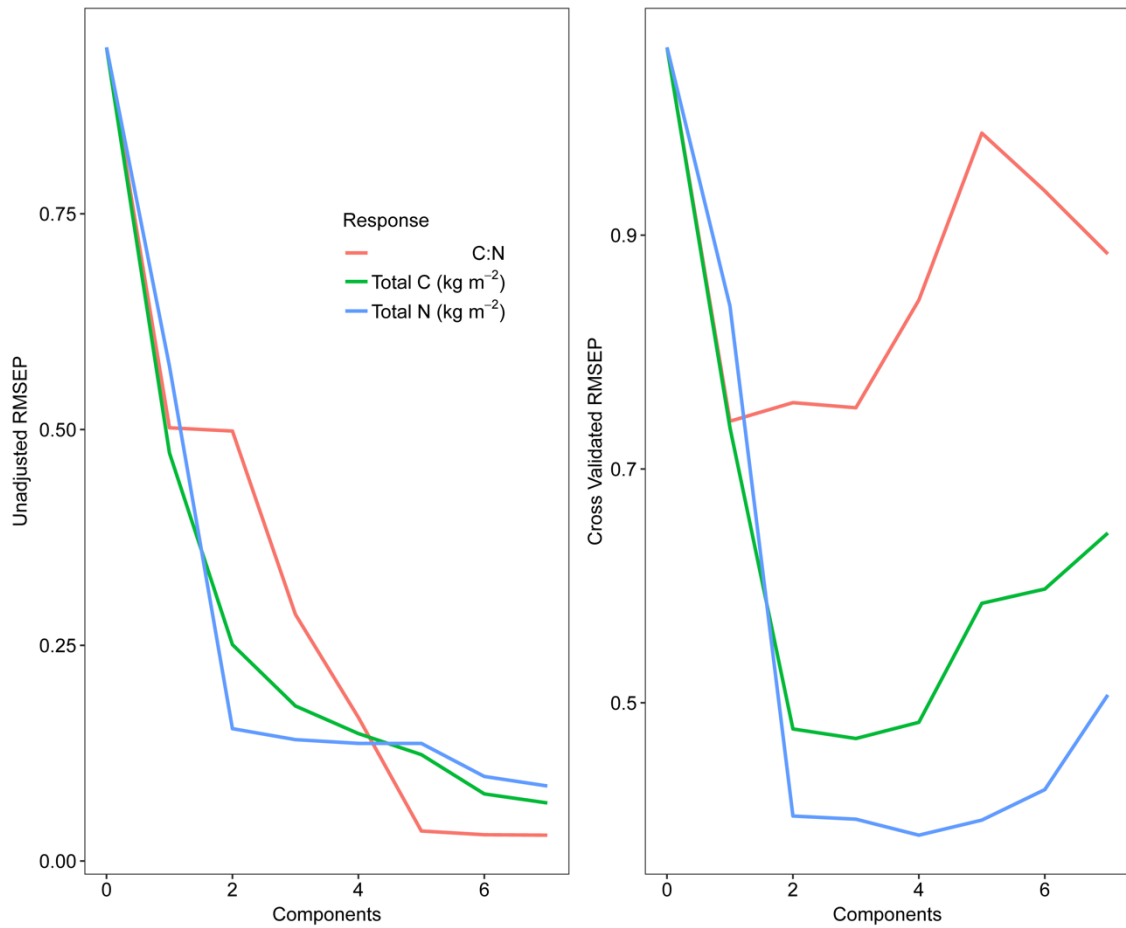


Figure 26. Change in root mean square error of the prediction from the PLSR with the number of included components for total C, total N, and C:N for the full PLSR model. Unadjusted RMSEP (left) indicated that substantial differences in RMSEP do not occur following two components. Cross-validated RMSEP demonstrated the lowest RMSEP with included components.

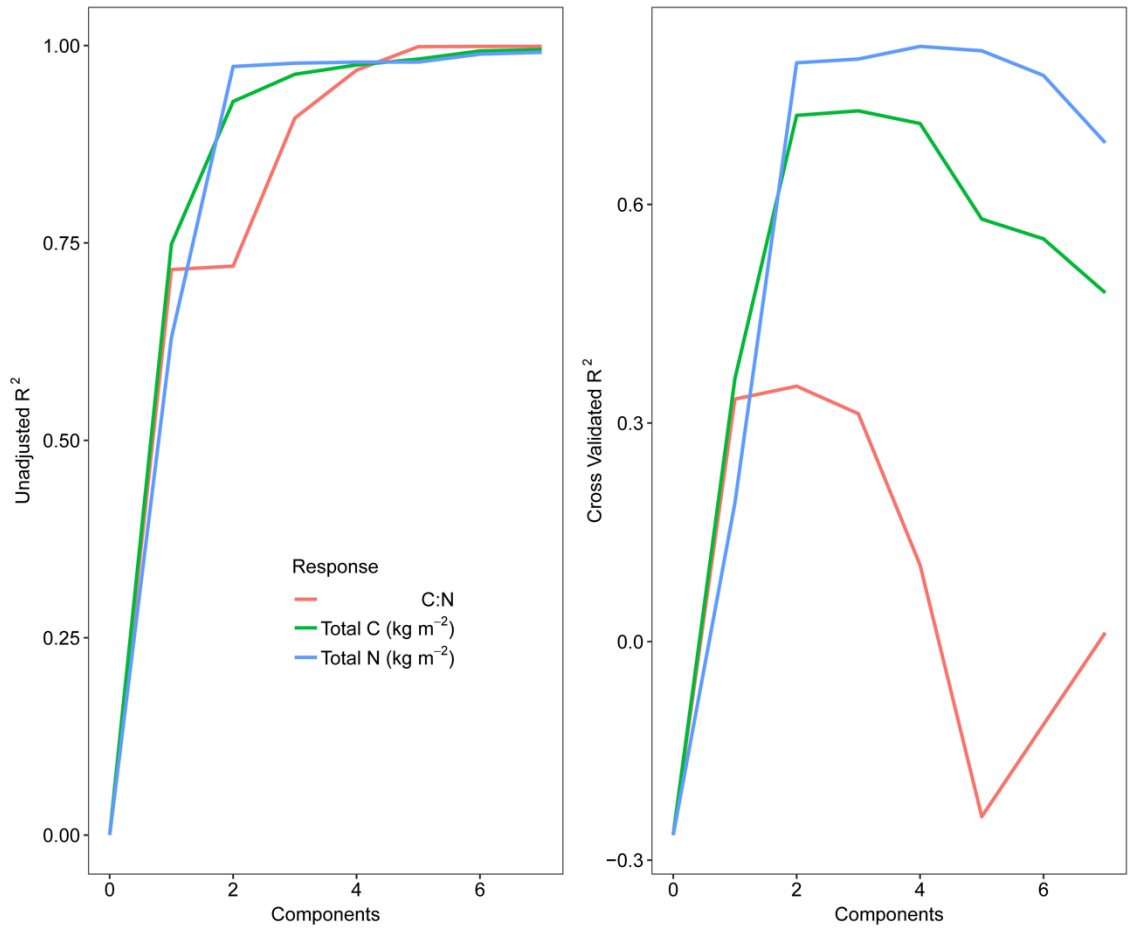


Figure 27. Change in r^2 with PLSR model components for the full PLSR model. Similar to RMSEP, no significant differences were observed in r^2 following two components (left). Cross-validated was greatest using two components (right).

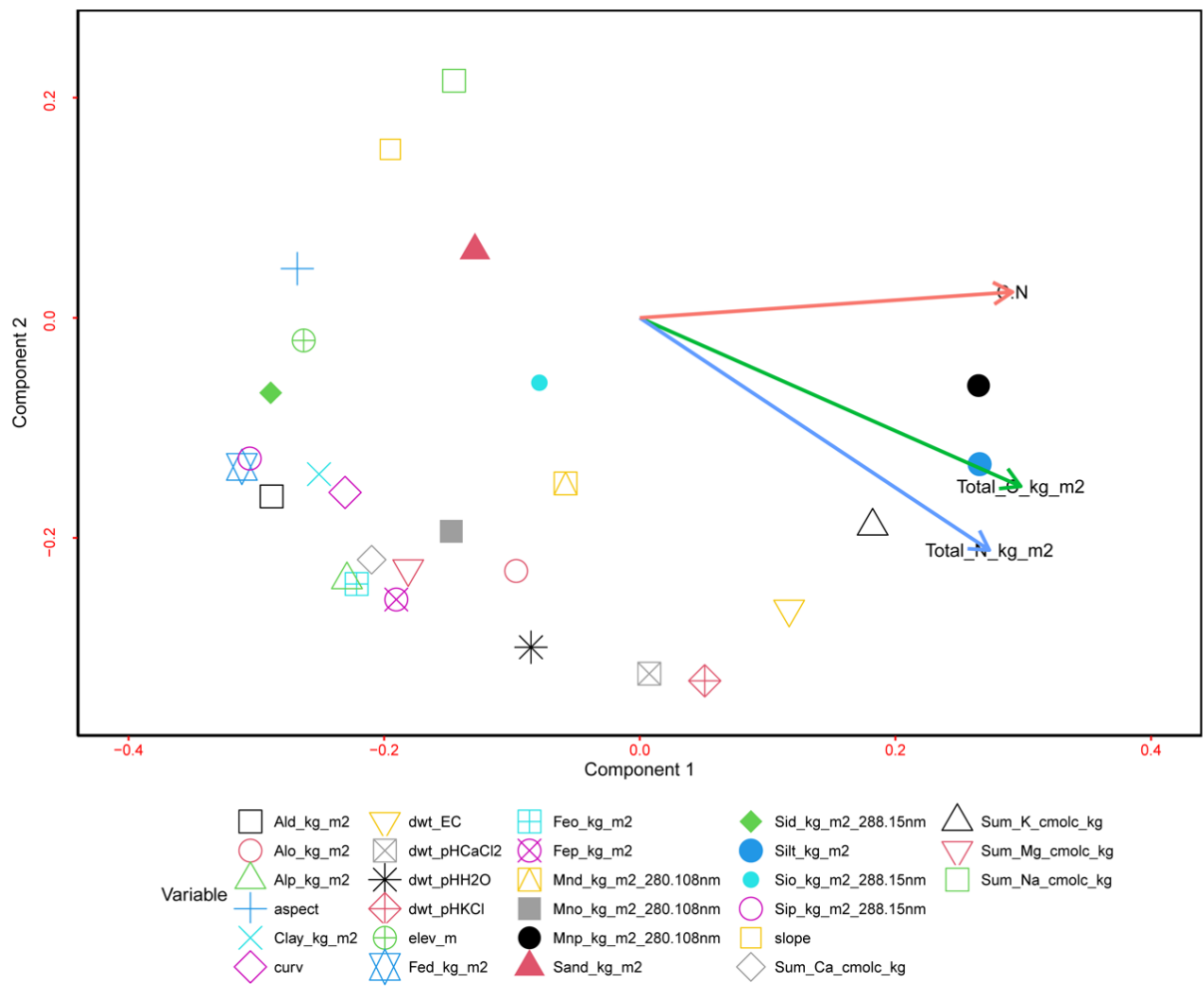


Figure 28. PLSR loadings biplot between the explanatory variables, represented as different shapes and colors, and the response variables, represented as arrows for the full PLSR model. The orientation of the arrows relative to the explanatory variables explain the positive and negative drivers of total C, total N, and C:N.

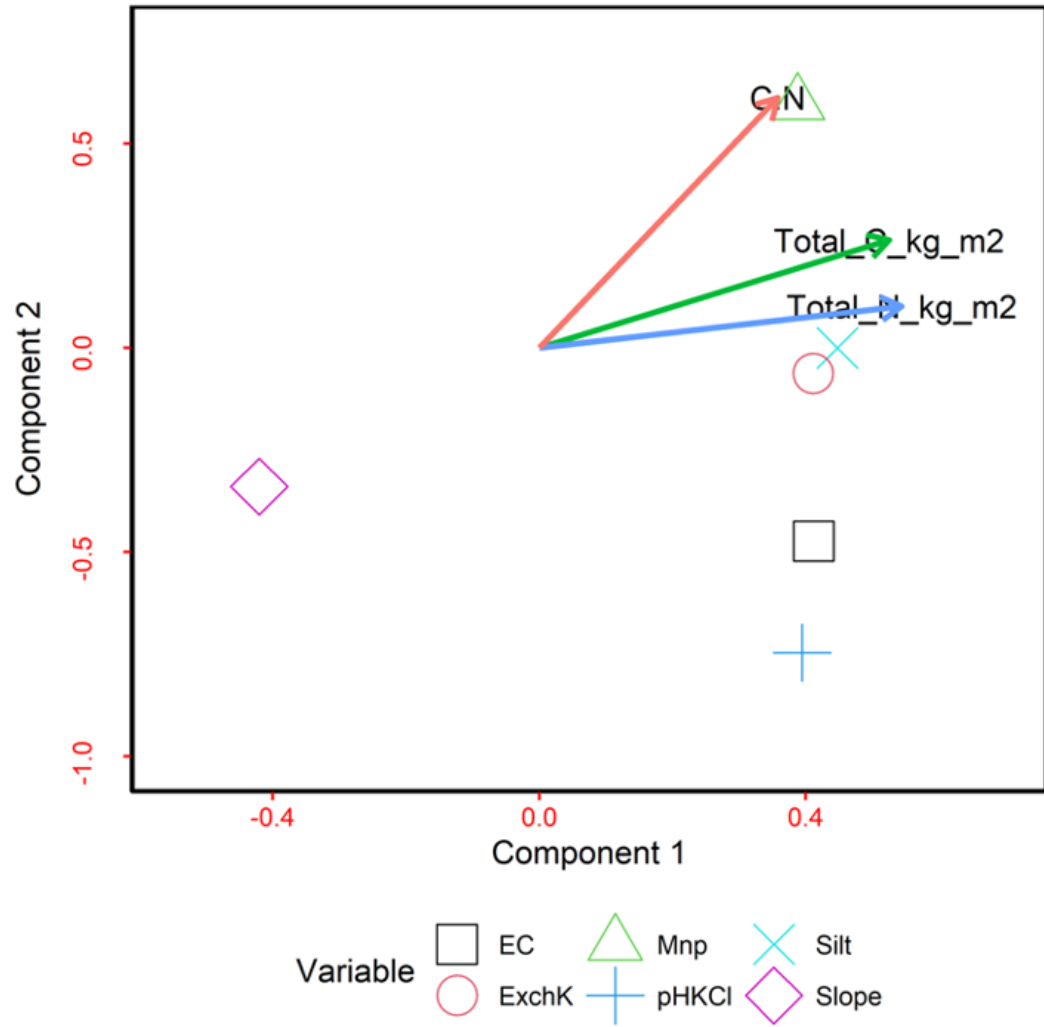


Figure 29. PLSR loadings biplot for the simplified PLSR model with only variables that had coefficient values either <-0.1 or >0.1 .

2.3.4 Soil Trends with Depth

When considering total carbon, we observed that sinkhole 2 contained greater carbon concentrations at most sampling depths (**Fig. 30**). In both sinkholes there was an increase in total carbon in the second horizon from the soil surface in the toe- and footslopes. Total N (kg m^{-2}) generally decreased with depth and followed similar patterns as total C, but we noted slightly higher total N concentrations with depth, especially in sinkhole 1 (**Fig. 31**). Carbon to nitrogen ratio depth trends in sinkhole 2 were consistent across all positions, with C:N values ranging from 8 to 10 (**Fig. 32**). Carbon to nitrogen depth trends in sinkhole 1 exhibited a significant decrease with depth in the summit, sideslope, and shoulder landscape positions. Similar C:N trends were observed in the sinkhole 1 foot- and toeslope positions, but the decreases with depth were slightly weaker.

Similar trends in particle size distribution were observed in both sinkholes; the highest clay percentages were found in the subsurface at the summit positions (**Fig. 33**). Overall, we found sinkhole 2 had lower clay percentages compared to sinkhole 1 at most sampling locations. We observed a substantial clay increase with depth in the summit position of sinkhole 1. The clay content in the toeslope of sinkhole 1 decreased to about 100 cm depth before increasing again, with the highest clay percentages observed at the final sampling depth (approximately 175 cm). This clay depth profile was different from sinkhole 2, which exhibited a general decrease in clay content through the entire profile.

Dithionite-extractable Al (Al_d) showed fairly similar trends across all hillslope positions with the exception of the summits (**Fig. 34**). A large increase in Al_d was observed in sinkhole 1 at approximately 90 cm, and a similar increase was observed in the summit position of sinkhole 2 but was slightly deeper in the profile (approx. 110 cm). Dithionite-

extractable Al also increased around 100 cm at both toeslopes. Dithionite-extractable Fe (Fe_d) was generally higher in sinkhole 1, especially at higher sampling locations (**Fig. 35**). In sinkhole 1, Fe_d demonstrated the clearest differentiation of landscape positions, with increasing Fe_d concentrations across all depths from the toeslope to the summit positions. A similar differentiation of Fe_d across landscape positions was less clear in sinkhole 2. Similar to the trend of Al_d , Fe_d increased with depth in the summit positions to approximately 100 cm before decreasing again.

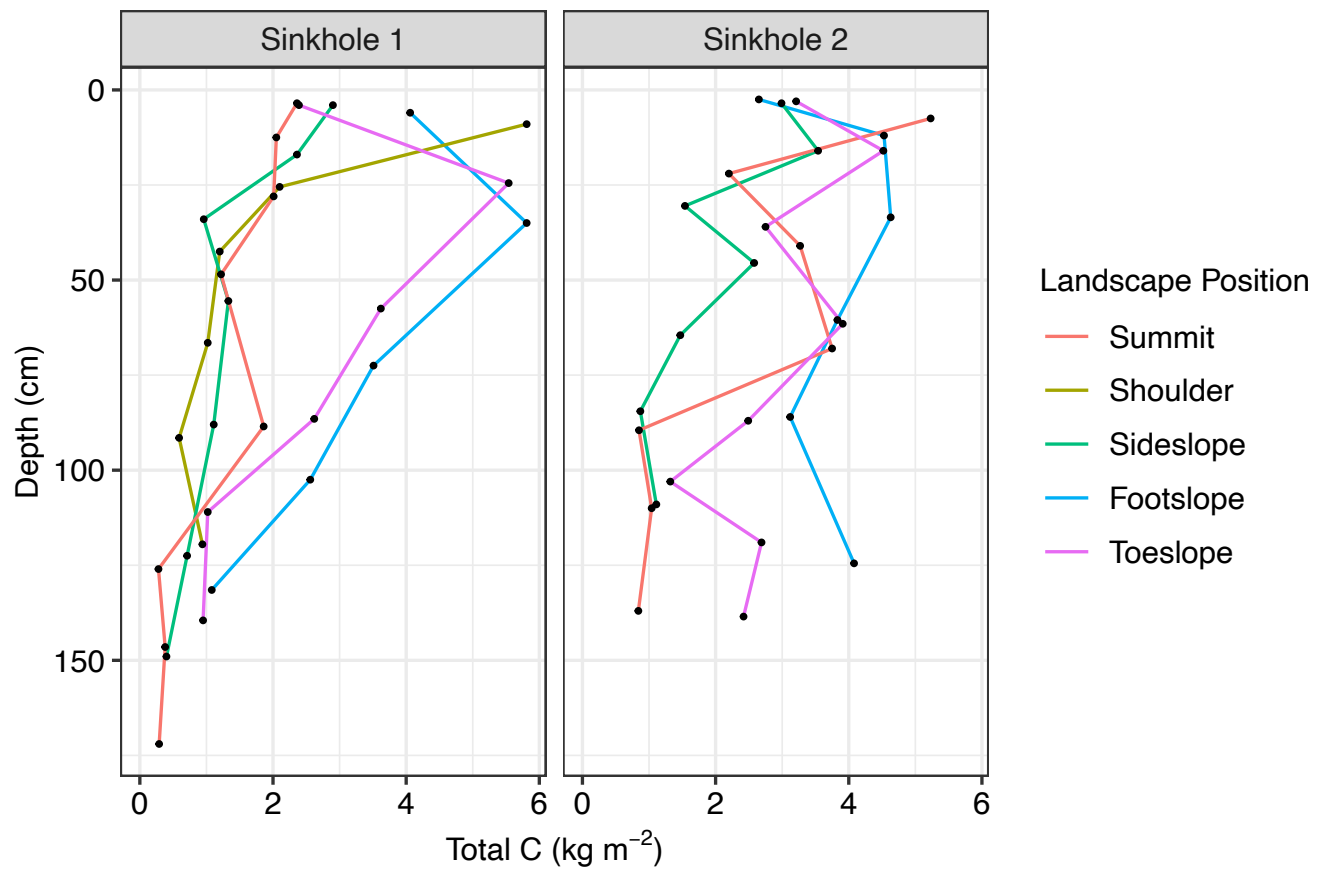


Figure 30. Total C (kg m⁻²) generally decreased with depth (cm), and was overall higher in sinkhole 2.

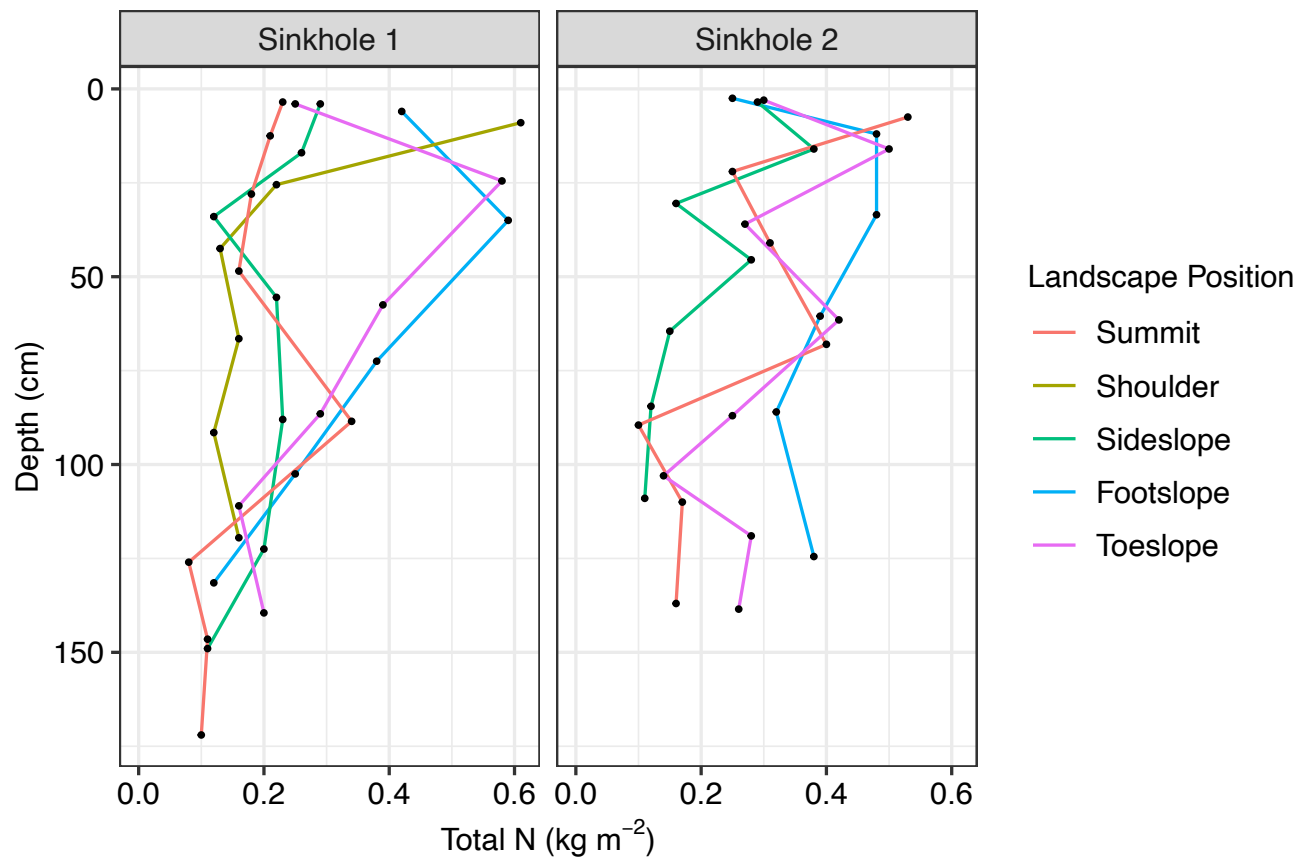


Figure 31. Total N (kg m⁻²) generally decreased with depth (cm) and was higher in the lower hillslope positions.

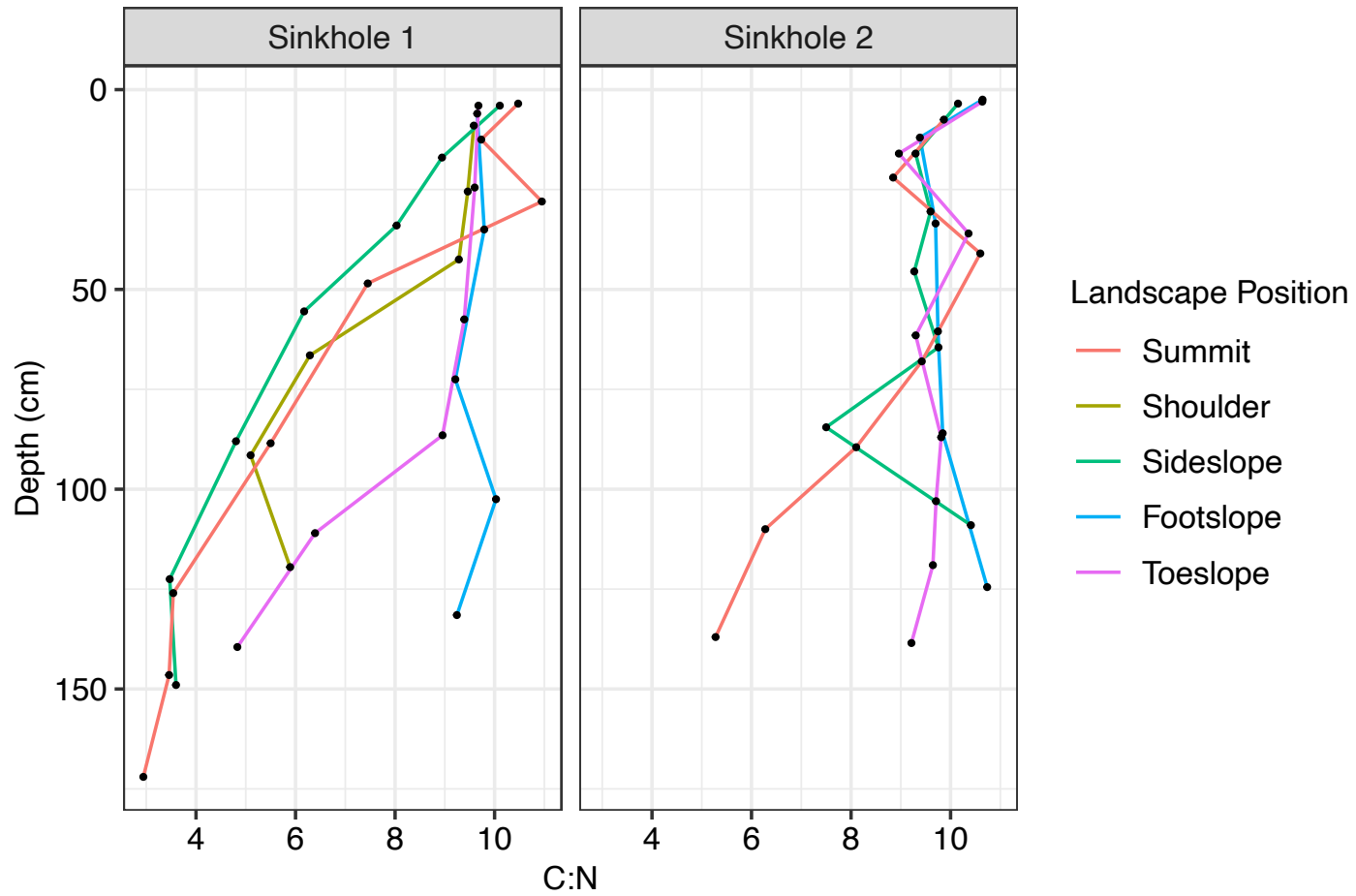


Figure 32. C:N was generally higher in sinkhole 2, and stayed higher with depth (cm) from the soil surface at most hillslope positions.

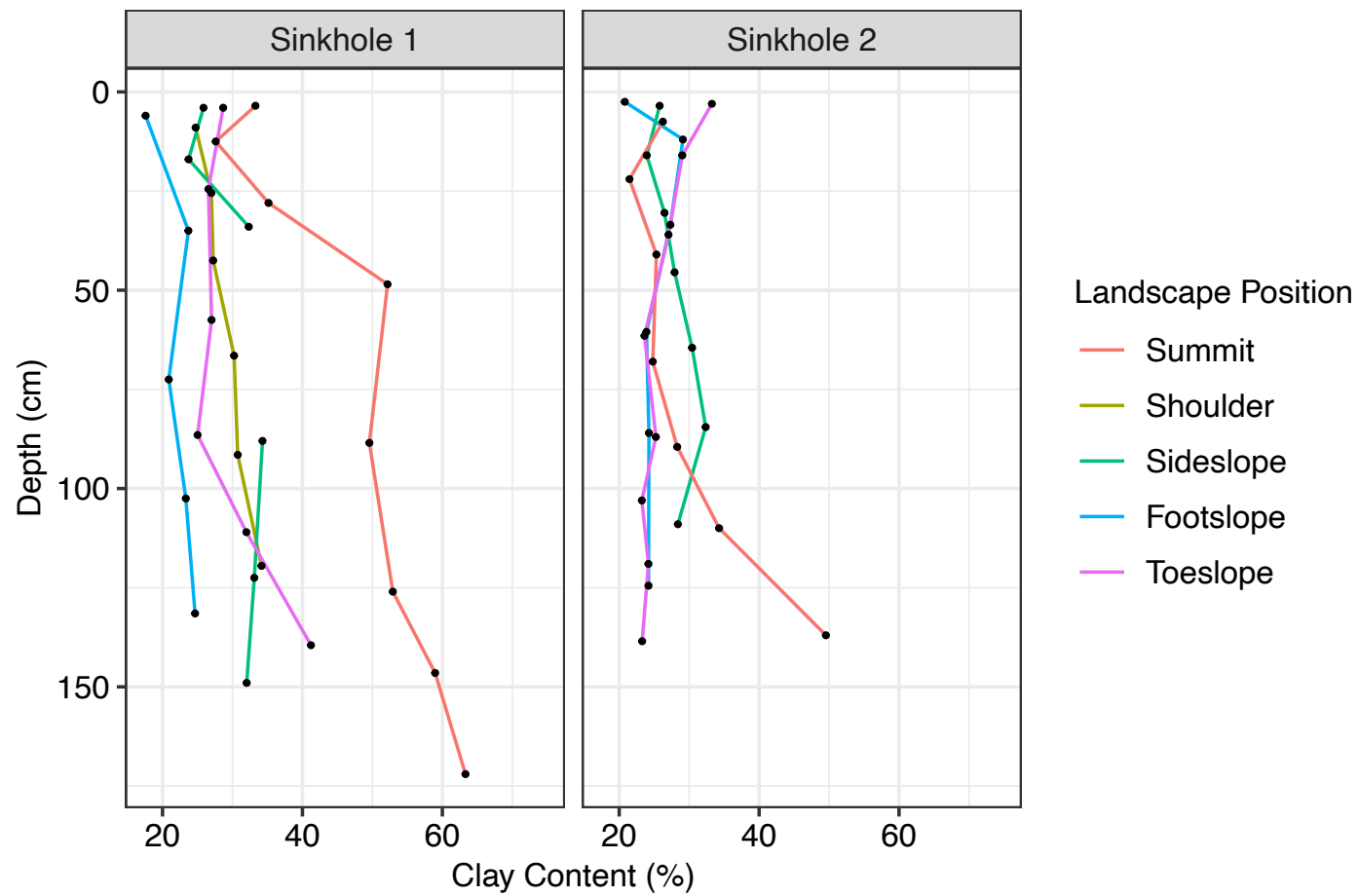


Figure 33. Total clay content (%) increased the most with depth (cm) at the summit locations of both study sinkholes.

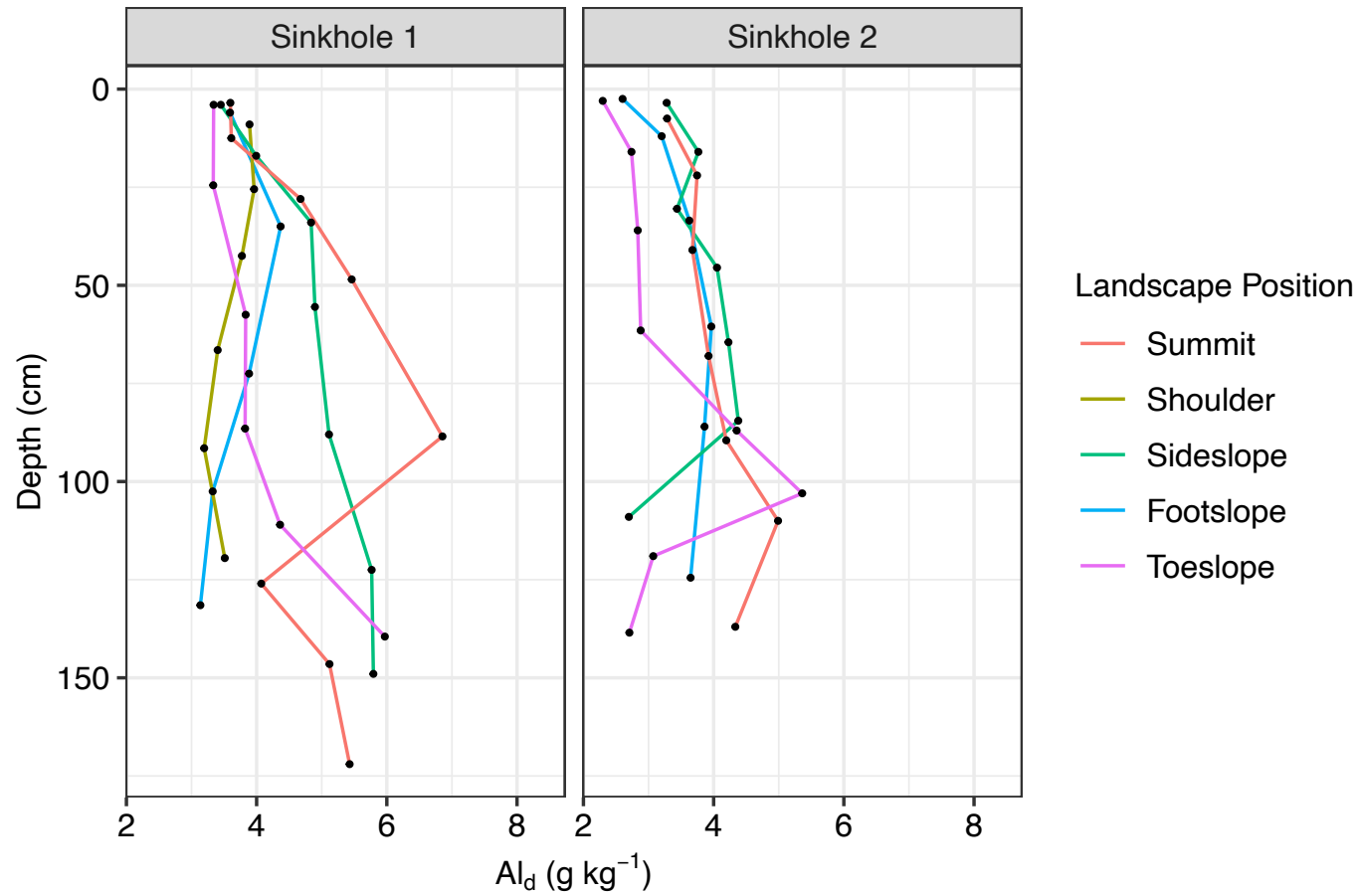


Figure 34. Dithionite-extractable Al (Al_d ; $g\ kg^{-1}$) was slightly higher in sinkhole 1, and remained relatively constant with depth (cm).

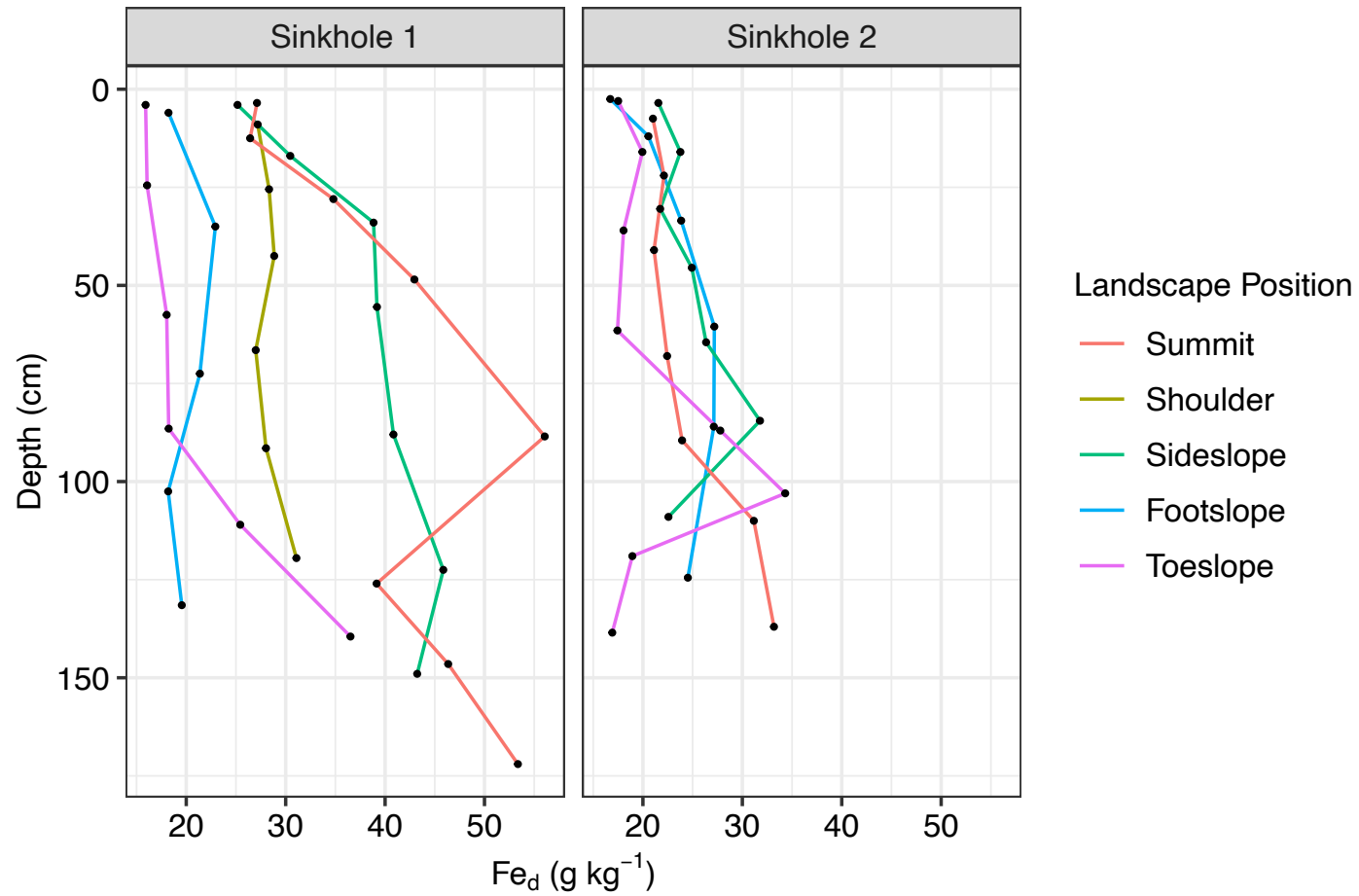


Figure 35. Dithionite-extractable Fe (Fe_d; g kg⁻¹) was much higher in sinkhole 1 with depth (cm).

2.3.5 Clay Mineralogy

Clay minerals labeled on all sample diffractograms (**Figs. 37-40**) are vermiculite (15-14 Å), mica (10.0, 5.0, 3.36 (in samples without quartz), and 2.5 Å), kaolinite (7.2 and 3.57 Å), quartz (4.26 and 3.35 Å), and goethite (4.18, 2.69, and 2.45 Å). We identified kaolinite in all samples. Kaolinite is a 1:1 phyllosilicate with no water interlayer, it also has a lower exchange capacity relative to other clay minerals (Grim, 1968). Kaolinite was identified on diffractograms by peaks at approximately 7.2 and 3.6 Å that collapse with heat (i.e., no identified kaolinite peaks in slides heated to 550°C). Treatment of the magnesium-saturated slide with glycerol does not affect the 7.2 Å kaolinite peak. Mica was also identified in all study samples. It was determined that mica was present and not halloysite because the halloysite peak changes from 10 Å to 7.2 Å with heat before collapsing at 550°C, which was not observed in study samples. The saturation of clay slides with K fills the interlayers of mica, preventing any collapse with heat treatment and maintains the diagnostic peak at 10 Å with a secondary peak at 5 Å.

Vermiculite is identified by a 15-14 Å peak that shifts with heating to 550°C, and a 10 Å peak that increases in intensity also with heating to 550°C (Hajirasouli et al., 2010). Vermiculite is a phyllosilicate, and a common intermediate weathering product in the transformation of biotite and mica (Malla, 2002), and is common in Inner Bluegrass soils (Prawito, 1996) and in other soils formed over carbonates (Singer, 1993; Egli et al., 2008).

In sinkhole 2, a trace of chlorite is also present in the BC horizon based on the presence of the 14 Å peak in the Mg-glycerol slides and its persistence with heating in the K + 550°C slide (Fig. 38). Additional experiments will be performed to evaluate whether chlorite is present in the Ap horizon from this sinkhole.

Goethite was identified in all of the pits chosen for analysis with XRD. Goethite is identified by peaks at 4.18, 2.69, and 2.45 Å. Goethite peaks collapse with higher heat and were therefore not identified in samples heated to 300°C and 550°C. The presence of goethite agrees with the low Fe_o/Fe_d ratios, which range from 0.1-0.4 (McKeague and Day, 1966; Schwertmann, 1993). Goethite is an iron oxide, and therefore important for forming associations with soil organic matter.

Quartz was identified in most soils. It was identified by peaks at 4.26 and 3.35 Å. The quartz peaks are not affected by any treatment and thus the 4.26 Å peak is often used as an internal standard against which other peaks can be adjusted. If a peak was noted at 3.35 Å but there was not a 4.26 Å peak present, this was identified as another mica peak. Quartz was not identified in the bottom of the summit pit in sinkhole 1.

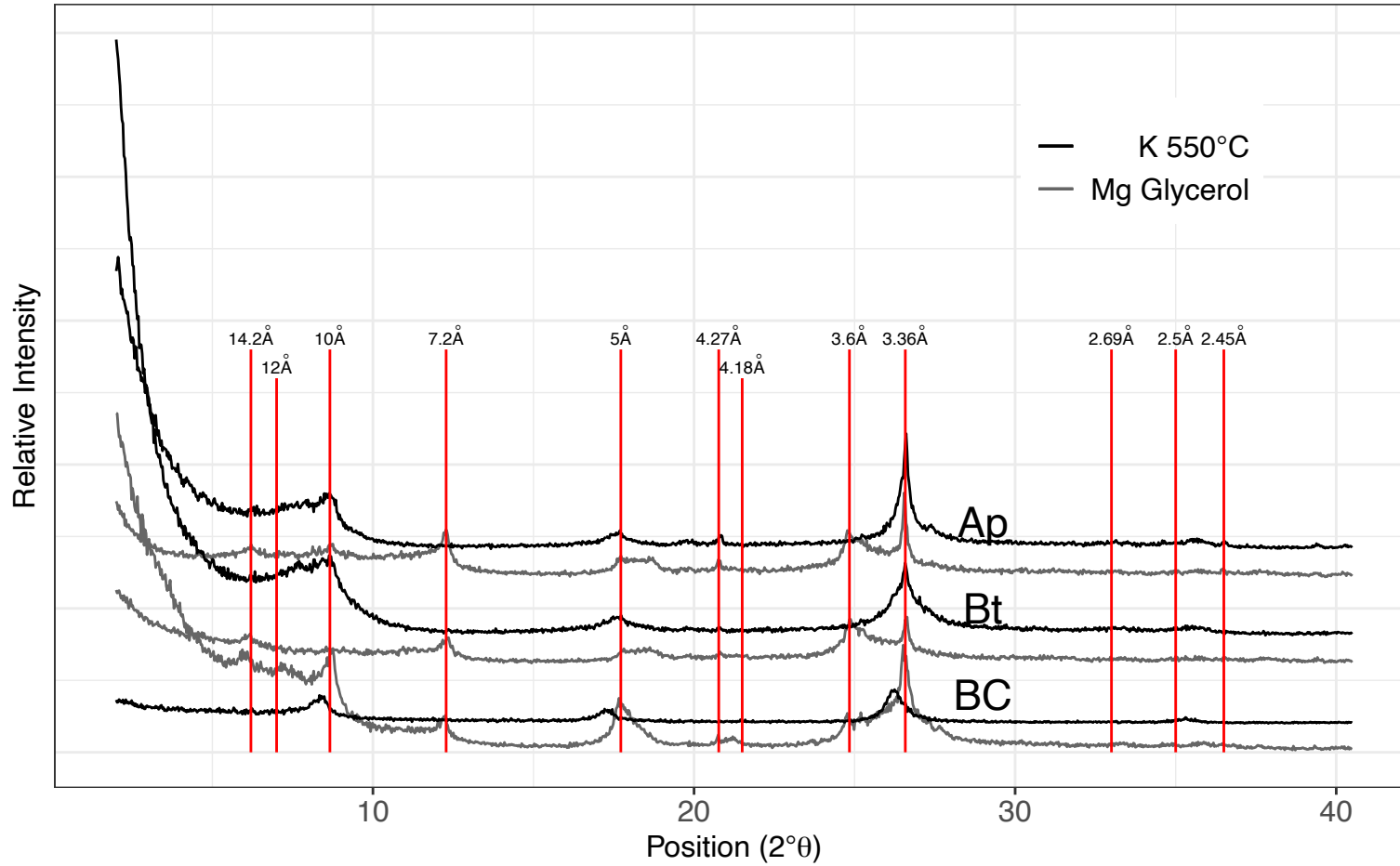


Figure 36. Diffractogram for sinkhole 1, summit pit. Select horizons are shown with 2 treatments.

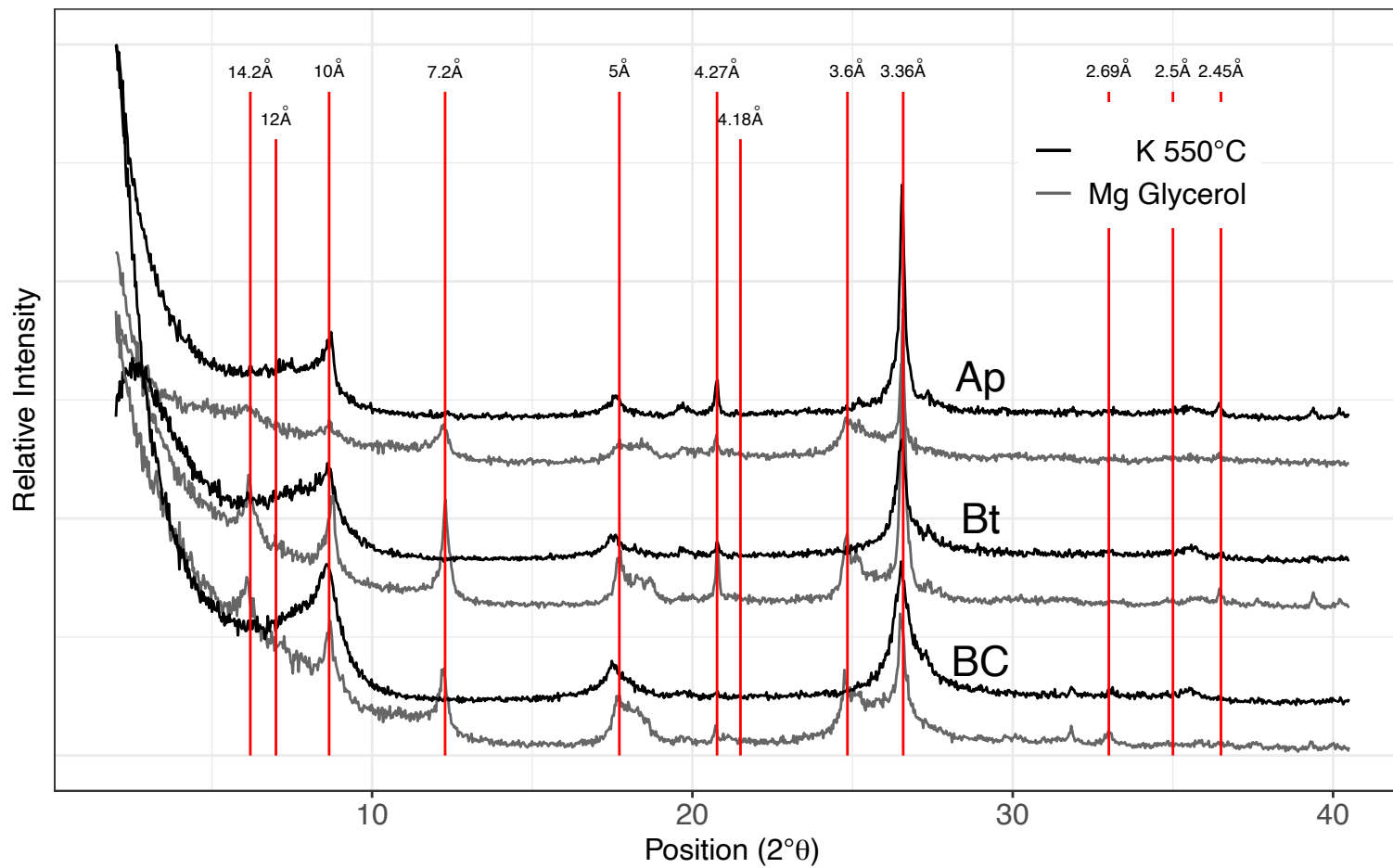


Figure 37. Diffractogram for sinkhole 1, toeslope pit. Select horizons with two treatments are shown.

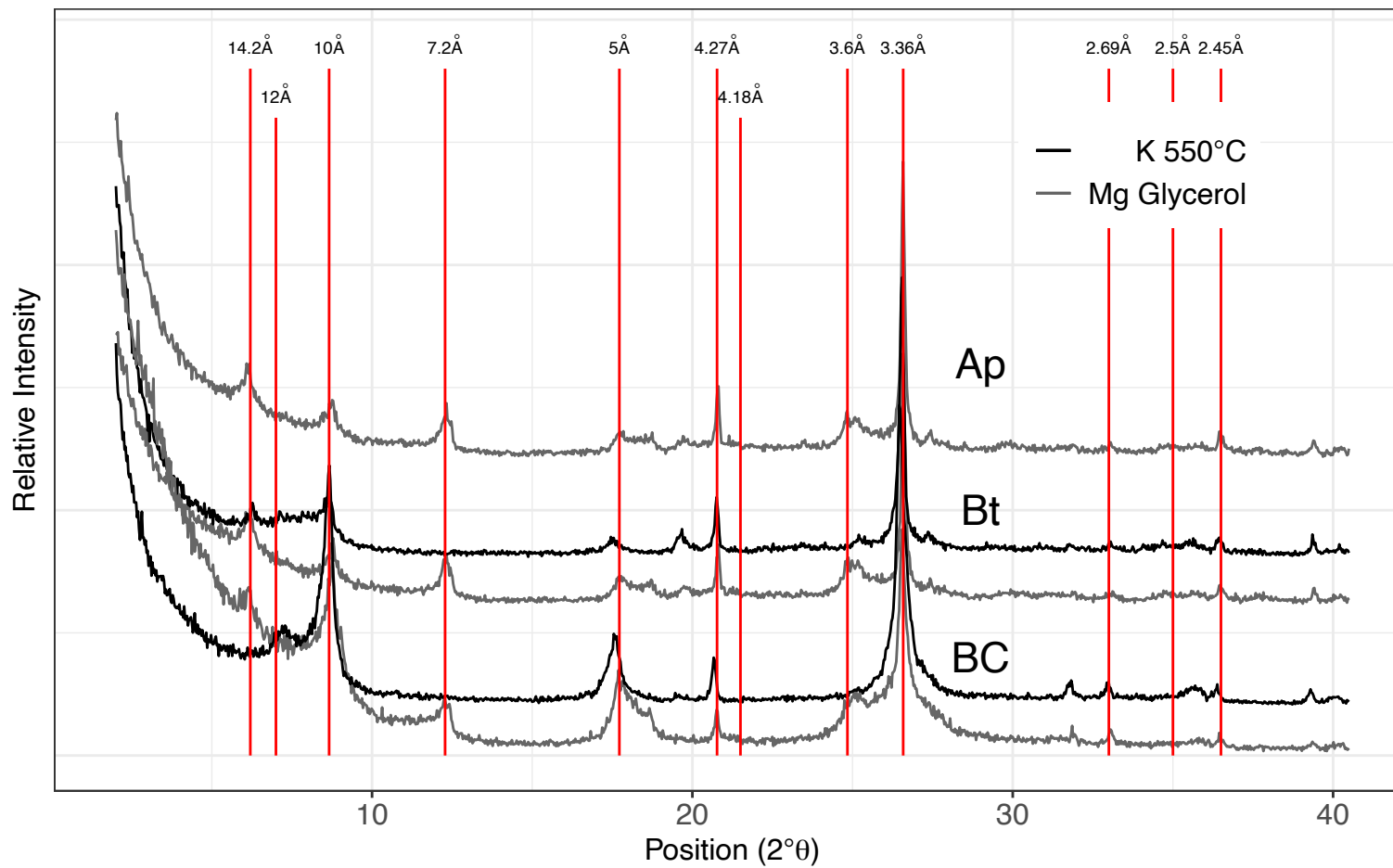


Figure 38. Diffractogram for sinkhole 2, summit pit. Select horizons with two treatments are shown.

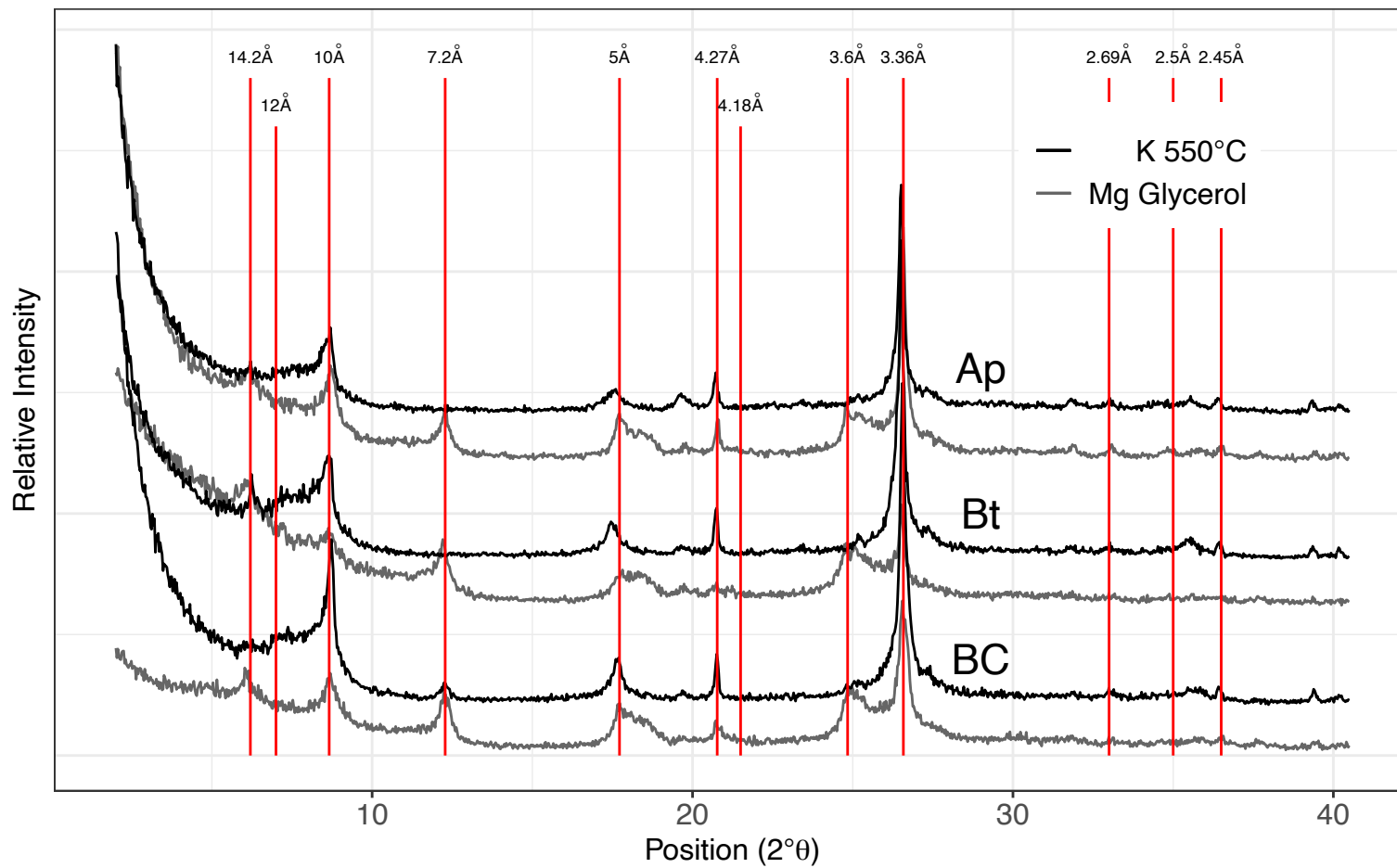


Figure 39. Diffractogram for sinkhole 2, toeslope pit. Select horizons with two treatments are shown

2.4 Discussion

2.4.1 Topographic Controls on Bulk Soil Properties

Topography alters microclimate and local additions and losses of matter and energy from the soil profile (Hunckler and Schaetzl, 1997; Birkeland, 1999; Rasmussen et al., 2015; Pelletier et al., 2018). Landscape position specifically exerts large control over the redistribution of water, sediment, ions, and minerals (Jenny, 1941; Schimel et al., 1985; Applegarth and Dahms, 2001). In subsidence sinkholes, the reactants and products of weathering are temporarily concentrated before being lost from the system. As observed here, topography and landscape (e.g., hillslope) position still control soil properties in these karst features.

While subsidence sinkholes maintain a fairly circular, bowl-like shape throughout their evolution (Delle Rose et al., 2004; Radulović, 2013), which should concentrate pedogenic processes; from the observed results, karst features are likely disruptive to pedogenesis by altering microclimate and increasing fluxes of matter and energy which limits pedogenic processes. In the present study, common hallmarks of pedogenesis, such as clay content and metal oxide concentrations were substantially lower in the toeslope, or sinkhole base, as compared to the summit. In the described soil toposequences, we observed less crystalline and amorphous metal oxide concentrations and substantially less clay content in the base of the sinkholes compared to the summit positions. This result was similar to the toposequences described in Prawito (1996), who found higher C levels in sinkhole bases compared to higher landscape positions (**Fig. 41**), and also found less clay in the toeslopes and more in the summit positions surrounding these features (**Fig. 42**).

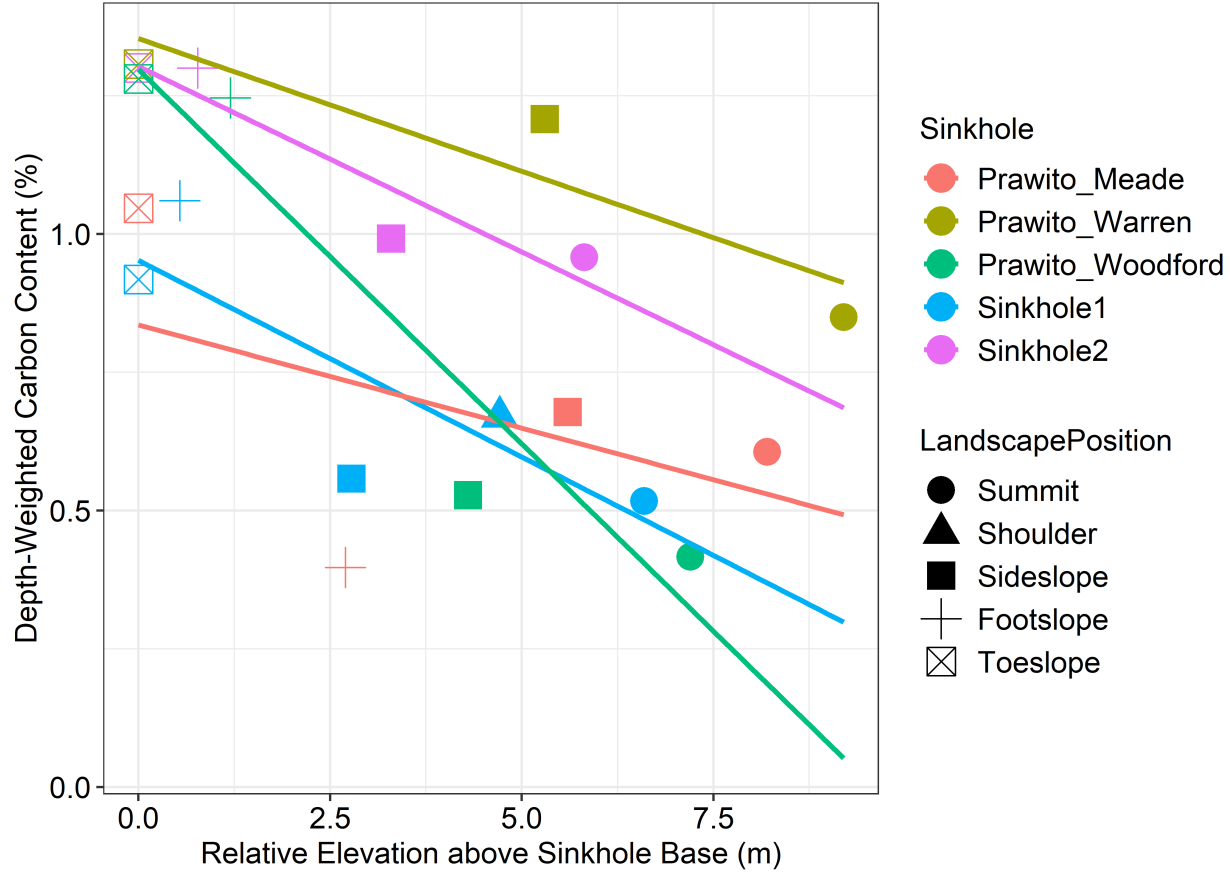


Figure 40. Depth-weighted C (%) showed a negative relationship with relative elevation (m) for both the current study sites and Prawito (1996).

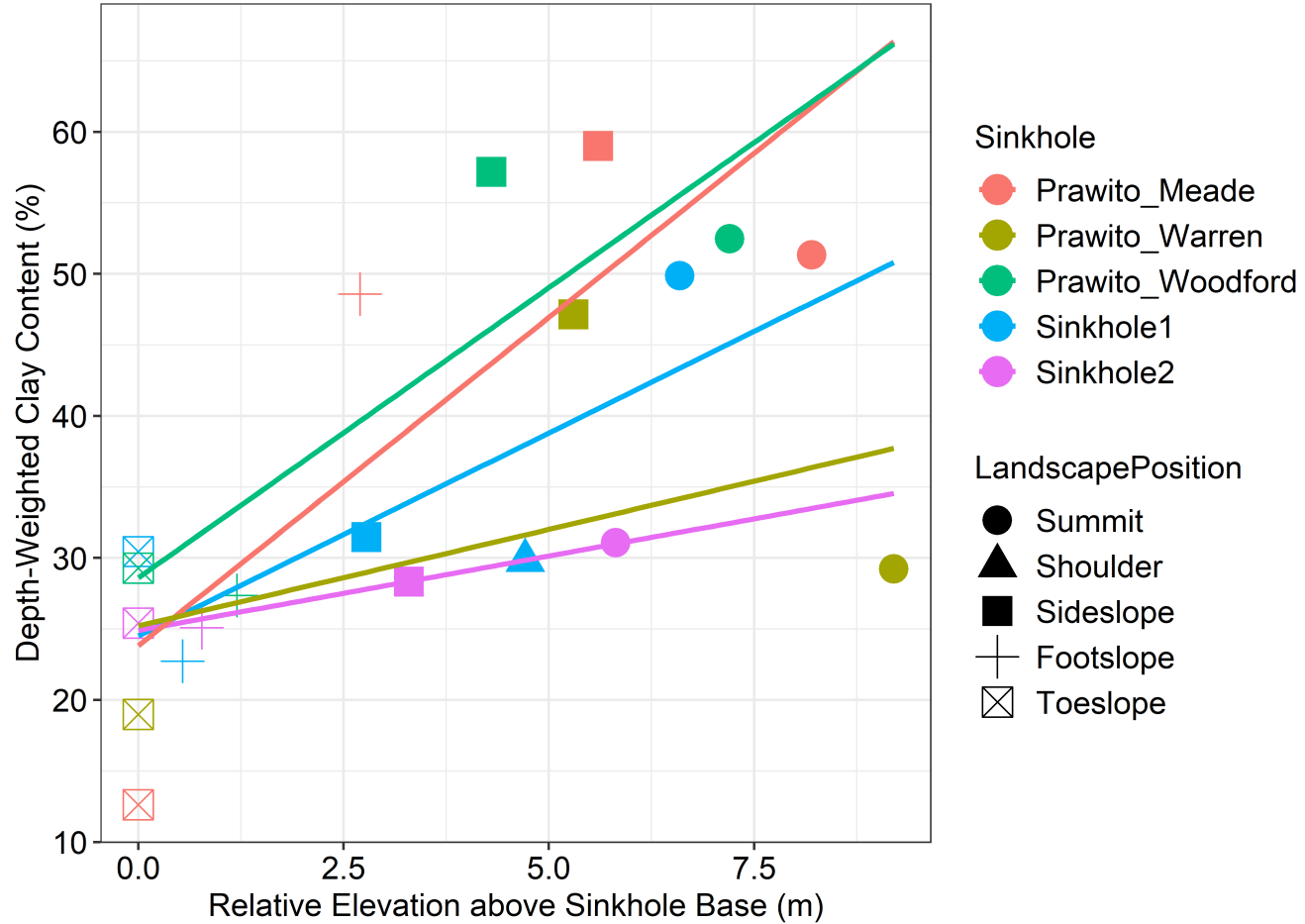


Figure 41. Depth-weighted clay (%) exhibited a positive relationship with relative elevation (m) for both this study's sites and the sites from Prawito (1996).

While these observations confirmed our hypotheses that elevation and other topographic variables exert a large control on pedogenesis and bulk soil properties, the trends that we observed were largely opposite of what we expected. A possible explanation is that slope and curvature, and not elevation, are largely responsible for constraining pedogenesis in these features. Locally in Kentucky, flatter and more stable landscape positions are found with better developed argillic horizons compared to soils formed on steeper slopes (Karathanasis et al., 1991). In both sinkhole toposequences, depth to the first Bt horizon was shallower in the summit than it was in the sideslopes. The Bt horizons in both summit positions were also thicker, indicating more advanced argillic development compared to other landscape positions (see **Table 1**). Additionally, we found strong relationships between Fe_d and Si_d concentrations and curvature, with more convex sites having greater concentrations compared to concave sites. This result contradicts other past work which found that concave positions should contain more free oxides (Swanson, 1985).

Soils at the base of the sinkhole were weakly developed compared to the soils at the sinkhole summits (Frumkin et al., 2015). Sinkhole formation and evolution likely disrupts pedogenesis through a constant flux of sediment out of the soil profile into karstic features or fractures below the soil column. The greater turnover of soil materials likely does not allow enough time for weathering processes to generate secondary clays and metal oxides in the sinkhole bases (Yoo et al., 2007; Yoo and Mudd, 2008b). The sinkhole bases are also more consistently wet, which may result in observed mineralogical differences. For example, hematite may be dissolved preferentially compared to goethite under moister hydroregimes (Boero and Schwertmann, 1987). This may explain the reduced redness

rating values as a function of elevation, however, evidence of wetness, such as redoximorphic features, were not observed in the toe- or footslope profiles of either sinkhole.

Topography also influences soil weathering and therefore mineralogy (e.g., Yoo et al., 2009; Lybrand and Rasmussen, 2015). The same study from west-central Kentucky mentioned above found that kaolinite was more abundant in upland soils (Karathanasis et al., 1991). While Karathanasis and Golrick (1991) focused on the influences of loess additions to sandstone soils, the modern soils from this study also identified vermiculite and mica, both of which were found in our study soils. Karathanasis and Golrick cited soil mixing (a result of topography) as an important predictor of the mineralogical composition of soils, which may also be a factor in the present study due to similarities in mineral assemblage between pedons. A study examined the mineralogy of soils along a toposequence in Iran (xeric moisture regime, mesic temperature regime) found similar clay minerals along their toposequence, but relative quantities of the identified minerals varied (Hajirasouli et al., 2010). Similarly, in the present study, we did not observe major differences between many of the identified minerals. Had quantitative mineralogy been done, it would have been possible to make comparisons in terms of amounts of minerals present. For example, in the case of goethite, this would be important for estimating how much of the carbon being stored in these features is due to mineral-organic associations.

Hajirasouli et al. (2010) identified drainage as an important factor in the variable mineral weathering rates that lead to mineralogical differences. While sinkholes collect water and are generally wetter in the base, karst lithologies are usually highly porous, meaning there often are not as many indicators of poor drainage or anaerobic conditions as

expected (Li et al., 2019). There were no identified redoximorphic features in the bases of our study sinkholes but even slight changes in duration of saturation can affect mineral weathering, with chemical weathering being the most intense in moist soils with high biotic activity (Dethier et al., 2012).

Soil carbon is tied to hillslope position, among other topographic factors (Hancock et al., 2010; Chirinda et al., 2014; Conforti et al., 2020). Carbon and nitrogen are redistributed across hillslopes (Berhe et al., 2007; 2018), which results in important soil organic matter transformations and storage dynamics. Similar to numerous other soil toposequence/catena studies, we found that the deeper and potentially wetter soils in the toe- and footslope positions contained greater amounts of carbon and nitrogen compared to the sideslope, shoulder, or summit positions (Chirinda et al., 2014; Conforti et al., 2020). While most past work was not examining karstic soils, we noted similar results in the present study, as higher total carbon concentrations were found in the sinkhole bases relative to the summit. On the local-landscape scale (i.e., 10s to 100s of meters), topographic variable such as elevation may primarily explain trends in soil carbon and nitrogen (Zhu et al., 2019).

2.4.2 Soil Carbon Storage in Karst Environments

Considering how widespread karst terrain is throughout the world, approximately 20% of the ice-free surface of the Earth (Ford and Williams, 2007), any trends with regards to carbon storage would have broad implications to how carbon in soils is quantified in these regions. Our results showed that total C was generally higher in the bases (foot- and toeslope sampling locations) of study sinkholes which suggests that these features act as carbon sinks. Trends in carbon storage and silt content across the hillslopes of the present study are complementary, which is not uncommon on most hillslopes (Litaor, 1992; Sollins et al., 1996; John et al., 2005), which may indicate that the soil carbon is less likely to be minerally-associated. This relationship may be driven by the preferential loss of clay-sized particles from the soil profiles in the sinkhole base/toeslopes to underlying karst features, which would enhance the relationship between silt and carbon.

While we did not find significant relationships between dithionite-extractable Fe or Al, clay content, or exchangeable Ca and total C, total N, or C:N ratios (Rasmussen et al., 2018), we did observe that the ratios of Fe_o/Fe_d and Fe_p/Fe_d explained trends in total C, total N, and C:N ratios across the soil toposequences. Soil organic matter adsorbs to the surface of metal oxides, which stabilizes and protects the organic matter from mineralization for substantial periods of time (Kaiser and Guggenberger, 2007; Nguyen et al., 2019). For example, the low Fe_o/Fe_d ratios are also indicative of goethite, which may explain the lack of red colors in the sinkhole toeslopes (Schwertmann and Taylor, 1989). Soil organic matter also has the potential to adsorb to goethite, which may explain the strong correlation between Fe_o/Fe_d and total carbon (Kleber et al., 2005; Kaiser and Guggenberger, 2007). Not surprisingly the relationship between Fe_p/Fe_d and total C, total

N, and C:N was strong, which was expected given that the Fe_p/Fe_d indicates the degree of Fe complexed by SOM. The relative proportion of SRO Fe oxides and organo-complexed Fe relative to crystalline or free Fe oxides may largely explain the trends in total C, total N, and C:N ratios observed in the study pedons.

In addition to the relationships between Fe_o/Fe_d and Fe_p/Fe_d , goethite was also reported in some of the pedons selected for XRD analysis. Goethite has been shown to readily form mineral-organic complexes, or associations (Tipping, 1981; Kaiser and Guggenberger, 2007; Nguyen et al., 2019). These associations both protect and stabilize SOC from microbial decomposition/mineralization (Schimel et al., 1994; Guggenberger and Kaiser, 2003; Keil and Mayer, 2013; Nguyen et al., 2019). The identification of goethite in study soils suggests that these complexes play an important role in SOC storage in these soils and also identifies a potential mechanism facilitating SOC storage. Shang and Tiessen (2003) also did not find relationships with sesquioxide content and SOM accumulation in the karst soils of the Yucatan Peninsula similar to our results here. However, unlike Shang and Tiessen (2003), we did find significant relationships with the relative proportion of poorly-crystalline or complexed oxides to crystalline oxides. One possible explanation is that the relative proportion of poorly crystalline oxides to crystalline oxides is a better indicator of available binding sites for organic matter compared to the absolute magnitude. A second possibility is that as material is constantly added to the sinkhole bases, a mix of minerals may be added from the surrounding hillslopes, such that the relative mix of mineralogy is a better predictor of soil carbon storage.

2.4.3 Implications for Karst Sinkhole Evolution

The size of karst sinkholes may be related to their age. However, the rate of dissolution of soluble bedrock and the removal of weathering products also influences sinkhole evolution. These weathering processes are variable and are controlled by climate as well as the soil thickness (Dong et al., 2019) and the age of the soil surface (Bautista et al., 2011). Dissolution of the bedrock below a sinkhole can be slowed by limited reactants (e.g., water limitation due to drought, CaCO_3 limitation due to depletion of bedrock, or soil depth) which would alter aboveground expression (Dreybrodt, 1988). Soil formation and pedogenesis would still occur but these processes would occur on more stable topography (assuming no more subsidence) and may link sinkhole evolution to soil development. Ultimately, unless a specific site has been consistently monitored, it is not possible to quantify the exact age at which the ground surface began to subside, however, studying the soils within these features may provide relative age estimates.

In karst terrains, landscape position stability plays an important role in profile development and horizonation. As these karst features age, they are generally deepening and widening, while gaining material from the surrounding landscape and exporting material to the epikarst and karst below the soil surface (Delle Rose et al., 2004). These processes (dissolution, openings in underlying bedrock, water movement through the feature) will continue as long as the reactants are present and the products are exported (Dreybrodt, 1988). If subsidence/dissolution slows or export of material becomes limiting, the soils within these features may experience greater pedogenesis, linking soil profile

morphology and properties to the onset of karst feature stability, thus providing a relative age.

For the present study's sites, there were no available historic records with details of feature growth. However, based on our observations, we expect that sinkhole 1 is an older feature relative to sinkhole 2. Sinkhole 1 is substantially larger than sinkhole 2 (Paylor et al., 2003). In addition, soils of sinkhole 1 had higher redness ratings as well as higher clay percentages compared to sinkhole 2. In general, sinkhole 1 also exhibited greater Fe_d concentrations. Based on the larger size, higher clay content, redness rating, and Fe_d concentrations, we expect that sinkhole 1 is an older feature compared to sinkhole 2. Since sinkhole formation and weathering are on-going processes, we would expect to observe that karst landscapes with substantial sinkhole distribution have more variable spatial distribution of bulk soil properties than previously anticipated. This spatial variability may have important implications in the development of karst, the weathering of soluble bedrocks, and larger-scale earth surface processes.

2.5 Conclusions

Sinkholes are abundant in the Inner Bluegrass, as well as globally, which makes them important features to include when considering how they influence biogeochemical cycling. As the climate continues to change, it will become increasingly important to understand how carbon cycles through and is stored in soils. The present work suggests that carbon is being held in higher amounts in the base of sinkholes relative to adjacent limestone soils under similar management. Greater integration of pedogenesis with our understanding of karst hydrology is needed to better identify the forms of carbon being lost, the rates of chemical weathering, and the role of soils in karst hydrologic functioning.

Consideration of the predicted climate and weather patterns, as well as vegetation, would be beneficial to the understanding of how sinkhole soils may impact karst hydrology over the next century.

CHAPTER 3. SUMMARY

The data presented in Chapter 2 demonstrated that the soil in karst subsidence sinkholes has identifiable trends related to hillslope position and depth that have the potential of being applied to other sinkholes in the study region. Sample depth and elevation (which was related to sampling location along the hillslope) explained many of the trends in bulk soil physical, chemical, and mineralogical properties. Soil carbon was of interest in this study because of its role in the global carbon cycle and the increasing need to understand exactly how carbon is cycled and stored in soils (Minasny et al., 2017). Since soils are the largest terrestrial sink of carbon (Jobbagy and Jackson, 2000) understanding the dynamics of carbon in various environmental systems, such as karst terrains, is needed.

If a sinkhole can be thought of as a bowl, there is a hillslope at every point along the sides of the bowl. The base of the sinkhole (where the toeslopes converge) will see the concentration of water and sediment that moves down slope. In the present study, the effect of this concentration resulted in high total carbon, which, as discussed in Chapter 2, will likely lead to increased C storage in these karst features.

There are, of course, different types of karst; limestone, dolomite, gypsum, and marble are all lithologies that are conducive to karst feature formation (Stokes et al., 2010). The combination of lithologies that differ in composition and purity, coupled with other

factors such as climate and structural controls means that karst is expressed differently. Although over half (approx. 55%) of Kentucky alone has observable karst features (Currens, 2012), the morphology is variable. For example, the upland areas of the Pennyroyal region of western KY are also underlain by limestone, but this region has rougher topography compared to the Inner Bluegrass, with more abundant sinkholes and knobs and elongated depressions (Newell, 2001). Even the subtle lithologic changes between the Inner and Outer Bluegrass change the observed karst feature expression.

Even though the factors controlling sinkhole expression might change, we expect the general trends identified to hold true across most sinkholes; water and sediments moving downslope will continue to be concentrated in the toeslope. An important finding from the present study was the presence of goethite in some samples. The mineral-organic complexes that often form with goethite slow or prevent the microbial degradation of organic matter, resulting in long term storage of SOC (John et al., 2005; Helfrich et al., 2007; Poeplau et al., 2013). Goethite is often present in more highly weathered soils, and is therefore expected in tropical environments where there is often karst. Hematite, another Fe oxide, is often more abundant in red, tropical soils and also forms associations that protect and store SOC.

Knowing that these features contain high amounts of carbon is important to understanding how they function in the context of not only their specific karst region, but also how they play into the global C cycle. Understanding the mechanisms that are controlling the increased C storage in karst sinkholes is vital to quantifying their potential to hold onto C for long periods of time in the future. Ensuring that these features are able to function naturally and without disruption in the form of intensive agricultural practices

or spreading urbanization is vital to maintaining the increased levels of C storage in these features.

Aside from carbon storage, dissolution sinkholes represent a unique karst feature that allows for the effect of a single soil forming factor (topography) to be studied. The present study examined bulk soil properties from 2 toposequences, both on the south-facing slope. In the future, it would be beneficial to examine the corresponding soils on the north-facing slopes. We expect to observe higher OM concentrations and potentially less-weathered minerals. Differences in both the amount of SOC stored and the mechanisms controlling storage would be important to identify.

Given the widespread occurrence of karst sinkholes, the results of the present study are widely applicable. It will be important to monitor changes to subsidence morphology and how soils are weathered. Changes to mineralogy with age have implications for carbon storage, as well as other nutrient storage. Connecting these changes to belowground systems represents a unique challenge that require a multidisciplinary approach.

APPENDIX

Sinkhole	Hillslope Position	Lab ID	Sample Depth (cm)	Total C (%)	Total N (%)	LOI	Bulk Density (kg/m ³)	C (mass per area kg m ⁻²)	N (mass per area kg m ⁻²)	Total C per sampling location	Total N per sampling location	Depth-weighted total C
Sinkhole 1	Toeslope	60	0-8	2.477	0.256	7.40%	1208.5	2.39	0.25	16.14	1.86	0.917403846
Sinkhole 1	Toeslope	61	8-41	1.392	0.145	5.24%	1207	5.54	0.58			
Sinkhole 1	Toeslope	62	41-74	1.202	0.128	4.72%	912.7	3.62	0.39			
Sinkhole 1	Toeslope	63	74-99	0.788	0.088	3.90%	1328.6	2.62	0.29			
Sinkhole 1	Toeslope	64	99-123	0.358	0.056	3.91%	1183.3	1.02	0.16			
Sinkhole 1	Toeslope	65	123-156	0.285	0.059	2.41%	1009.8	0.95	0.2			
Sinkhole 1	Toeslope	66	156+	0.187	0.047	5.14%		0	0			
Sinkhole 1	Footslope	67	0-12	2.741	0.284	7.93%	1235.2	4.06	0.42	17.02	1.77	1.059889655
Sinkhole 1	Footslope	68	12-58	1.273	0.13	5.00%	992.7	5.81	0.59			
Sinkhole 1	Footslope	69	58-87	1.133	0.123	4.50%	1069.1	3.51	0.38			
Sinkhole 1	Footslope	70	87-118	0.682	0.068	3.43%	1209.2	2.56	0.25			
Sinkhole 1	Footslope	71	118-145	0.305	0.033	2.67%	1379	1.08	0.12			
Sinkhole 1	Footslope	72	145+	0.248	0.038	2.61%		0	0			
Sinkhole 1	Sideslope	89	0-8	3.749	0.371	9.74%	965.3	2.9	0.29	9.77	1.43	0.457684821
Sinkhole 1	Sideslope	90	8-26	0.966	0.108	4.67%	1359	2.36	0.26			
Sinkhole 1	Sideslope	91	26-42	0.506	0.063	4.23%	1189.2	0.96	0.12			
Sinkhole 1	Sideslope	92	26-42	0.321	0.052	4.05%	1537.7	1.33	0.22			
Sinkhole 1	Sideslope	93	69-107	0.245	0.051	3.93%	1189.9	1.11	0.23			
Sinkhole 1	Sideslope	94	107-138	0.184	0.053	3.76%	1301.9	0.71	0.2			
Sinkhole 1	Sideslope	95	138-160	0.1655	0.046	3.57%	1212.2	0.4	0.11			
Sinkhole 1	Sideslope	96	160+	0.135	0.048	5.65%	856.3	0	0			
Sinkhole 1	Shoulder	97	0-18	2.53	0.264	7.64%	1276.7	5.81	0.61	11.67	1.4	0.669481752
Sinkhole 1	Shoulder	98	18-33	1.107	0.117	4.79%	1267.1	2.1	0.22			
Sinkhole 1	Shoulder	99	33-52	0.492	0.053	3.43%	1282.6	1.2	0.13			
Sinkhole 1	Shoulder	100	52-81	0.283	0.045	3.13%	1247.8	1.02	0.16			
Sinkhole 1	Shoulder	101	81-102	0.209	0.041	2.97%	1347.1	0.59	0.12			
Sinkhole 1	Shoulder	102	102-137	0.218	0.037	3.00%	1234.4	0.94	0.16			
Sinkhole 1	Shoulder	103	137+	0.218	0.044	3.29%		0	0			
Sinkhole 1	Summit	104	0-7	3.645	0.348	9.58%	926	2.36	0.23	10.82	1.45	0.514230346
Sinkhole 1	Summit	105	7-18	1.635	0.168	6.20%	1142.5	2.05	0.21			
Sinkhole 1	Summit	106	18-38	0.887	0.081	5.24%	1135.8	2.01	0.18			
Sinkhole 1	Summit	107	38-59	0.544	0.073	5.75%	1120.3	1.22	0.16			
Sinkhole 1	Summit	108	59-118	0.336	0.057	5.88%	1402.4	2.22	0.38			
Sinkhole 1	Summit	109	118-134	0.124	0.035	4.43%	1431	0.28	0.08			
Sinkhole 1	Summit	110	134-159	0.128	0.037	4.90%	1179.6	0.38	0.11			
Sinkhole 1	Summit	111	159-185	0.1	0.034	5.89%	1112.9	0.29	0.1			
Sinkhole 1	Summit	112	185+	0.127	0.048	5.97%		0	0			
Sinkhole 2	Toeslope	73	0-6	5.766	0.542	13.88%	928.3	3.21	0.3	23.32	2.42	1.300013514
Sinkhole 2	Toeslope	74	6-26	1.864	0.208	6.36%	1211.5	4.52	0.5			
Sinkhole 2	Toeslope	75	26-46	0.974	0.094	4.26%	1412.4	2.75	0.27			
Sinkhole 2	Toeslope	76	46-77	0.93	0.1	4.11%	1357.6	3.91	0.42			
Sinkhole 2	Toeslope	77	77-97	0.9665	0.0985	4.31%	1285.7	2.49	0.25			
Sinkhole 2	Toeslope	78	97-109	0.932	0.096	5.17%	1178.9	1.32	0.14			
Sinkhole 2	Toeslope	79	109-129	1.061	0.11	4.34%	1269.4	2.69	0.28			
Sinkhole 2	Toeslope	80	129-148	1.078	0.117	4.23%	1181.9	2.42	0.26			
Sinkhole 2	Toeslope	81	148+	1.202	0.12	4.64%		0	0			
Sinkhole 2	Footslope	82	0-5	5.364	0.504	12.17%	988.4	2.65	0.25	22.83	2.3	1.300086667
Sinkhole 2	Footslope	83	5-19	2.637	0.281	7.20%	1226.3	4.53	0.48			
Sinkhole 2	Footslope	84	19-48	1.193	0.123	4.57%	1339	4.63	0.48			
Sinkhole 2	Footslope	85	48-73	1.345	0.138	4.92%	1138.1	3.83	0.39			
Sinkhole 2	Footslope	86	73-99	1.309	0.133	4.78%	1077.3	3.12	0.32			
Sinkhole 2	Footslope	87	99-150	0.569	0.053	3.12%	1404.3	4.08	0.38			
Sinkhole 2	Footslope	88	150+	0.353	0.044	2.92%		0	0			
Sinkhole 2	Sideslope	113	0-7	3.867	0.381	10.16%	1104	2.99	0.29	17.21	1.78	0.991243902
Sinkhole 2	Sideslope	114	7-25	1.72	0.185	5.90%	1141.8	3.54	0.38			
Sinkhole 2	Sideslope	115	25-36	1.027	0.107	4.66%	1367.2	1.54	0.16			
Sinkhole 2	Sideslope	116	36-55	1.029	0.111	4.82%	1317.5	2.58	0.28			
Sinkhole 2	Sideslope	117	55-74	0.683	0.07	3.93%	1194.5	1.47	0.15			
Sinkhole 2	Sideslope	118	74-94	0.345	0.046	3.72%	1341.3	0.87	0.12			
Sinkhole 2	Sideslope	119	95-123	0.458	0.044	3.02%	1445.8	1.11	0.11			
Sinkhole 2	Summit	120	0-15	3.246	0.329	8.54%	1073.6	5.23	0.53	17.18	1.92	0.957746667
Sinkhole 2	Summit	121	15-29	1.265	0.143	4.97%	1244.9	2.2	0.25			
Sinkhole 2	Summit	122	29-53	1.028	0.097	4.47%	1325	3.27	0.31			
Sinkhole 2	Summit	123	53-83	1.027	0.109	4.47%	1216.7	3.75	0.4			
Sinkhole 2	Summit	124	83-96	0.47	0.058	3.48%	1386.5	0.85	0.1			
Sinkhole 2	Summit	125	96-124	0.295	0.047	4.36%	1326.4	1.04	0.17			
Sinkhole 2	Summit	126	124-150+	0.285	0.054	3.50%	1423.6	0.84	0.16			

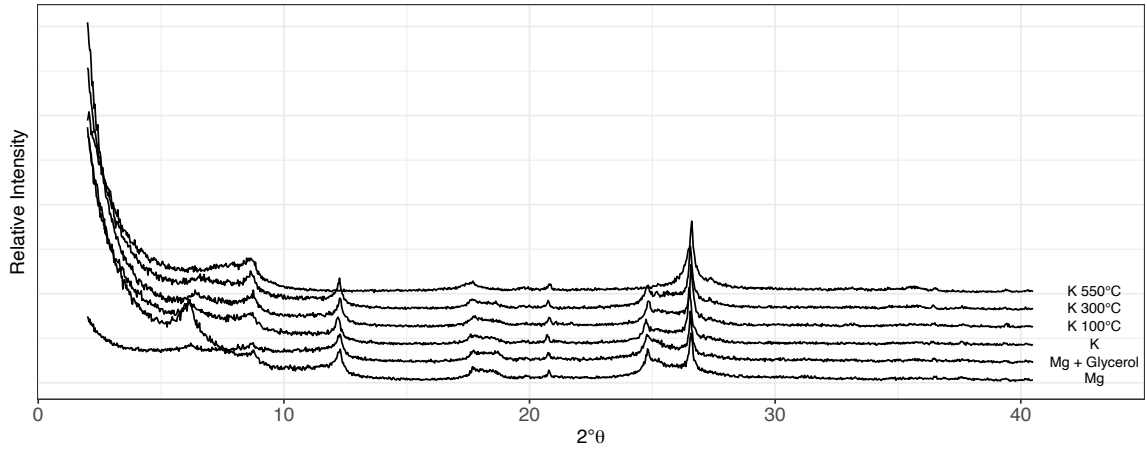
Appendix 1. Select bulk physical property data for all study soils.

Sinkhole	Hillslope Position	Lab ID	Sample Depth (cm)	pH H2O 1:2	EC H2O 1:2	pH CaCl2 1:2	pH KCl 1:2
Sinkhole 1	Toeslope	60	0-8	5.19	101	5.32	4.85
Sinkhole 1	Toeslope	61	8-41	5.07	36	5.27	4.8
Sinkhole 1	Toeslope	62	41-74	4.965	29.25	5.025	4.505
Sinkhole 1	Toeslope	63	74-99	4.95	32.9	5	4.68
Sinkhole 1	Toeslope	64	99-123	5.11	27.2	5.09	4.67
Sinkhole 1	Toeslope	65	123-156	5.49	44.5	5.33	4.42
Sinkhole 1	Toeslope	66	156+	5.36	42.4	5.23	4.47
Sinkhole 1	Footslope	67	0-12	5.28	89.5	5.15	4.79
Sinkhole 1	Footslope	68	12-58	5.02	32	4.98	4.4
Sinkhole 1	Footslope	69	58-87	5.06	34.4	4.98	4.55
Sinkhole 1	Footslope	70	87-118	5.2	25.9	5.1	4.79
Sinkhole 1	Footslope	71	118-145	5.29	23.9	5.14	4.78
Sinkhole 1	Footslope	72	145+	5.38	23.2	5.19	4.82
Sinkhole 1	Sideslope	89	0-8	5.36	368	5.33	5.15
Sinkhole 1	Sideslope	90	8-26	5.395	73.6	5.215	4.89
Sinkhole 1	Sideslope	91	26-42	6.08	41.1	5.61	5.01
Sinkhole 1	Sideslope	92	26-42	6.16	22.5	5.51	4.81
Sinkhole 1	Sideslope	93	69-107	6.06	20	5.44	4.76
Sinkhole 1	Sideslope	94	107-138	6.14	21.3	5.39	4.83
Sinkhole 1	Sideslope	95	138-160	6.03	20.5	5.32	4.76
Sinkhole 1	Sideslope	96	160+	5.55	43.4	5.12	4.54
Sinkhole 1	Shoulder	97	0-18	5.18	192	4.94	4.56
Sinkhole 1	Shoulder	98	18-33	5.36	43.3	4.84	4.41
Sinkhole 1	Shoulder	99	33-52	5.47	24.3	4.83	4.43
Sinkhole 1	Shoulder	100	52-81	5.58	17.1	4.95	4.63
Sinkhole 1	Shoulder	101	81-102	5.72	18.7	5.04	4.79
Sinkhole 1	Shoulder	102	102-137	5.79	20.2	5.15	4.97
Sinkhole 1	Shoulder	103	137+	5.71	27.45	5.235	5.005
Sinkhole 1	Summit	104	0-7	5.91	330	5.51	5.11
Sinkhole 1	Summit	105	7-18	5.88	84.2	5.42	4.91
Sinkhole 1	Summit	106	18-38	5.87	66	5.44	4.95
Sinkhole 1	Summit	107	38-59	6.03	26.8	5.46	5.01
Sinkhole 1	Summit	108	59-118	6.08	29.1	5.55	5.15
Sinkhole 1	Summit	109	118-134	6.01	26.1	5.51	5.12
Sinkhole 1	Summit	110	134-159	5.74	27.9	5.45	5.07
Sinkhole 1	Summit	111	159-185	5.33	39.4	4.68	3.92
Sinkhole 1	Summit	112	185+	4.85	47.7	4.16	3.61
Sinkhole 2	Toeslope	73	0-6	5.83	269	5.87	5.75
Sinkhole 2	Toeslope	74	6-26	5.65	104	5.67	5.43
Sinkhole 2	Toeslope	75	26-46	5.46	55.7	5.55	5.14
Sinkhole 2	Toeslope	76	46-77	5.43	46.6	5.47	5.05
Sinkhole 2	Toeslope	77	77-97	5.415	50.2	5.4	5.075
Sinkhole 2	Toeslope	78	97-109	6.26	92.7	5.39	5.09
Sinkhole 2	Toeslope	79	109-129	6.17	61.3	5.38	5
Sinkhole 2	Toeslope	80	129-148	6.08	67.7	5.33	4.9
Sinkhole 2	Toeslope	81	148+	6.05	64.4	5.28	4.83
Sinkhole 2	Footslope	82	0-5	5.91	310	5.54	5.38
Sinkhole 2	Footslope	83	5-19	5.81	123	5.42	5.08
Sinkhole 2	Footslope	84	19-48	5.99	59.4	5.42	5.03
Sinkhole 2	Footslope	85	48-73	6.03	58.4	5.44	5.15
Sinkhole 2	Footslope	86	73-99	6.05	56.2	5.45	5.2
Sinkhole 2	Footslope	87	99-150	6.13	54.4	5.48	5.25
Sinkhole 2	Footslope	88	150+	6.21	45.7	5.53	5.32
Sinkhole 2	Sideslope	113	0-7	5.35	297	5.26	5.21
Sinkhole 2	Sideslope	114	7-25	5.58	87.1	5.36	5.25
Sinkhole 2	Sideslope	115	25-36	5.74	38.4	5.42	5.33
Sinkhole 2	Sideslope	116	36-55	5.685	31.8	5.375	5.275
Sinkhole 2	Sideslope	117	55-74	6.04	50.6	5.56	5.21
Sinkhole 2	Sideslope	118	74-94	6.16	31.1	5.48	5.05
Sinkhole 2	Sideslope	119	95-123	6.45	41.8	5.73	5.43
Sinkhole 2	Summit	120	0-15	5.69	252	5.5	5.17
Sinkhole 2	Summit	121	15-29	6.03	61.5	5.55	5.21
Sinkhole 2	Summit	122	29-53	6.2	44.4	5.61	5.24
Sinkhole 2	Summit	123	53-83	6.21	37.8	5.6	5.37
Sinkhole 2	Summit	124	83-96	6.15	32.1	5.58	5.3
Sinkhole 2	Summit	125	96-124	6.12	32.2	5.5	5.2
Sinkhole 2	Summit	126	124-150+	6.1	36.4	5.57	5.21

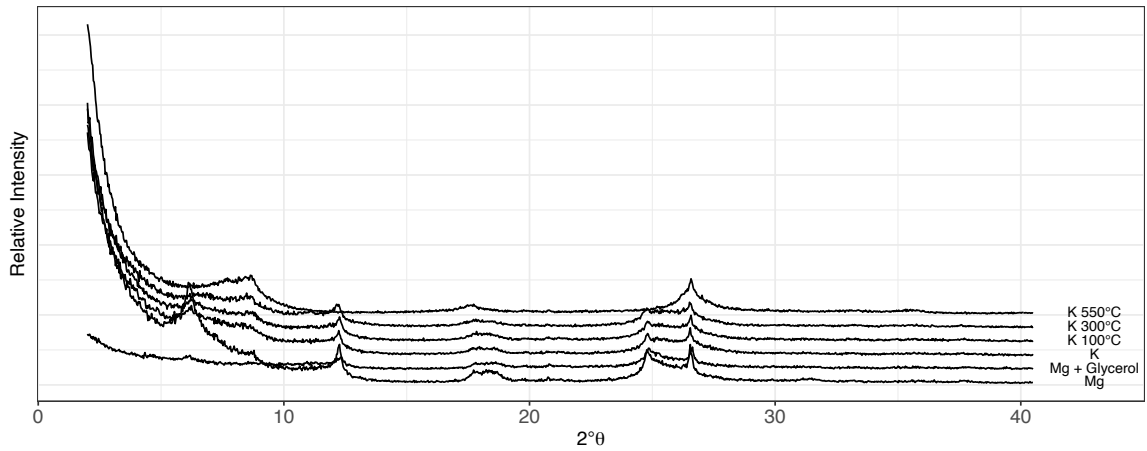
Appendix 2. pH and electrical conductivity data for all study samples.

Sinkhole	Hillslope Position	Lab ID	Sample Depth (cm)	Calculated Loss on Ignition (%)	Gravimetric Water Content
Sinkhole 1	Toeslope	60	0-8	7.40%	0.0315
Sinkhole 1	Toeslope	61	8-41	5.24%	0.0266
Sinkhole 1	Toeslope	62	41-74	4.72%	0.0294
Sinkhole 1	Toeslope	63	74-99	3.90%	0.027
Sinkhole 1	Toeslope	64	99-123	3.91%	0.0336
Sinkhole 1	Toeslope	65	123-156	2.41%	0.0496
Sinkhole 1	Toeslope	66	156+	5.14%	0.07015
Sinkhole 1	Footslope	67	0-12	7.93%	0.0321
Sinkhole 1	Footslope	68	12-58	5.00%	0.0286
Sinkhole 1	Footslope	69	58-87	4.50%	0.0283
Sinkhole 1	Footslope	70	87-118	3.43%	0.0255
Sinkhole 1	Footslope	71	118-145	2.67%	0.0237
Sinkhole 1	Footslope	72	145+	2.61%	0.0241
Sinkhole 1	Sideslope	89	0-8	9.74%	0.0398
Sinkhole 1	Sideslope	90	8-26	4.67%	0.0385
Sinkhole 1	Sideslope	91	26-42	4.23%	0.0447
Sinkhole 1	Sideslope	92	26-42	4.05%	0.0467
Sinkhole 1	Sideslope	93	69-107	3.93%	0.0519
Sinkhole 1	Sideslope	94	107-138	3.76%	0.0457
Sinkhole 1	Sideslope	95	138-160	3.57%	0.0415
Sinkhole 1	Sideslope	96	160+	5.65%	0.0732
Sinkhole 1	Shoulder	97	0-18	7.64%	0.0377
Sinkhole 1	Shoulder	98	18-33	4.79%	0.0349
Sinkhole 1	Shoulder	99	33-52	3.43%	0.0319
Sinkhole 1	Shoulder	100	52-81	3.13%	0.0356
Sinkhole 1	Shoulder	101	81-102	2.97%	0.0379
Sinkhole 1	Shoulder	102	102-137	3.00%	0.0921
Sinkhole 1	Shoulder	103	137+	3.29%	0.0439
Sinkhole 1	Summit	104	0-7	9.58%	0.0455
Sinkhole 1	Summit	105	7-18	6.20%	0.0399
Sinkhole 1	Summit	106	18-38	5.24%	0.0499
Sinkhole 1	Summit	107	38-59	5.75%	0.0677
Sinkhole 1	Summit	108	59-118	5.88%	0.0731
Sinkhole 1	Summit	109	118-134	4.73%	0.06435
Sinkhole 1	Summit	110	134-159	4.90%	0.0732
Sinkhole 1	Summit	111	159-185	5.89%	0.0718
Sinkhole 1	Summit	112	185+	5.97%	0.0789
Sinkhole 2	Toeslope	73	0-6	13.88%	0.0485
Sinkhole 2	Toeslope	74	6-26	6.36%	0.0324
Sinkhole 2	Toeslope	75	26-46	4.27%	0.0233
Sinkhole 2	Toeslope	76	46-77	4.11%	0.022
Sinkhole 2	Toeslope	77	77-97	4.31%	0.0824
Sinkhole 2	Toeslope	78	97-109	5.17%	0.0385
Sinkhole 2	Toeslope	79	109-129	4.34%	0.0284
Sinkhole 2	Toeslope	80	129-148	4.23%	0.0192
Sinkhole 2	Toeslope	81	148+	4.64%	0.0775
Sinkhole 2	Footslope	82	0-5	12.17%	0.0406
Sinkhole 2	Footslope	83	5-19	7.20%	0.0355
Sinkhole 2	Footslope	84	19-48	4.54%	0.0331
Sinkhole 2	Footslope	85	48-73	4.92%	0.0344
Sinkhole 2	Footslope	86	73-99	4.78%	0.0349
Sinkhole 2	Footslope	87	99-150	3.12%	0.0285
Sinkhole 2	Footslope	88	150+	2.92%	0.0284
Sinkhole 2	Sideslope	113	0-7	10.16%	0.0449
Sinkhole 2	Sideslope	114	7-25	5.90%	0.0431
Sinkhole 2	Sideslope	115	25-36	4.66%	0.0392
Sinkhole 2	Sideslope	116	36-55	4.82%	0.0404
Sinkhole 2	Sideslope	117	55-74	3.93%	0.0422
Sinkhole 2	Sideslope	118	74-94	3.72%	0.0483
Sinkhole 2	Sideslope	119	95-123	3.02%	0.0437
Sinkhole 2	Summit	120	0-15	8.54%	0.0469
Sinkhole 2	Summit	121	15-29	4.97%	0.0383
Sinkhole 2	Summit	122	29-53	4.47%	0.0364
Sinkhole 2	Summit	123	53-83	4.47%	0.0403
Sinkhole 2	Summit	124	83-96	3.48%	0.042
Sinkhole 2	Summit	125	96-124	4.36%	0.1132
Sinkhole 2	Summit	126	124-150+	3.50%	0.0473

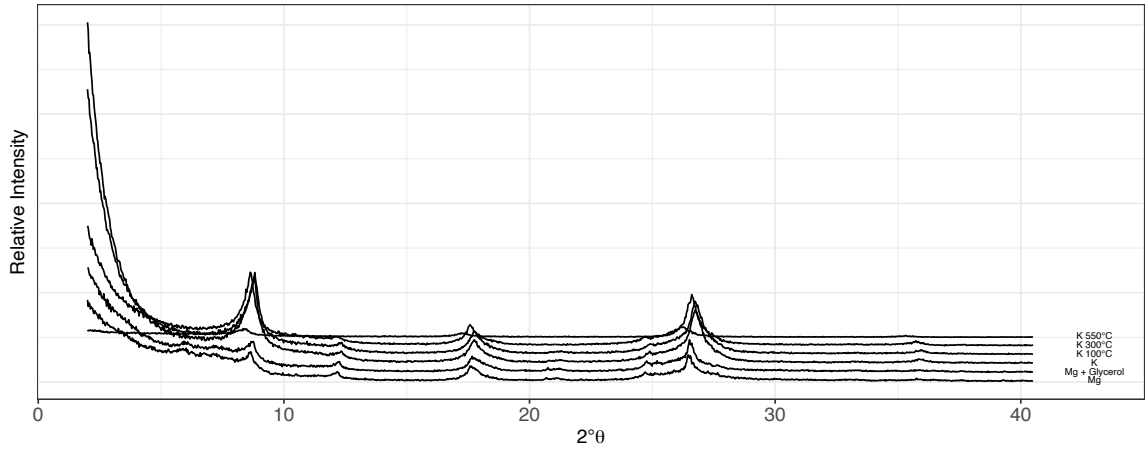
Appendix 3. Loss on ignition and gravimetric water content for study soils.



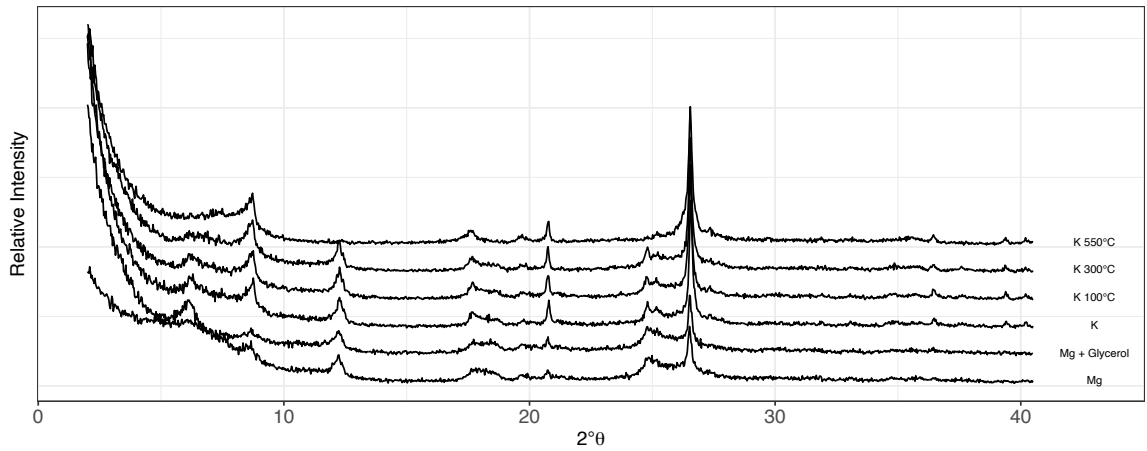
Appendix 4. Diffractogram with all 5 treatments for the clay slide from sinkhole 1, summit pit Ap1 horizon (0-7cm depth).



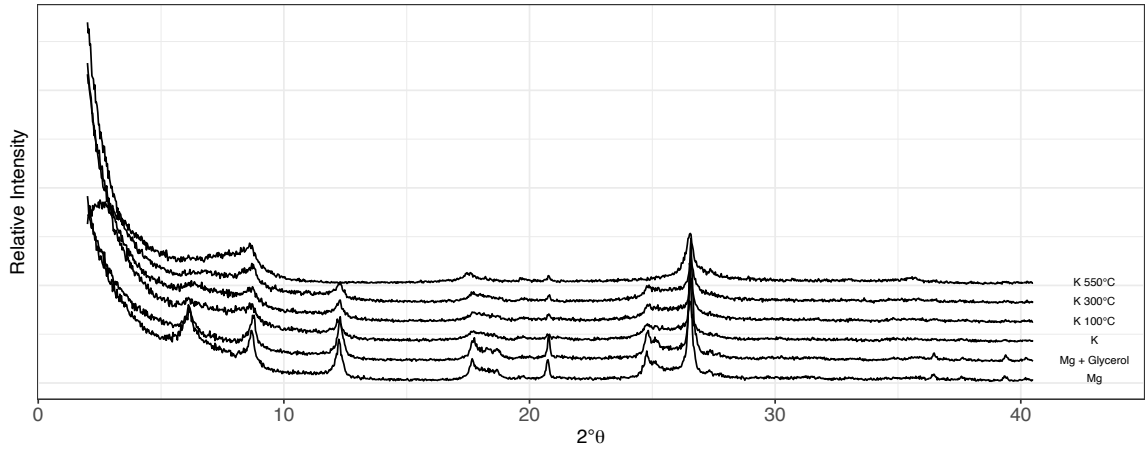
Appendix 5. Diffractogram with all five treatments for the clay slide from sinkhole 1, summit pit 2Bt2 horizon (38-59cm depth).



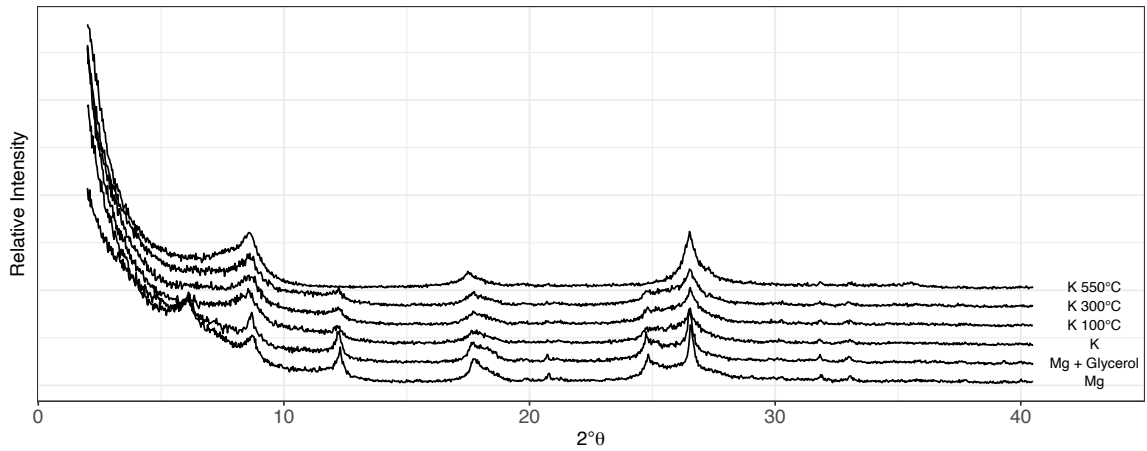
Appendix 6. Diffractogram with all five treatments for the clay slide from sinkhole 1, summit pit 2Btgss horizon (185+cm depth).



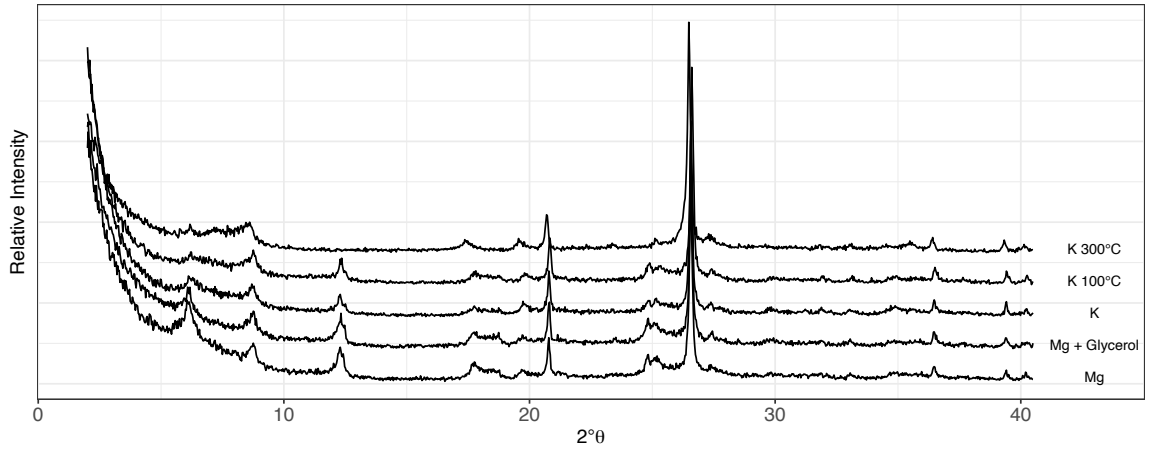
Appendix 7. Diffractogram with all five treatments for the clay slide from sinkhole 1, toeslope pit Ap horizon (0-8cm depth).



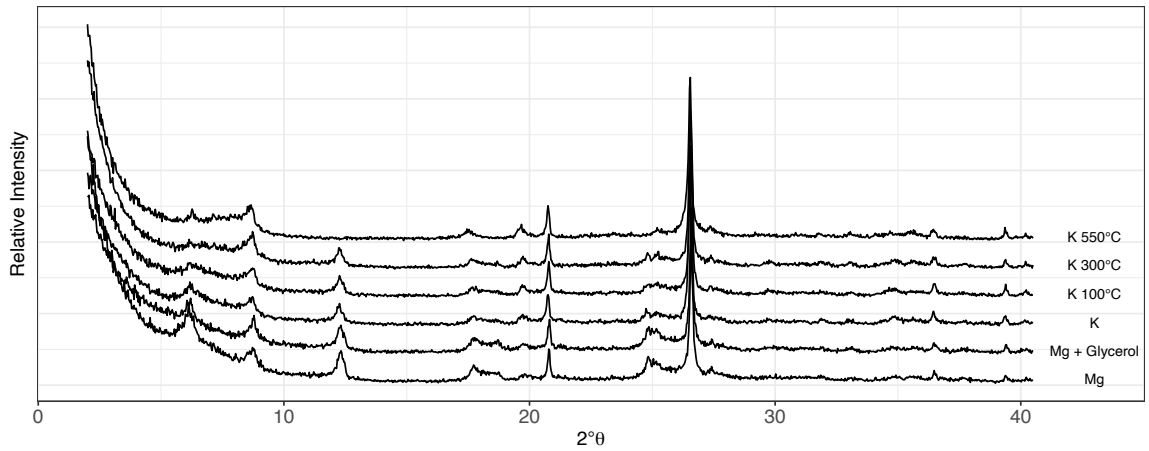
Appendix 8. Diffractogram with all five treatments for the clay slide from sinkhole 1, toeslope pit Bt1 horizon (41-74cm depth).



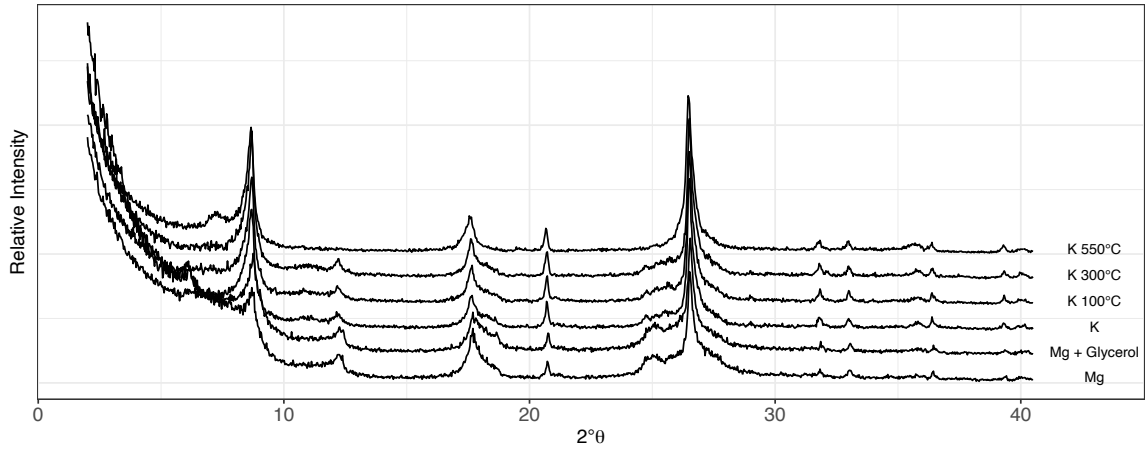
Appendix 9. Diffractogram with all five treatments for the clay slide from sinkhole 1, toeslope pit 2BCt horizon (156+ cm depth).



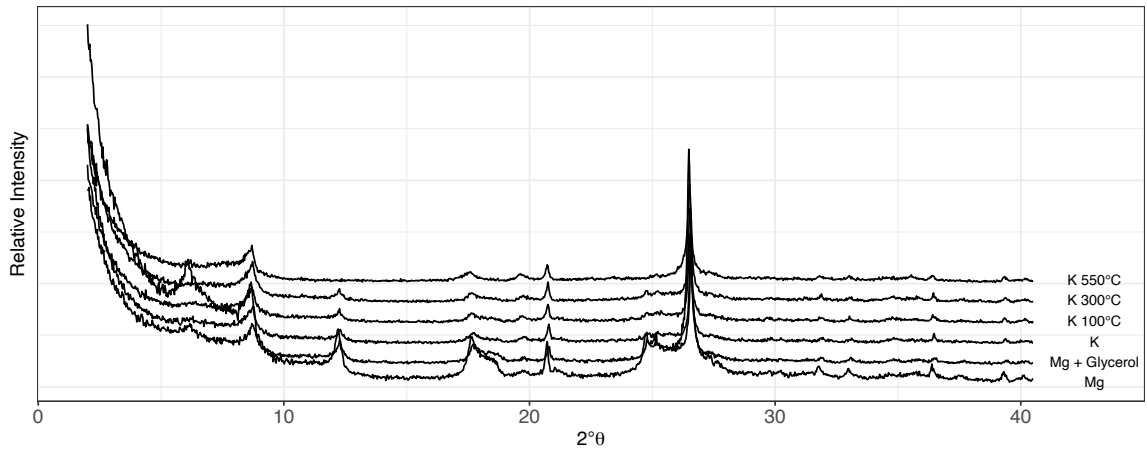
Appendix 10. Diffractogram with all five treatments for the clay slide from sinkhole 2, summit pit Ap horizon (0-15cm depth).



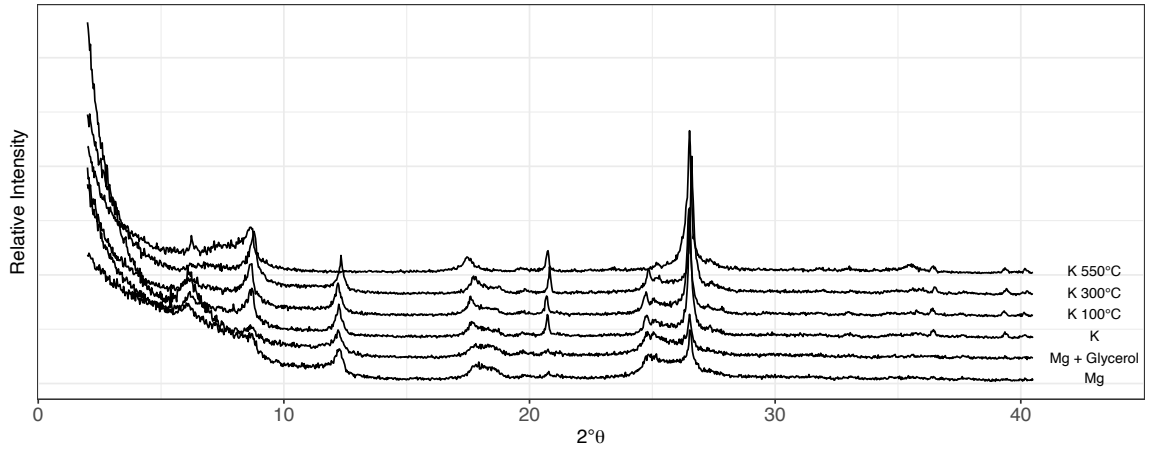
Appendix 11. Diffractogram with all five treatments for the clay slide from sinkhole 2, summit pit Bt2 horizon (29-53cm depth).



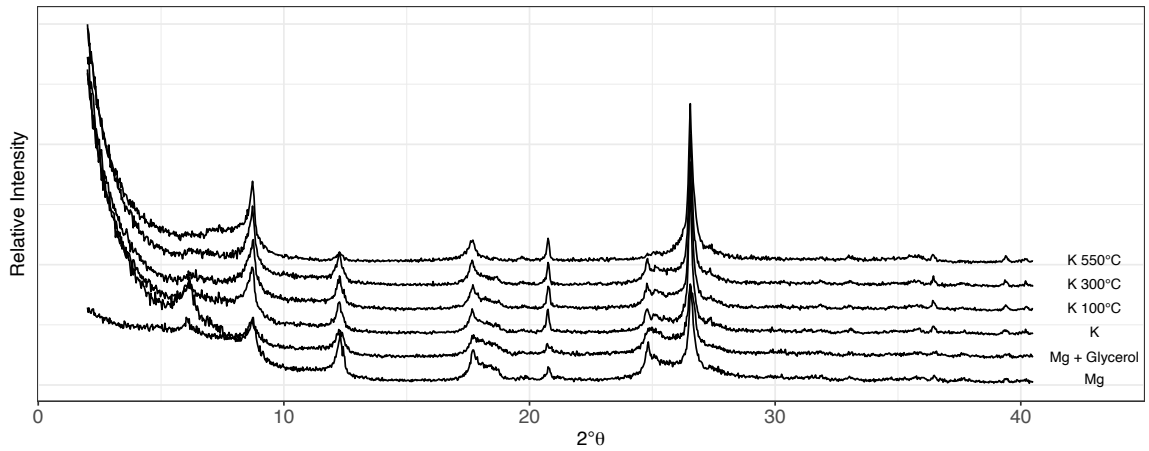
Appendix 12. Diffractogram with all five treatments for the clay slide from sinkhole 2, summit pit 2BCt horizon (124-150cm depth).



Appendix 13. Diffractogram with all five treatments for the clay slide from sinkhole 2, toeslope pit Ap horizon (0-6cm depth).



Appendix 14. Diffractogram with all five treatments for the clay slide from sinkhole 2, toeslope pit Bt3 horizon (46-77cm depth).



Appendix 15. Diffractogram with all five treatments for the clay slide from sinkhole 2, toeslope pit BC4 horizon (148+cm depth).

Sinkhole 1 Summit Ap1 (0-7cm)																							
Mg				Mg + glycerol				K				K + 100°C				K + 300°C				K + 550°C			
Pos. [°2Th.]	d-spacing [Å]	Rel. Int. [%]	Mineral	Pos. [°2Th.]	d-spacing [Å]	Rel. Int. [%]	Mineral	Pos. [°2Th.]	d-spacing [Å]	Rel. Int. [%]	Mineral	Pos. [°2Th.]	d-spacing [Å]	Rel. Int. [%]	Mineral	Pos. [°2Th.]	d-spacing [Å]	Rel. Int. [%]	Mineral	Pos. [°2Th.]	d-spacing [Å]	Rel. Int. [%]	Mineral
6.1991	14.25776	95.48	Vermiculite	6.1770	14.30881	21.59	Vermiculite	6.1478	14.37668	29.91	Vermiculite	6.3604	13.89664	19.42	Vermiculite	8.7070	10.15596	41.45	Mica (dioctahedral)	8.7279	10.13172	35.19	Mica (dioctahedral)
8.7283	10.13118	22.23	Mica (dioctahedral)	8.7128	10.14921	33.49	Mica (dioctahedral)	8.6982	10.16626	29.81	Mica (dioctahedral)	8.7191	10.14194	33.44	Mica (dioctahedral)	12.2356	7.23387	41.93	Kaolinite	17.6843	5.01544	13.78	Mica (dioctahedral)
12.2543	7.22287	61.62	Kaolinite	12.2613	7.21876	68.05	Kaolinite	12.1948	7.25802	45.94	Kaolinite	12.2861	7.20426	41.17	Kaolinite	17.6833	5.01573	18.82	Mica (dioctahedral)	19.7694	4.49091	3.60	Kaolinite
17.7926	4.98516	28.43	Mica (dioctahedral)	17.7245	5.09416	29.17	Mica (dioctahedral)	17.6049	5.03788	19.31	Mica (dioctahedral)	17.7216	5.00496	19.39	Mica (dioctahedral)	19.7859	4.48721	3.91	Kaolinite	20.8058	4.26948	8.22	Quartz
20.7511	4.27572	13.77	Quartz	20.7907	4.27255	14.01	Quartz	19.7448	4.49646	4.63	Kaolinite	19.7660	4.49167	4.36	Kaolinite	20.7417	4.28254	10.47	Quartz	26.5680	3.35513	100.00	Quartz
24.8230	3.58690	69.67	Kaolinite	24.8354	3.58514	67.92	Kaolinite	20.8805	4.25437	6.89	Quartz	20.8264	4.26531	11.92	Quartz	24.7723	3.59413	40.31	Kaolinite				
26.5835	3.35322	100.00	Quartz	26.5485	3.35757	100.00	Quartz	24.7472	3.59772	43.75	Quartz	24.8256	3.58653	45.93	Kaolinite	26.5622	3.35586	100.00	Quartz				
33.1711	2.70081	2.68	Goethite	33.1079	2.70582	2.60	Goethite	26.5268	3.36026	100.00	Quartz	26.5922	3.35215	100.00	Quartz								
36.4613	2.46429	6.13	Goethite					33.1388	2.70337	1.53	Goethite	33.0890	2.70732	3.03	Goethite								
												36.4826	2.46290	5.51	Goethite								

Appendix 16. Mineralogy table for sinkhole 1 Ap1 horizon (0-7cm).

Sinkhole 1 Summit 2B2 (38-59cm)																							
Mg				Mg + glycerol				K				K + 100°C				K + 300°C				K + 550°C			
Pos. [°2Th.]	d-spacing [Å]	Rel. Int. [%]	Mineral	Pos. [°2Th.]	d-spacing [Å]	Rel. Int. [%]	Mineral	Pos. [°2Th.]	d-spacing [Å]	Rel. Int. [%]	Mineral	Pos. [°2Th.]	d-spacing [Å]	Rel. Int. [%]	Mineral	Pos. [°2Th.]	d-spacing [Å]	Rel. Int. [%]	Mineral	Pos. [°2Th.]	d-spacing [Å]	Rel. Int. [%]	Mineral
6.1554	14.35899	100.00	Vermiculite	6.1456	14.38195	22.51	Vermiculite	6.1724	14.31938	69.98	Vermiculite	6.2836	14.06634	50.34	Vermiculite	8.6832	10.18373	54.69	Mica (dioctahedral)	8.6501	10.22268	84.66	Mica (dioctahedral)
8.7056	10.15762	12.00	Mica (dioctahedral)	8.6158	10.26329	8.56	Mica (dioctahedral)	8.2624	10.70142	40.05	Mica (dioctahedral)	8.7527	10.10000	42.02	Mica (dioctahedral)	12.1749	7.26983	70.86	Kaolinite	17.6196	5.03371	22.43	Mica (dioctahedral)
12.2349	7.23430	52.26	Kaolinite	12.3389	7.17358	57.33	Kaolinite	12.2010	7.25433	78.00	Kaolinite	12.2413	7.23054	76.86	Kaolinite	17.7469	4.99790	26.91	Mica (dioctahedral)	20.7999	4.27069	3.64	Quartz
17.7564	4.99524	19.75	Mica (dioctahedral)	17.7890	4.98615	26.41	Mica (dioctahedral)	17.7842	4.98748	30.55	Mica (dioctahedral)	17.7413	4.99946	34.06	Mica (dioctahedral)	20.7987	4.26740	9.04	Quartz	26.5484	3.35758	100.00	Quartz
20.7621	4.27838	4.97	Quartz	19.8182	4.47997	10.17	Kaolinite	21.2540	4.18046	7.89	Goethite	20.7683	4.27712	9.96	Quartz	24.7646	3.59523	81.25	Kaolinite				
24.8145	3.58810	55.82	Kaolinite	20.8197	4.26666	14.07	Quartz	24.7808	3.59291	91.73	Kaolinite	24.8043	3.58956	91.13	Kaolinite	26.5230	3.36073	100.00	Quartz				
26.5461	3.35786	52.04	Quartz	24.8882	3.57765	100.00	Kaolinite	26.5544	3.35683	100.00	Quartz	26.5569	3.35652	100.00	Quartz								
				26.5868	3.35281	65.74	Quartz	33.1288	2.70416	4.67	Goethite	33.1538	2.70218	5.10	Goethite								
				33.2191	2.69702	2.90	Goethite	36.6041	2.45501	5.00	Goethite	36.5673	2.45739	3.96	Goethite								
				36.6290	2.45340	4.43	Goethite																

Appendix 17. Mineralogy table for sinkhole 1 2Bt2 horizon (38-59cm).

Sinkhole 1 Summit 2Btss (185+cm)																							
Mg				Mg + glycerol				K				K + 100°C				K + 300°C				K + 550°C			
Pos. [°2Th.]	d-spacing [Å]	Rel. Int. [%]	Mineral	Pos. [°2Th.]	d-spacing [Å]	Rel. Int. [%]	Mineral	Pos. [°2Th.]	d-spacing [Å]	Rel. Int. [%]	Mineral	Pos. [°2Th.]	d-spacing [Å]	Rel. Int. [%]	Mineral	Pos. [°2Th.]	d-spacing [Å]	Rel. Int. [%]	Mineral	Pos. [°2Th.]	d-spacing [Å]	Rel. Int. [%]	Mineral
5.8677	15.06245	27.68	Vermiculite	6.1309	14.41625	17.05	Vermiculite	8.7540	10.10150	100.00	Mica (dioctahedral)	8.8205	10.02557	100.00	Mica (dioctahedral)	8.6537	10.21840	100.00	Mica (dioctahedral)	8.3809	10.55040	56.47	Mica (dioctahedral)
7.1837	12.30577	30.78	Kaolinite	7.7248	11.44491	23.92	Kaolinite	12.2906	7.20162	7.68	Kaolinite	12.3003	7.19601	7.90	Kaolinite	12.1856	7.26346	5.11	Kaolinite	17.4061	5.09495	33.60	Mica (dioctahedral)
8.6285	10.24819	73.48	Mica (dioctahedral)	8.6968	10.16782	68.82	Mica (dioctahedral)	17.7342	5.00145	32.96	Mica (dioctahedral)	17.7486	4.99741	33.79	Mica (dioctahedral)	17.5831	5.04407	32.26	Mica (dioctahedral)	19.7801	4.48850	0.87	Kaolinite
12.1102	7.30852	23.12	Kaolinite	12.1995	7.25520	23.15	Kaolinite	21.2616	4.17899	2.64	Goethite	21.2650	4.17832	2.23	Goethite	24.6363	3.61366	9.80	Kaolinite	21.5328	4.12696	1.82	smectite
17.6164	5.03462	65.90	Mica (dioctahedral)	17.6578	5.02290	53.02	Mica (dioctahedral)	24.8656	3.58084	10.68	Kaolinite	24.8733	3.57976	9.92	Kaolinite	26.5996	3.35123	78.58	Quartz	26.2296	3.39766	100.00	Quartz
21.1827	4.19437	7.15	Goethite	21.2165	4.18776	9.09	Goethite	26.7274	3.33549	74.66	Quartz	26.7377	3.33422	76.21	Quartz	35.8088	2.50769	4.92	Mica (dioctahedral)	33.5450	2.67156	1.68	biotite (trioctahedral mica)
24.6995	3.60456	25.56	Kaolinite	24.7374	3.59912	27.09	Kaolinite	31.5575	2.83513	0.49	Chlorapatite	33.3126	2.68966	1.17	Goethite					35.3096	2.54199	12.21	Mica (dioctahedral)
26.5220	3.36085	100.00	Quartz	26.5643	3.35560	100.00	Quartz	33.3226	2.68888	1.25	Goethite	35.9892	2.49553	5.46	Goethite								
33.1542	2.70215	3.08	Goethite	31.2887	2.85887	1.39	Chlorapatite	35.9102	2.50084	5.15	hematite												
34.5554	2.59572	1.65	Muscovite	33.2761	2.69253	3.17	Goethite																
35.7627	2.51081	6.29	hematite	34.7858	2.57905	2.31	Mica (dioctahedral)																
36.4720	2.46360	4.33	Goethite	35.8043	2.50799	4.76	hematite																
				36.6118	2.45451	2.51	Goethite																

Appendix 18. Mineralogy table for sinkhole 1 2Btss horizon (185+cm).

Sinkhole 1 Toeslope Ap (0-8cm)																																																																																																																																																																																																																															
Mg				Mg + glycerol				K				K + 100C				K + 300C				K + 550C																																																																																																																																																																																																											
Pos. (#2)h.l	d-spacing [Å]	Rel. Int. [%]	Mineral	Pos. (#2)h.l	d-spacing [Å]	Rel. Int. [%]	Mineral	Pos. (#2)h.l	d-spacing [Å]	Rel. Int. [%]	Mineral	Pos. (#2)h.l	d-spacing [Å]	Rel. Int. [%]	Mineral	Pos. (#2)h.l	d-spacing [Å]	Rel. Int. [%]	Mineral	Pos. (#2)h.l	d-spacing [Å]	Rel. Int. [%]	Mineral																																																																																																																																																																																																								
6.2005	14.25466	67.17	Vermiculite	6.1110	14.46327	19.55	Vermiculite	6.2344	14.20080	18.47	Vermiculite	6.2442	14.15493	14.46	Vermiculite	6.6430	10.23104	33.04	Mica (dioctahedral)	6.6507	10.22188	33.26	Mica (dioctahedral)	7.5726	11.67465	14.28	Kaolinite	8.6392	10.23557	18.53	Mica (dioctahedral)	8.6643	10.20595	25.39	Mica (dioctahedral)	8.6688	10.20097	31.23	Mica (dioctahedral)	12.2399	7.23135	23.14	Kaolinite	12.3530	7.16541	1.80	Kaolinite	12.5889	7.22017	44.29	Mica (dioctahedral)	12.2174	7.24460	38.90	Kaolinite	12.2872	7.20362	25.76	Kaolinite	12.2544	7.22285	23.10	Kaolinite	17.6492	5.02535	12.54	Mica (dioctahedral)	17.6337	5.02972	11.32	Mica (dioctahedral)	17.7530	4.99617	26.42	Mica (dioctahedral)	17.6719	5.01892	22.42	Mica (dioctahedral)	17.7223	5.00477	13.38	Mica (dioctahedral)	17.6945	5.01258	14.51	Mica (dioctahedral)	19.7712	4.49051	3.70	Kaolinite	19.6879	4.50931	5.22	Kaolinite	19.7260	4.50070	9.55	Kaolinite	20.7414	4.28260	21.45	Quartz	20.7725	4.27626	16.72	Quartz	20.7420	4.28247	17.25	Quartz	25.2149	3.52911	16.54	Kaolinite	25.2001	3.53407	5.33	Kaolinite	20.9278	4.24487	8.21	Quartz	24.8212	3.58715	49.91	Kaolinite	24.8470	3.58349	19.05	Kaolinite	25.2149	3.52911	17.31	Kaolinite	26.5518	3.35715	100.00	Quartz	26.5469	3.35776	100.00	Quartz	24.8888	3.57757	48.00	Kaolinite	26.5408	3.58551	100.00	Quartz	26.5795	3.53771	100.00	Quartz	33.1373	2.70349	2.12	Goethite	33.1373	2.70349	2.12	Goethite	33.1373	2.70349	2.12	Goethite	33.1373	2.70349	2.12	Goethite	26.5261	3.36035	100.00	Quartz	33.1502	2.70023	3.22	Goethite	33.1497	2.70092	2.26	Goethite	33.1340	2.70375	1.76	Goethite	36.4623	2.46219	5.10	Goethite	36.4623	2.46219	5.10	Goethite	36.2055	2.48111	3.11	Goethite	33.1042	2.70611	4.55	Goethite	36.5159	2.46074	5.28	Goethite	34.7582	2.58104	3.44	Mica (dioctahedral)	36.5107	2.46107	6.36	Goethite	34.8436	2.57490	5.49	Mica (dioctahedral)	36.5333	2.45960	5.09	Goethite

Appendix 19. Mineralogy table for sinkhole 1 toeslope Ap horizon (0-8cm).

Sinkhole 1 Toeslope Bt1 (41-74cm)																																																																																																																																																																											
Mg				Mg + glycerol				K				K + 100C				K + 300C				K + 550C																																																																																																																																																							
Pos. (#2)h.l	d-spacing [Å]	Rel. Int. [%]	Mineral	Pos. (#2)h.l	d-spacing [Å]	Rel. Int. [%]	Mineral	Pos. (#2)h.l	d-spacing [Å]	Rel. Int. [%]	Mineral	Pos. (#2)h.l	d-spacing [Å]	Rel. Int. [%]	Mineral	Pos. (#2)h.l	d-spacing [Å]	Rel. Int. [%]	Mineral	Pos. (#2)h.l	d-spacing [Å]	Rel. Int. [%]	Mineral																																																																																																																																																				
8.1661	14.47483	42.43	Vermiculite	6.1959	14.26517	20.29	Vermiculite	6.1628	14.34183	26.84	Vermiculite	6.2601	14.11906	21.47	Vermiculite	6.8085	12.98300	21.72	Vermiculite	8.6419	10.23231	63.36	Mica/Vermiculite?	8.8554	10.18118	34.71	Mica (dioctahedral)	8.7170	10.14431	30.90	Mica (dioctahedral)	8.7044	10.15904	51.64	Mica (dioctahedral)	8.7592	10.09557	46.24	Mica (dioctahedral)	12.2440	7.22896	36.47	Kaolinite	12.2955	7.19876	37.00	Kaolinite	12.2422	7.21297	47.83	Kaolinite	12.2713	7.21992	42.39	Kaolinite	17.6895	5.01398	20.54	Mica (dioctahedral)	17.7301	5.00259	21.31	Mica (dioctahedral)	17.7159	5.00657	27.71	Mica (dioctahedral)	17.7454	4.99831	24.04	Mica (dioctahedral)	17.7236	5.00440	23.71	Mica (dioctahedral)	19.7140	4.50340	3.03	Kaolinite	19.7834	4.48776	1.95	Kaolinite	19.6732	4.51264	8.47	Kaolinite	20.7883	4.27304	11.94	Quartz	19.7579	4.49350	6.51	Kaolinite	20.7895	4.27280	9.80	Quartz	20.7586	4.27908	15.62	Quartz	24.8024	3.58983	75.44	Kaolinite	24.8723	3.57990	74.02	Kaolinite	24.8164	3.58784	46.93	Kaolinite	26.5932	3.35202	100.00	Quartz	26.5842	3.35830	38.49	Kaolinite	26.5361	3.35910	100.00	Quartz	26.5879	3.35267	100.00	Quartz	26.5468	3.35802	100.00	Quartz	33.0150	2.71322	1.54	Goethite	33.2665	2.69328	0.81	Goethite	32.9805	2.71598	2.45	Goethite	36.5024	2.46161	5.92	Goethite	33.1608	2.70162	2.99	Goethite	36.2949	2.47521	2.94	Goethite	36.4704	2.46370	5.46	Goethite	36.5283	2.45993	4.56	Goethite	36.4527	2.46485	5.37	Goethite

Appendix 20. Mineralogy table for sinkhole 1 toeslope Bt1 horizon (41-74cm).

Sinkhole 1 Toeslope 2Bc1 (156+cm)																																																																																																																																																																															
Mg				Mg + glycerol				K				K + 100C				K + 300C				K + 550C																																																																																																																																																											
Pos. (#2)h.l	d-spacing [Å]	Rel. Int. [%]	Mineral	Pos. (#2)h.l	d-spacing [Å]	Rel. Int. [%]	Mineral	Pos. (#2)h.l	d-spacing [Å]	Rel. Int. [%]	Mineral	Pos. (#2)h.l	d-spacing [Å]	Rel. Int. [%]	Mineral	Pos. (#2)h.l	d-spacing [Å]	Rel. Int. [%]	Mineral	Pos. (#2)h.l	d-spacing [Å]	Rel. Int. [%]	Mineral																																																																																																																																																								
4.1198	14.44236	51.36	Vermiculite	4.0922	14.50789	33.02	Vermiculite	4.5868	10.30507	89.39	Mica (dioctahedral)	4.1628	14.48259	9.63	Vermiculite	4.6782	10.18957	68.66	Mica (dioctahedral)	8.7113	10.15100	36.72	Mica (dioctahedral)	8.6731	10.19552	48.84	Mica (dioctahedral)	12.2664	7.25115	32.64	Kaolinite	12.2064	7.25115	32.64	Kaolinite	12.2862	7.20422	44.33	Kaolinite	12.2197	7.24325	51.22	Kaolinite	17.7456	4.99825	40.26	Mica (dioctahedral)	12.2023	7.25356	30.26	Kaolinite	17.7344	5.00138	38.82	Mica (dioctahedral)	12.2034	7.25292	23.51	Kaolinite	17.6433	5.02701	34.46	Mica (dioctahedral)	17.7837	4.48848	4.53	Kaolinite	17.7212	5.00509	45.39	Mica (dioctahedral)	17.6982	5.01153	42.79	Mica (dioctahedral)	19.6685	4.51372	3.10	Kaolinite	17.7344	5.00138	38.82	Mica (dioctahedral)	24.7939	3.59875	38.01	Kaolinite	20.7911	4.27247	9.42	Quartz	20.8123	4.26817	6.06	Quartz	24.7474	3.59769	44.24	Kaolinite	19.7192	4.50224	4.52	Kaolinite	26.5955	3.35619	100.00	Quartz	24.8501	3.58305	44.80	Kaolinite	24.8081	3.58903	50.69	Kaolinite	26.5628	3.35578	100.00	Quartz	20.7643	4.27793	6.60	Quartz	33.0607	2.71037	7.96	Goethite	26.5907	3.35183	100.00	Quartz	26.5577	3.35890	100.00	Quartz	22.9926	2.71501	9.11	Goethite	24.7954	3.59083	43.86	Kaolinite	36.5968	2.45548	4.02	Goethite	33.6605	2.70959	8.93	Goethite	32.9786	2.71613	10.74	Goethite	36.4537	2.46479	3.89	Goethite	33.0415	2.71110	9.24	Goethite	36.0613	2.49070	2.19	Goethite	36.2446	2.47853	2.26	Goethite	36.9266	2.43430	1.67	Goethite

Appendix 21. Mineralogy table for sinkhole 1 toeslope 2Bc1 horizon (156+cm).

Sinkhole 2 Summit Ap (0-20cm)																			
Mg				Mg + glycerol				K				K + 100C				K + 300C			
Pos. [°2Th.]	d-spacing [Å]	Rel. Int. [%]	Mineral	Pos. [°2Th.]	d-spacing [Å]	Rel. Int. [%]	Mineral	Pos. [°2Th.]	d-spacing [Å]	Rel. Int. [%]	Mineral	Pos. [°2Th.]	d-spacing [Å]	Rel. Int. [%]	Mineral	Pos. [°2Th.]	d-spacing [Å]	Rel. Int. [%]	Mineral
6.1528	14.36508	24.37	Vermiculite	6.1111	14.46308	16.06	Vermiculite	6.2365	14.17245	10.43	Vermiculite	6.2110	14.23055	8.98	Vermiculite	8.5689	10.31932	12.29	Mica (dioctahedral)
8.7081	10.15465	11.77	Mica (dioctahedral)	8.7109	10.15147	14.27	Mica (dioctahedral)	8.7136	10.14832	12.91	Mica (dioctahedral)	8.7460	10.11070	21.36	Mica (dioctahedral)	17.4395	5.08529	5.52	Mica (dioctahedral)
12.3059	7.19275	19.08	Kaolinite	12.3130	7.18859	17.77	Kaolinite	12.3157	7.18703	10.48	Kaolinite	12.3435	7.17091	19.33	Kaolinite	19.6056	4.52805	5.13	Kaolinite
17.7634	4.99330	11.54	Mica (dioctahedral)	17.7232	5.00453	10.50	Mica (dioctahedral)	17.7011	5.01071	5.17	Mica (dioctahedral)	17.7551	4.99560	11.03	Mica (dioctahedral)	20.6825	4.29466	15.79	Quartz
19.6940	4.50793	5.92	Kaolinite	19.7156	4.50304	6.07	Kaolinite	19.7699	4.49079	7.80	Kaolinite	19.7906	4.48615	8.05	Kaolinite	26.4717	3.36712	100.00	Quartz
20.7649	4.27781	19.90	Quartz	20.7817	4.27438	21.16	Quartz	20.7832	4.27407	20.19	Quartz	20.8121	4.26821	34.22	Quartz				
24.9244	3.57253	13.68	Kaolinite	24.9166	3.57363	14.75	Kaolinite	24.9492	3.56903	6.22	Kaolinite	24.8696	3.58029	17.54	Kaolinite				
26.5647	3.35555	100.00	Quartz	26.5783	3.35387	100.00	Quartz	26.5726	3.35457	100.00	Quartz	26.5939	3.35193	100.00	Quartz				
33.1891	2.69938	2.24	Goethite	32.9939	2.71490	2.40	Goethite	33.0916	2.70712	2.65	Goethite	33.1329	2.70384	4.02	Goethite				
36.5122	2.46097	6.51	Goethite	36.5198	2.46048	7.84	Goethite	36.5200	2.46047	7.14	Goethite	36.5379	2.45930	13.21	Goethite				

Appendix 22. Mineralogy table for sinkhole 2 summit Ap horizon (0-20cm).

Sinkhole 2 Summit Bt2 (29-53cm)																							
Mg				Mg + glycerol				K				K + 100C				K + 300C				K + 550C			
Pos. [°2Th.]	d-spacing [Å]	Rel. Int. [%]	Mineral	Pos. [°2Th.]	d-spacing [Å]	Rel. Int. [%]	Mineral	Pos. [°2Th.]	d-spacing [Å]	Rel. Int. [%]	Mineral	Pos. [°2Th.]	d-spacing [Å]	Rel. Int. [%]	Mineral	Pos. [°2Th.]	d-spacing [Å]	Rel. Int. [%]	Mineral				
6.1226	14.43594	32.70	Vermiculite	6.1572	14.35485	18.11	Vermiculite	6.1686	14.32821	13.61	Vermiculite	6.2615	14.11587	9.01	Vermiculite	8.6565	10.21506	19.25	Mica (dioctahedral)	8.6652	10.20485	21.18	Mica (dioctahedral)
8.7780	10.07403	15.37	Mica (dioctahedral)	8.7316	10.12737	17.39	Mica (dioctahedral)	8.6863	10.18009	13.44	Mica (dioctahedral)	8.6756	10.19266	15.35	Mica (dioctahedral)	12.2719	7.21255	13.53	Kaolinite	17.5167	5.06303	6.61	Mica (dioctahedral)
12.3131	7.18854	25.53	Kaolinite	12.2911	7.20134	22.84	Kaolinite	12.2633	7.21760	13.33	Kaolinite	12.3124	7.18896	13.42	Kaolinite	17.7076	5.00888	6.52	Mica (dioctahedral)	19.6506	4.51779	9.09	Kaolinite
17.7269	5.00349	14.24	Mica (dioctahedral)	17.7413	4.99944	11.74	Mica (dioctahedral)	17.7264	5.00363	7.25	Mica (dioctahedral)	17.6766	5.01760	7.22	Mica (dioctahedral)	19.7394	4.49766	7.26	Kaolinite	20.7295	4.28504	19.48	Quartz
19.8284	4.47767	5.00	Kaolinite	20.7747	4.27581	16.72	Quartz	19.6496	4.51803	6.72	Kaolinite	19.7527	4.49468	8.84	Kaolinite	20.7489	4.28108	17.64	Quartz	25.1988	3.53425	7.25	Kaolinite
20.7764	4.27546	19.03	Quartz	24.9371	3.57074	19.02	Kaolinite	20.7297	4.28144	27.61	Quartz	20.7684	4.27710	20.47	Quartz	25.0577	3.55383	7.48	Kaolinite	26.5134	3.36193	100.00	Quartz
24.9099	3.57459	17.48	Kaolinite	26.5888	3.35256	100.00	Quartz	24.7416	3.59852	10.69	Kaolinite	24.9014	3.57578	9.72	Kaolinite	26.5485	3.35756	100.00	Quartz				
26.5902	3.35239	100.00	Quartz	33.0936	2.70696	3.25	Goethite	26.5275	3.36017	100.00	Quartz	26.5611	3.35599	100.00	Quartz								
33.1771	2.70034	0.99	Goethite	36.4888	2.46250	6.58	Goethite	32.9918	2.71508	3.39	Goethite												
36.5261	2.46007	5.69	Goethite					36.4753	2.46338	8.57	Goethite												

Appendix 23. Mineralogy table for sinkhole 2 summit Bt2 horizon (29-53cm).

Sinkhole 2 Summit 2BCt (124-150cm)																							
Mg				Mg + glycerol				K				K + 100C				K + 300C				K + 550C			
Pos. [°2Th.]	d-spacing [Å]	Rel. Int. [%]	Mineral	Pos. [°2Th.]	d-spacing [Å]	Rel. Int. [%]	Mineral	Pos. [°2Th.]	d-spacing [Å]	Rel. Int. [%]	Mineral	Pos. [°2Th.]	d-spacing [Å]	Rel. Int. [%]	Mineral	Pos. [°2Th.]	d-spacing [Å]	Rel. Int. [%]	Mineral				
6.0913	14.51000	28.45	Vermiculite	6.1428	14.38845	12.32	Vermiculite	8.6493	10.22361	75.72	Mica (dioctahedral)	8.6516	10.22084	74.87	Mica (dioctahedral)	8.6560	10.21568	85.80	Mica (dioctahedral)	8.6318	10.24428	73.81	Mica (dioctahedral)
8.6982	10.16620	52.35	Mica (dioctahedral)	8.7583	10.09653	59.75	Mica (dioctahedral)	12.2168	7.24499	8.19	Kaolinite	12.2170	7.24483	7.79	Kaolinite	12.1805	7.26649	9.06	Kaolinite	17.6003	5.03918	24.39	Mica (dioctahedral)
12.2804	7.20759	17.79	Kaolinite	12.3444	7.17040	14.99	Kaolinite	17.6365	5.02892	24.99	Mica (dioctahedral)	17.6313	5.03041	26.31	Mica (dioctahedral)	17.6243	5.03238	27.26	Mica (dioctahedral)	19.6278	4.52300	0.97	Kaolinite
17.6930	5.01300	45.80	Mica (dioctahedral)	17.6716	5.01900	36.13	Mica (dioctahedral)	20.6955	4.29200	14.49	Quartz	20.6845	4.29424	14.68	Quartz	20.6894	4.29324	14.65	Quartz	20.6630	4.29867	11.01	Quartz
20.7172	4.28754	12.33	Quartz	20.7546	4.27991	12.29	Quartz	24.7269	3.60662	7.35	Kaolinite	26.5494	3.35744	100.00	Quartz	26.5522	3.35710	100.00	Quartz	26.5146	3.36177	100.00	Quartz
24.8447	3.57815	20.40	Kaolinite	25.0989	3.54809	25.06	Kaolinite	26.5455	3.35793	100.00	Quartz	33.0171	2.71305	6.87	Goethite								
26.5558	3.35665	100.00	Quartz	26.5673	3.35523	100.00	Quartz	33.0094	2.71367	5.69	Goethite	36.3933	2.46670	8.56	Goethite								
33.0527	2.71021	7.46	Goethite	33.0378	2.71140	6.57	Goethite																
36.4623	2.46219	8.31	Goethite	36.5133	2.46091	4.46	Goethite																

Appendix 24. Mineralogy table for sinkhole 2 summit 2BCt horizon (124-150cm).

Sinkhole 2 Toeslope Ap (0-6cm)																							
Mg				Mg + glycerol				K				K + 100C				K + 300C				K + 550C			
Pos. [°2Th.]	d-spacing [Å]	Rel. Int. [%]	Mineral	Pos. [°2Th.]	d-spacing [Å]	Rel. Int. [%]	Mineral	Pos. [°2Th.]	d-spacing [Å]	Rel. Int. [%]	Mineral	Pos. [°2Th.]	d-spacing [Å]	Rel. Int. [%]	Mineral	Pos. [°2Th.]	d-spacing [Å]	Rel. Int. [%]	Mineral	Pos. [°2Th.]	d-spacing [Å]	Rel. Int. [%]	Mineral
6.0951	14.30099	24.21	Vermiculite	6.1420	14.39030	12.11	Vermiculite	6.3064	14.01561	5.57	Vermiculite	6.3952	13.82118	7.62	Vermiculite	6.6914	10.17417	41.62	Mica (dioctahedral)	6.6989	10.16536	34.47	Mica (dioctahedral)
8.6072	10.27347	32.07	Mica (dioctahedral)	8.7222	10.13824	30.52	Mica (dioctahedral)	8.8419	10.18527	35.50	Mica (dioctahedral)	8.7069	10.15608	39.81	Mica (dioctahedral)	12.2278	7.23850	10.96	Kaolinite	17.5862	5.04319	11.11	Mica (dioctahedral)
12.2044	7.25231	20.26	Kaolinite	12.2770	7.20960	20.69	Kaolinite	12.2979	7.19737	12.21	Kaolinite	12.2416	7.23034	10.98	Kaolinite	17.6463	5.02614	12.33	Mica (dioctahedral)	19.6149	4.52593	7.89	Kaolinite
17.6580	5.02285	21.67	Mica (dioctahedral)	17.7105	5.00809	23.03	Mica (dioctahedral)	17.7157	5.00662	13.47	Mica (dioctahedral)	17.6358	5.02912	12.37	Mica (dioctahedral)	19.7367	4.49827	6.74	Kaolinite	20.7786	4.27501	8.36	Quartz
19.7783	4.48891	3.20	Kaolinite	19.8062	4.48266	4.28	Kaolinite	19.7947	4.48524	7.18	Kaolinite	19.7217	4.50166	7.00	Kaolinite	20.7378	4.28334	11.09	Quartz	25.1035	3.54745	3.87	Kaolinite
20.6883	4.29347	13.56	Quartz	20.7796	4.27482	14.04	Quartz	20.7890	4.27291	15.79	Quartz	20.8466	4.26122	9.24	Quartz	24.7196	3.60166	9.41	Kaolinite	26.4980	3.36384	100.00	Quartz
24.7885	3.59181	20.16	Kaolinite	24.8558	3.58224	23.05	Kaolinite	25.0881	3.54959	8.41	Kaolinite	24.7992	3.59028	9.71	Kaolinite	26.5418	3.35839	100.00	Quartz				
26.5032	3.36320	100.00	Quartz	26.5870	3.35278	100.00	Quartz	26.5734	3.35446	100.00	Quartz	33.1972	2.69874	1.96	Goethite	33.0589	2.70972	3.85	Goethite				
				33.0603	2.70961	4.54	Goethite	33.1972	2.69874	1.96	Goethite	36.4923	2.46227	7.02	Goethite	36.4796	2.46310	7.50	Goethite				
				36.5266	2.46004	5.10	Goethite																

Appendix 25. Mineralogy table for sinkhole 2 toeslope Ap horizon (0-6cm).

Sinkhole 2 Toeslope Bt3 (46-77cm)																							
Mg				Mg + glycerol				K				K + 100C				K + 300C				K + 550C			
Pos. [°2Th.]	d-spacing [Å]	Rel. Int. [%]	Mineral	Pos. [°2Th.]	d-spacing [Å]	Rel. Int. [%]	Mineral	Pos. [°2Th.]	d-spacing [Å]	Rel. Int. [%]	Mineral	Pos. [°2Th.]	d-spacing [Å]	Rel. Int. [%]	Mineral	Pos. [°2Th.]	d-spacing [Å]	Rel. Int. [%]	Mineral	Pos. [°2Th.]	d-spacing [Å]	Rel. Int. [%]	Mineral
6.1125	14.45967	100.00	Vermiculite	6.0734	14.55257	40.30	Vermiculite	6.2029	14.24911	17.96	Vermiculite	6.1851	14.29006	14.07	Vermiculite	8.7501	10.10606	46.43	Mica (dioctahedral)	8.6577	10.21371	35.02	Mica (dioctahedral)
8.6480	10.22508	32.07	Mica (dioctahedral)	8.7032	10.16041	32.26	Mica (dioctahedral)	8.6369	10.23826	33.29	Mica (dioctahedral)	8.6049	10.27621	42.55	Mica (dioctahedral)??	12.3243	7.18201	25.95	Kaolinite	17.4475	5.08298	13.25	Mica (dioctahedral)
12.2506	7.22509	57.06	Kaolinite	12.2378	7.23259	60.99	Kaolinite	12.2445	7.22865	25.41	Kaolinite	12.2097	7.24918	28.77	Kaolinite	17.7359	5.00097	16.62	Mica (dioctahedral)	19.5800	4.53391	2.17	Kaolinite
17.7762	4.98972	34.02	Mica (dioctahedral)	17.7347	5.00130	34.15	Mica (dioctahedral)	17.6595	5.02244	15.72	Mica (dioctahedral)	17.6179	5.03420	18.67	Mica (dioctahedral)??	19.8373	4.47570	3.01	Kaolinite	20.7385	4.28320	8.02	Quartz
19.8733	4.46767	7.53	Kaolinite	19.6981	4.50700	12.53	Kaolinite	19.7864	4.48710	4.03	Kaolinite	19.7281	4.50022	2.50	Kaolinite	20.8024	4.27019	14.30	Quartz	26.4820	3.36584	100.00	Quartz
20.7632	4.27816	11.86	Quartz	20.7158	4.28783	15.35	Quartz	20.8407	4.26243	9.45	Quartz	20.6811	4.24945	15.10	Quartz	24.8601	3.58162	18.55	Kaolinite				
24.8707	3.58013	53.82	Kaolinite	24.8446	3.58382	67.09	Kaolinite	24.7894	3.59168	21.26	Kaolinite	24.7569	3.59633	19.70	Kaolinite	26.6295	3.34753	100.00	Quartz				
26.5539	3.35689	93.64	Quartz	26.5109	3.36224	100.00	Quartz	26.5356	3.35916	100.00	Quartz	26.4974	3.36392	100.00	Quartz								
33.1162	2.70516	4.32	Goethite	33.0563	2.70993	4.16	Goethite	32.9950	2.71482	3.10	Goethite												
				36.3430	2.47204	4.50	Goethite	36.1793	2.48285	2.75	Goethite												

Appendix 26. Mineralogy table for sinkhole 2 toeslope Bt3 horizon (46-77cm).

Sinkhole 2 Toeslope BC4 (148+cm)																							
Mg				Mg + glycerol				K				K + 100C				K + 300C				K + 550C			
Pos. [°2Th.]	d-spacing [Å]	Rel. Int. [%]	Mineral	Pos. [°2Th.]	d-spacing [Å]	Rel. Int. [%]	Mineral	Pos. [°2Th.]	d-spacing [Å]	Rel. Int. [%]	Mineral	Pos. [°2Th.]	d-spacing [Å]	Rel. Int. [%]	Mineral	Pos. [°2Th.]	d-spacing [Å]	Rel. Int. [%]	Mineral	Pos. [°2Th.]	d-spacing [Å]	Rel. Int. [%]	Mineral
6.1419	14.39044	51.24	Vermiculite	6.0757	14.54723	21.65	Vermiculite	6.1629	14.34157	15.49	Vermiculite	6.2101	14.23272	6.40	Vermiculite	8.6827	10.18437	47.27	Mica (dioctahedral)	8.6871	10.17917	51.13	Mica (dioctahedral)
8.7088	10.15386	41.56	Mica (dioctahedral)	8.6795	10.18812	35.21	Mica (dioctahedral)	8.6638	10.20648	41.01	Mica (dioctahedral)	8.6837	10.18315	44.87	Mica (dioctahedral)	12.2648	7.21672	20.08	Kaolinite	12.2757	7.21037	5.46	Kaolinite
12.3078	7.19160	47.11	Kaolinite	12.2861	7.20425	34.00	Kaolinite	12.2672	7.21534	21.98	Kaolinite	12.2767	7.20977	21.64	Kaolinite	17.6707	5.01926	18.35	Mica (dioctahedral)	17.6405	5.02780	15.24	Mica (dioctahedral)
17.7274	5.00335	37.59	Mica (dioctahedral)	17.7436	4.99882	30.40	Mica (dioctahedral)	17.6832	5.01576	18.95	Mica (dioctahedral)	17.6732	5.01856	20.19	Mica (dioctahedral)	20.7235	4.28626	12.03	Quartz	19.7318	4.49938	1.83	Kaolinite
19.8469	4.47356	3.37	Kaolinite	20.7807	4.27459	13.06	Quartz	19.7543	4.49431	2.03	Kaolinite	19.8046	4.48301	1.72	Kaolinite	24.8024	3.58983	17.29	Kaolinite	20.7417	4.28254	11.74	Quartz
20.7498	4.28088	12.32	Quartz	24.8270	3.58633	35.72	Kaolinite	20.7227	4.28643	14.68	Quartz	20.7631	4.27817	14.45	Quartz	26.5685	3.35507	100.00	Quartz	25.0301	3.55769	4.23	Kaolinite
24.8614	3.58145	38.47	Kaolinite	26.5921	3.35216	100.00	Quartz	24.8420	3.58420	18.43	Kaolinite	24.8048	3.59499	18.55	Kaolinite					26.5765	3.35409	100.00	Quartz
26.5855	3.35297	100.00	Quartz	33.0947	2.70687	3.22	Goethite	26.5329	3.35701	100.00	Quartz	26.5770	3.35403	100.00	Quartz								
33.0546	2.71006	3.29	Goethite	36.5276	2.45997	5.81	Goethite	33.0442	2.71089	2.78	Goethite	33.0306	2.71198	2.51	Goethite								
36.6003	2.45322	5.63	Goethite					36.4623	2.46219	5.66	Goethite	36.3933	2.46670	5.18	Goethite								

Appendix 27. Mineralogy table for sinkhole 2 toeslope BC4 horizon (148+cm).

REFERENCES

- Alves, M., P. Galvão, and P. Aranha. 2021. Karst hydrogeological controls and anthropic effects in an urban lake. *J. Hydrol.* 593(December 2020). doi: 10.1016/j.jhydrol.2020.125830.
- Applegarth, M.T., and D.E. Dahms. 2001. Soil catenas of calcareous tills, Whiskey Basin, Wyoming, USA. *Catena* 42(1): 17–38. doi: 10.1016/S0341-8162(00)00116-8.
- Badía, D., C. Martí, J.M. Aznar, and J. León. 2013. Influence of slope and parent rock on soil genesis and classification in semiarid mountainous environments. *Geoderma* 193–194: 13–21. doi: 10.1016/j.geoderma.2012.10.020.
- Banker, L., P. Reeder, and R. Brinkmann. 1995. A Toposequence of Soils in the Karst of West-Central Florida, U.S.A. *J. Speleol. Soc. Korea* 42(2): 41–63.
- Bautista, F., G. Palacio-Aponte, P. Quintana, and J.A. Zinck. 2011. Spatial distribution and development of soils in tropical karst areas from the Peninsula of Yucatan, Mexico. *Geomorphology* 135(3–4): 308–321. doi: 10.1016/j.geomorph.2011.02.014.
- Berhe, A.A., R.T. Barnes, J. Six, and E. Marín-Spiotta. 2018. Role of Soil Erosion in Biogeochemical Cycling of Essential Elements: Carbon, Nitrogen, and Phosphorus. *Annu. Rev. Earth Planet. Sci.* 46: 521–548. doi: 10.1146/annurev-earth-082517-010018.
- Berhe, A.A., J. Harte, J.W. Harden, and M.S. Torn. 2007. The significance of the erosion-induced terrestrial carbon sink. *Bioscience* 57(4): 337–346. doi: 10.1641/B570408.
- Birkeland, P.W. 1999. *Soils and Geomorphology*. 3rd ed. Oxford University Press, New York.
- Blair, R.J., E.D. Carigan, J.C. Currens, P.W. O'dell, J.A. Ray, et al. 2012. Pilot study to integrate existing karst flow data for Kentucky, USA into the National Hydrography Dataset of US Geological Survey. *Carbonates and Evaporites* 27(2): 123–131. doi: 10.1007/s13146-012-0094-5.
- Boero, V., and U. Schwertmann. 1987. Occurrence and Transformations of Iron and Manganese in a Colluvial Terra Rossa Toposequence of Northern Italy. *Catena* 14: 519–531.
- Bonacci, O. 1987. Principles of Karst Groundwater Circulation. *Karst Hydrology*. Springer, Berlin, Heidelberg. p. 18–48
- Bonneau, J., T.D. Fletcher, J.F. Costelloe, and M.J. Burns. 2017. Stormwater infiltration and the ‘urban karst’ – A review. *J. Hydrol.* 552: 141–150. doi: 10.1016/j.jhydrol.2017.06.043.

- Borden, R.W., I.C. Baillie, and S.H. Hallett. 2020. The East African contribution to the formalisation of the soil catena concept. *Catena* 185(September 2019): 104291. doi: 10.1016/j.catena.2019.104291.
- Bosák, P. 2008. Karst processes and time Procesy krasowe a czas. *Geologos* 14(1): 19–36.
- Bremner, J.M., and A.P. Edwards. 1965. Determination and Isotope-Ratio Analysis of Different Forms of Nitrogen in Soils: I. Apparatus and Procedure for Distillation and Determination of Ammonium¹. *Soil Sci. Soc. Am. J.* 29(5): 504. doi: 10.2136/sssaj1965.03615995002900050011x.
- Brevik, E.C., and J.A. Homburg. 2004. A 5000 year record of carbon sequestration from a coastal lagoon and wetland complex, southern California, USA. *Catena* 57(3): 221–232. doi: 10.1016/j.catena.2003.12.001.
- Buckerfield, S.J., R.S. Quilliam, L. Bussiere, S. Waldron, L.A. Naylor, et al. 2020. Chronic urban hotspots and agricultural drainage drive microbial pollution of karst water resources in rural developing regions. *Sci. Total Environ.* 744: 1–10. doi: 10.1016/j.scitotenv.2020.140898.
- Cabadas-Báez, H., E. Solleiro-Rebolledo, S. Sedov, T. Pi-Puig, and J. Gama-Castro. 2010. Pedosediments of karstic sinkholes in the eolianites of NE Yucatán: A record of Late Quaternary soil development, geomorphic processes and landscape stability. *Geomorphology* 122(3–4): 323–337. doi: 10.1016/j.geomorph.2010.03.002.
- Cahalan, M.D., and A.M. Milewski. 2018. Sinkhole formation mechanisms and geostatistical-based prediction analysis in a mantled karst terrain. *Catena* 165(February 2017): 333–344. doi: 10.1016/j.catena.2018.02.010.
- Calmels, D., J. Gaillardet, A. Brenot, and C. France-Lanord. 2007. Sustained sulfide oxidation by physical erosion processes in the Mackenzie River basin: Climatic perspectives. *Geology* 35(11): 1003–1006. doi: 10.1130/G24132A.1.
- Catani, F., S. Segoni, and G. Falorni. 2010. An empirical geomorphology-based approach to the spatial prediction of soil thickness at catchment scale. *Water Resour. Res.* 46(5): 1–15. doi: 10.1029/2008WR007450.
- Chaney, A.L., and E.P.P. Marbach. 1962. Modified reagents for determination of urea and ammonia. *Clin. Chem.* 8(2): 130–132. doi: 10.1093/clinchem/8.2.130.
- Chaopricha, N.T., and E. Marín-Spiotta. 2014. Soil burial contributes to deep soil organic carbon storage. *Soil Biol. Biochem.* 69: 251–264. doi: 10.1016/j.soilbio.2013.11.011.
- Chen, X., Z. Zhang, C. Soulsby, Q. Cheng, A. Binley, et al. 2018. Characterizing the heterogeneity of karst critical zone and its hydrological function: An integrated approach. *Hydrol. Process.* 32(19): 2932–2946. doi: 10.1002/hyp.13232.
- Chen, H., W. Zhang, K. Wang, and Y. Hou. 2012. Soil organic carbon and total nitrogen as affected by land use types in karst and non-karst areas of northwest Guangxi, China. *J. Sci. Food Agric.* 92(5): 1086–1093. doi: 10.1002/jsfa.4591.

- Chirinda, N., S.D. Roncossek, G. Heckrath, L. Elsgaard, I.K. Thomsen, et al. 2014. Root and soil carbon distribution at shoulderslope and footslope positions of temperate toposequences cropped to winter wheat. *Catena* 123: 99–105. doi: 10.1016/j.catena.2014.07.012.
- Conforti, M., T. Longobucco, F. Scarciglia, G. Niceforo, G. Matteucci, et al. 2020. Interplay between soil formation and geomorphic processes along a soil catena in a Mediterranean mountain landscape: an integrated pedological and geophysical approach. *Environ. Earth Sci.* 79(2): 1–16. doi: 10.1007/s12665-019-8802-2.
- Currens, J.C. 2012. Cover-collapse sinkholes in Kentucky, USA: Geographic and temporal distribution. *Carbonates and Evaporites* 27(2): 137–142. doi: 10.1007/s13146-012-0097-2.
- D.L., J., and W.-S. D. 1987. Evolution model of pedogenesis.pdf. *Soil Sci.* 143(5): 349–366.
- Delle Rose, M., A. Federico, and M. Parise. 2004. Sinkhole genesis and evolution in Apulia, and their interrelations with the anthropogenic environment. *Nat. Hazards Earth Syst. Sci.* 4(5/6): 747–755. doi: 10.5194/nhess-4-747-2004.
- Dethier, D.P., P.W. Birkeland, and J.A. McCarthy. 2012. Using the accumulation of CBD-extractable iron and clay content to estimate soil age on stable surfaces and nearby slopes, Front Range, Colorado. *Geomorphology* 173–174: 17–29. doi: 10.1016/j.geomorph.2012.05.022.
- Dong, X., M.J. Cohen, J.B. Martin, D.L. McLaughlin, A.B. Murray, et al. 2019. Ecohydrologic processes and soil thickness feedbacks control limestone-weathering rates in a karst landscape. *Chem. Geol.* 527(February): 118774. doi: 10.1016/j.chemgeo.2018.05.021.
- Dreybrodt, W. 1988. *Processes in Karst Systems*. Springer-Verlag Berlin Heidelberg.
- Du, W., J. Yu, and S. Yu. 2013. Uncertainty evaluations on the measurement of “carbon” in the research on karst carbon sink effect -A case for dissolved inorganic carbon. *Appl. Mech. Mater.* 303–306: 703–713. doi: 10.4028/www.scientific.net/AMM.303-306.703.
- Egli, M., C. Merkli, G. Sartori, A. Mirabella, and M. Plötze. 2008. Weathering, mineralogical evolution and soil organic matter along a Holocene soil toposequence developed on carbonate-rich materials. *Geomorphology* 97(3–4): 675–696. doi: 10.1016/j.geomorph.2007.09.011.
- ESRI. 2018. ArcMap 10.6. <https://www.esri.com/en-us/arcgis/>.
- Fey, M. V., and J. le Roux. 1976. Electric Charges on Sesquioxidic Soil Clays. *Soil Sci. Soc. Am. J.* 40(3): 359–364. doi: 10.2136/sssaj1976.03615995004000030017x.
- Ford, D.C., and P.W. Williams. 2007. *Karst Hydrogeology and Geomorphology*. John Wiley & Sons.
- Fragoso-Servón, P., A.P. Corona, F.B. Zúñiga, B.P. Hernández, and N.A. Reyes. 2020.

- Soils in extreme conditions : the case of the catenas karst-marsh-coastline in the Mexican Caribbean. *Boletín la Soc. Geológica Mex.* 72(2): 1–18. doi: <http://dx.doi.org/10.18268/BSGM2020v72n2a040619>.
- Franzmeier, D.P., E.J. Pedersen, T.J. Longwell, J.G. Byrne, and C.K. Losche. 1969. Properties of Some Soils in the Cumberland Plateau As Related To Slope Aspect and Position. *Soil Sci Soc Amer PROC* 33(5): 755–761. doi: 10.2136/sssaj1969.03615995003300050037x.
- Frumkin, A., Y. Zaidner, I. Na'aman, A. Tsatskin, N. Porat, et al. 2015. Sagging and collapse sinkholes over hypogenic hydrothermal karst in a carbonate terrain. *Geomorphology* 229: 45–57. doi: 10.1016/j.geomorph.2014.08.001.
- Gaillardet, J., D. Calmels, G. Romero-Mujalli, E. Zakharova, and J. Hartmann. 2019. Global climate control on carbonate weathering intensity. *Chem. Geol.* 527(November 2017): 1–11. doi: 10.1016/j.chemgeo.2018.05.009.
- Galvão, P., R. Hirata, T. Halihan, and R. Terada. 2017. Recharge sources and hydrochemical evolution of an urban karst aquifer, Sete Lagoas, MG, Brazil. *Environ. Earth Sci.* 76(4). doi: 10.1007/s12665-017-6482-3.
- Gonnea, M.E., M.A. Charette, Q. Liu, J.A. Herrera-Silveira, and S.M. Morales-Ojeda. 2014. Trace element geochemistry of groundwater in a karst subterranean estuary (Yucatan Peninsula, Mexico). *Geochim. Cosmochim. Acta* 132: 31–49. doi: 10.1016/j.gca.2014.01.037.
- Grimmeisen, F., M. Zemann, N. Goeppert, and N. Goldscheider. 2016. Weekly variations of discharge and groundwater quality caused by intermittent water supply in an urbanized karst catchment. *J. Hydrol.* 537: 157–170. doi: 10.1016/j.jhydrol.2016.03.045.
- Guggenberger, G., and K. Kaiser. 2003. Dissolved organic matter in soil: Challenging the paradigm of sorptive preservation. *Geoderma* 113(3–4): 293–310. doi: 10.1016/S0016-7061(02)00366-X.
- Hajirasouli, M., S. Mahmoodi, and H. Torabi. 2010. Distribution of clay minerals along a soil toposequence. *J. Food, Agric. Environ.* 8(3-4 PART 2): 1162–1167.
- Hancock, G.R., D. Murphy, and K.G. Evans. 2010. Hillslope and catchment scale soil organic carbon concentration: An assessment of the role of geomorphology and soil erosion in an undisturbed environment. *Geoderma* 155(1–2): 36–45. doi: 10.1016/j.geoderma.2009.11.021.
- Hancock, G.R., T. Wells, C. Dever, and M. Braggins. 2019. Hillslope and point based soil erosion – an evaluation of a Landscape Evolution Model. *Earth Surf. Process. Landforms* 44(5): 1163–1177. doi: 10.1002/esp.4566.
- Hartmann, J., and N. Moosdorf. 2012. The new global lithological map database GLiM: A representation of rock properties at the Earth surface. *Geochemistry, Geophys. Geosystems* 13(12): 1–37. doi: 10.1029/2012GC004370.
- Helfrich, M., H. Flessa, R. Mikutta, A. Dreves, and B. Ludwig. 2007. Comparison of

- chemical fractionation methods for isolating stable soil organic carbon pools. *Eur. J. Soil Sci.* 58(6): 1316–1329. doi: 10.1111/j.1365-2389.2007.00926.x.
- Hillel, D. 2003. *Introduction to Environmental Soil Physics*.
- Hodges, S.C., and L.W. Zelazny. 1980. Determination of Noncrystalline Soil Components By Weight Difference After Selective Dissolution. *Clays Clay Miner.* 28(1): 35–42. doi: 10.1346/CCMN.1980.0280105.
- Hofierka, J., M. Gallay, P. Bandura, and J. Šašak. 2018. Identification of karst sinkholes in a forested karst landscape using airborne laser scanning data and water flow analysis. *Geomorphology* 308: 265–277. doi: 10.1016/j.geomorph.2018.02.004.
- Huggett, R.J. 1975. Soil landscape systems: A model of soil Genesis. *Geoderma* 13(1): 1–22. doi: 10.1016/0016-7061(75)90035-X.
- Hunckler, R. V., and R.J. Schaetzl. 1997. Spodosol Development as Affected by Geomorphic Aspect, Baraga County, Michigan. *Soil Sci. Soc. Am. J.* 61(4): 1105–1115. doi: 10.2136/sssaj1997.03615995006100040017x.
- Ibrahim, M.A., and R. Lal. 2014. Soil carbon and silicon pools across an un-drained toposequence in central Ohio. *Catena* 120: 57–63. doi: 10.1016/j.catena.2014.04.006.
- Jakucs, L. 1977. *Morphogenetics of Karst Regions: Variants of Karst Evolution*. Wiley, New York.
- Jeannin, P.Y., M. Hessenauer, A. Malard, and V. Chapuis. 2016. Impact of global change on karst groundwater mineralization in the Jura Mountains. *Sci. Total Environ.* 541: 1208–1221. doi: 10.1016/j.scitotenv.2015.10.008.
- Jennings, J.N. 1985. *Karst Geomorphology*. 2nd ed. B. Blackwell, New York.
- Jenny, H. 1941. *Factors of Soil Formation: A System of Quantitative Pedology*. McGraw-Hill.
- Jenny, H. 1961. Derivation of State Factor Equations of Soils and Ecosystems. *Soil Sci. Soc. Am. J.* 25(5): 385–388. doi: 10.2136/sssaj1961.03615995002500050023x.
- John, B., T. Yamashita, B. Ludwig, and H. Flessa. 2005. Storage of organic carbon in aggregate and density fractions of silty soils under different types of land use. *Geoderma* 128(1–2): 63–79. doi: 10.1016/j.geoderma.2004.12.013.
- Kaiser, K., and G. Guggenberger. 2000. The role of DOM sorption to mineral surfaces in the preservation of organic matter in soils. *Org. Geochem.* 31(7–8): 711–725. doi: 10.1016/S0146-6380(00)00046-2.
- Kaiser, K., and G. Guggenberger. 2007. Sorptive stabilization of organic matter by microporous goethite: Sorption into small pores vs. surface complexation. *Eur. J. Soil Sci.* 58(1): 45–59. doi: 10.1111/j.1365-2389.2006.00799.x.
- Karathanasis, A.D., P.A. Golrick, and R.I. Barnhisel. 1991. Soil formation on loess/sandstone toposequences in west-central Kentucky: II. Mineralogical

- relationships. *Soil Sci.* 152(3): 151–161. doi: 10.1097/00010694-199109000-00002.
- Keil, R.G., and L.M. Mayer. 2013. *Mineral Matrices and Organic Matter. Treatise on Geochemistry: Second Edition.* 2nd ed. Elsevier Ltd. p. 337–359
- Kentucky Climate Center. The Kentucky Mesonet at WKU. <http://www.kymesonet.org/>.
- Kentucky Division of Geospatial Data. KYGeoNet. Kentucky Div.
- Kleber, M., R. Mikutta, M.S. Torn, and R. Jahn. 2005. Poorly crystalline mineral phases protect organic matter in acid subsoil horizons. *Eur. J. Soil Sci.* 56(6): 717–725. doi: 10.1111/j.1365-2389.2005.00706.x.
- Koirala, D.R., F.R. Ettensohn, and M.L. Clepper. 2016. Eustatic and far-field tectonic control on the development of an intra-platform carbonate-shoal complex: upper tongue of the Tanglewood Member, Upper Ordovician Lexington Limestone, central Kentucky, U.S.A. *Sediment. Geol.* 345: 1–18. doi: 10.1016/j.sedgeo.2016.08.007.
- Lan, G., C. Liu, H. Wang, J. Cao, W. Tang, et al. 2021. Linking soil redistribution to soil organic carbon using ²¹⁰Pb_{ex} along different complex toposequences in a karst region, southwest China. *Catena* 202(September 2020): 105239. doi: 10.1016/j.catena.2021.105239.
- Lawrence, C., J. Harden, and K. Maher. 2014. Modeling the influence of organic acids on soil weathering. *Geochim. Cosmochim. Acta* 139: 487–507. doi: 10.1016/j.gca.2014.05.003.
- Lebedeva, M.I., and S.L. Brantley. 2013. Exploring geochemical controls on weathering and erosion of convex hillslopes: Beyond the empirical regolith production function. *Earth Surf. Process. Landforms* 38(15): 1793–1807. doi: 10.1002/esp.3424.
- Lerman, A., and L. Wu. 2006. CO₂ and sulfuric acid controls of weathering and river water composition. *J. Geochemical Explor.* 88(1-3 SPEC. ISS.): 427–430. doi: 10.1016/j.gexplo.2005.08.100.
- Li, S.L., D. Calmels, G. Han, J. Gaillardet, and C.Q. Liu. 2008. Sulfuric acid as an agent of carbonate weathering constrained by $\delta^{13}\text{CDIC}$: Examples from Southwest China. *Earth Planet. Sci. Lett.* 270(3–4): 189–199. doi: 10.1016/j.epsl.2008.02.039.
- Li, D., H. Ji, X. Wei, and S. Wang. 2016. Stable carbon and oxygen isotopes of terra rossa in Guizhou Province of China and their relationship to climate and ecology. *Environ. Earth Sci.* 75(13): 1–16. doi: 10.1007/s12665-016-5858-0.
- Li, Z., X. Xu, J. Zhu, C. Xu, and K. Wang. 2019. Effects of lithology and geomorphology on sediment yield in karst mountainous catchments. *Geomorphology* 343: 119–128. doi: 10.1016/j.geomorph.2019.07.001.
- Liu, Z., C. Groves, D. Yuan, and J. Meiman. 2004. South China Karst Aquifer Storm-Scale Hydrochemistry. *Ground Water* 42(4): 491–499.
- Long, D.T., A.L. Pearson, T.C. Voice, A.G. Polanco-Rodríguez, E.C. Sanchez-Rodríguez, et al. 2018. Influence of rainy season and land use on drinking water

- quality in a karst landscape, State of Yucatán, Mexico. *Appl. Geochemistry* 98(September): 265–277. doi: 10.1016/j.apgeochem.2018.09.020.
- Luo, M., Z. Chen, D. Yin, H. Jakada, H. Huang, et al. 2016. Surface flood and underground flood in Xiangxi River Karst Basin: Characteristics, models, and comparisons. *J. Earth Sci.* 27(1): 15–21. doi: 10.1007/s12583-016-0624-5.
- Lybrand, R.A., and C. Rasmussen. 2015. Quantifying Climate and Landscape Position Controls on Soil Development in Semiarid Ecosystems. *Soil Sci. Soc. Am. J.* 79(1): 104–116. doi: 10.2136/sssaj2014.06.0242.
- Malhi, Y., D.D. Baldocchi, and P.G. Jarvis. 1999. The carbon balance of tropical, temperate and boreal forests. *Plant, Cell Environ.* 22(6): 715–740. doi: 10.1046/j.1365-3040.1999.00453.x.
- Maranhão, D.D.C., M.G. Pereira, L.S. Collier, L.H.C. dos Anjos, A.C. Azevedo, et al. 2020. Pedogenesis in a karst environment in the Cerrado biome, northern Brazil. *Geoderma* 365(July 2019): 114169. doi: 10.1016/j.geoderma.2019.114169.
- Martini, J.A., and L. Mosquera. 1972. Properties of Five Tropepts in a Toposequence of the Humid Tropics in Costa Rica. *Soil Sci. Soc. Am. J.* 36(3): 473–477. doi: 10.2136/sssaj1972.03615995003600030030x.
- McKeague, J.A., J.E. Brydon, and N.M. Miles. 1971. Differentiation of Forms of Extractable Iron and Aluminum in Soils. *Soil Sci Soc Amer PROC* 35: 33–38. doi: 10.2136/sssaj1971.03615995003500010016x.
- McKeague, J.A., and J.H. Day. 1966. Dithionite- and Oxalate-Extractable Fe and Al as Aids in Differentiating Various Classes of Soils. *Can. J. Soil Sci.* 46(1): 13–22. doi: 10.4141/cjss66-003.
- Mevik, B.-H., R. Wehrens, and K. Hovde. 2020. pls: Partial Least Squares and Principal Component Regression. <https://cran.r-project.org/package=pls%0D>.
- Miller, J.A. 1990. Appalachian Plateaus and Interior Low Plateau Aquifers. *Gr. Water Atlas United States*. https://pubs.usgs.gov/ha/ha730/ch_g/G-text10.html.
- Milne, G. 1935. Some suggested units of classification and mapping, particularly of East African soils. *Soil Res.* 4(3): 183–198.
- Minasny, B., B.P. Malone, A.B. McBratney, D.A. Angers, D. Arrouays, et al. 2017. Soil carbon 4 per mille. *Geoderma* 292: 59–86. doi: 10.1016/j.geoderma.2017.01.002.
- Nerantzaki, S.D., and N.P. Nikolaidis. 2020. The response of three Mediterranean karst springs to drought and the impact of climate change. *J. Hydrol.* 591(July). doi: 10.1016/j.jhydrol.2020.125296.
- Newell, W.L. 2001. Contributions to the Geology of Kentucky: Physiography. <https://pubs.usgs.gov/pp/p1151h/physiography.html>.
- Ngo, T.T., A.P.H. Phan, C.F. Yam, and H.M. Lenhoff. 1982. Interference in Determination of Ammonia with the Hypochlorite-Alkaline Phenol Method of

- Berthelot. *Anal. Chem.* 54(1): 46–49. doi: 10.1021/ac00238a015.
- Nguyen, M.L., J.L. Goldfarb, A.F. Plante, B.L.T. Lau, and W.C. Hockaday. 2019. Sorption temperature and the stability of iron-bound soil organic matter. *Geoderma* 341(September 2018): 93–99. doi: 10.1016/j.geoderma.2019.01.040.
- Opsahl, S.P., M. Musgrove, and R.N. Slattery. 2017. New insights into nitrate dynamics in a karst groundwater system gained from in situ high-frequency optical sensor measurements. *J. Hydrol.* 546: 179–188. doi: 10.1016/j.jhydrol.2016.12.038.
- Panno, S. V., and D.E. Luman. 2018. Characterization of cover-collapse sinkhole morphology on a groundwater basin-wide scale using lidar elevation data: A new conceptual model for sinkhole evolution. *Geomorphology* 318: 1–17. doi: 10.1016/j.geomorph.2018.05.013.
- Parise, M., N. Ravbar, V. Zivanovic, A. Mikszewski, N. Kresic, et al. 2015. Hazards in Karst and Managing Water Resources Quality. *Karst Aquifers- Characterization and Engineering*. Springer. p. 601–687
- Paylor, R.L., and J.C. Currens. 2001. Karst Occurrence in Kentucky. : 1 sheet. <http://kgs.uky.edu/kgsweb/PubsSearching/PubResults.asp?dropmenu1=authors&data1=Paylor&limiter=AND&dropmenu2=&data2=&yearlmt=nopref&year2=&year3=&pubtype=all&pubSubject=&maps=&submit=submit+search+for+publications&searchtype=criteria#5077>.
- Paylor, R.L., L. Florea, M. Caudill, and J.C. Currens. 2003. GIS Coverage for the Karst Areas of Kentucky. *Kentucky Geol. Surv.* <https://www.uky.edu/KGS/gis/sinkpick.htm>.
- Pelletier, J.D., G.A. Barron-Gafford, H. Gutiérrez-Jurado, E.L.S. Hinckley, E. Istanbuluoglu, et al. 2018. Which way do you lean? Using slope aspect variations to understand Critical Zone processes and feedbacks. *Earth Surf. Process. Landforms* 43(5): 1133–1154. doi: 10.1002/esp.4306.
- Percival, H.J., R.L. Parfitt, and N.A. Scott. 2000. Factors Controlling Soil Carbon Levels in New Zealand Grasslands Is Clay Content Important? *Soil Sci. Soc. Am. J.* 64(5): 1623–1630. doi: 10.2136/sssaj2000.6451623x.
- Perrin, A.S., A. Probst, and J.L. Probst. 2008. Impact of nitrogenous fertilizers on carbonate dissolution in small agricultural catchments: Implications for weathering CO₂ uptake at regional and global scales. *Geochim. Cosmochim. Acta* 72(13): 3105–3123. doi: 10.1016/j.gca.2008.04.011.
- Phillips, J.D. 2016. Biogeomorphology and contingent ecosystem engineering in karst landscapes. *Prog. Phys. Geogr.* 40(4): 503–526. doi: 10.1177/0309133315624641.
- Ping, C.L., G.J. Michaelson, E.C. Packee, C.A. Stiles, D.K. Swanson, et al. 2005. Soil Catena Sequences and Fire Ecology in the Boreal Forest of Alaska. *Soil Sci. Soc. Am. J.* 69(6): 1761–1772. doi: 10.2136/sssaj2004.0139.
- Poeplau, C., A. Don, M. Dondini, J. Leifeld, R. Nemo, et al. 2013. Reproducibility of a soil organic carbon fractionation method to derive RothC carbon pools. *Eur. J. Soil*

- Sci. 64(6): 735–746. doi: 10.1111/ejss.12088.
- Prawito, P. 1996. Pedogenesis on Karst Toposequences in Kentucky.
- R Core Team. 2013. R: A language and environment for statistical computing. <http://www.r-project.org/>.
- Radulović, M.M. 2013. A new view on karst genesis. *Carbonates and Evaporites* 28(4): 383–397. doi: 10.1007/s13146-012-0125-2.
- Rasmussen, C., K. Heckman, W.R. Wieder, M. Keiluweit, C.R. Lawrence, et al. 2018. Beyond clay: towards an improved set of variables for predicting soil organic matter content. *Biogeochemistry* 137(3): 297–306. doi: 10.1007/s10533-018-0424-3.
- Rasmussen, C., J.D. Pelletier, P.A. Troch, T.L. Swetnam, and J. Chorover. 2015. Quantifying Topographic and Vegetation Effects on the Transfer of Energy and Mass to the Critical Zone. *Vadose Zo. J.* 14(11): 1–16. doi: 10.2136/vzj2014.07.0102.
- Rasmussen, C., M.S. Torn, and R.J. Southard. 2005. Mineral Assemblage and Aggregates Control Carbon Dynamics in a California Conifer Forest. *Soil Sci. Soc. Am. J.* 69(6): 1711–1721. doi: 10.2136/sssaj2005.0040.
- Reuter, R.J., and J.C. Bell. 2003. Hillslope Hydrology and Soil Morphology for a Wetland Basin in South-Central Minnesota. *Soil Sci. Soc. Am. J.* 67(1): 365–372. doi: 10.2136/sssaj2003.3650.
- Robinson, H.K., and E.A. Hasenmueller. 2017. Transport of road salt contamination in karst aquifers and soils over multiple timescales. *Sci. Total Environ.* 603–604: 94–108. doi: 10.1016/j.scitotenv.2017.05.244.
- Ruhe, R.V. 1960. Elements of the soil landscape. *Transactions of the 7th International Congress of Soil Science.* p. 165–170
- Ruhe, R.V., and P.H. Walker. 1968. Hillslope model and soil formation. I. Open systems. *Int Soc Soil Sci Trans* 4: 551–560.
- Scanlon, B.R., and J. Thrailkill. 1987. Chemical similarities among physically distinct spring types in a karst terrain. *J. Hydrol.* 89(3–4): 259–279. doi: 10.1016/0022-1694(87)90182-X.
- Schillaci, C., M. Acutis, L. Lombardo, A. Lipani, M. Fantappiè, et al. 2017. Spatio-temporal topsoil organic carbon mapping of a semi-arid Mediterranean region: The role of land use, soil texture, topographic indices and the influence of remote sensing data to modelling. *Sci. Total Environ.* 601–602: 821–832. doi: 10.1016/j.scitotenv.2017.05.239.
- Schimel, D.S., B.H. Braswell, E.A. Holland, R. McKeown, D.S. Ojima, et al. 1994. Climatic, edaphic, and biotic controls over storage and turnover of carbon in soils. *Global Biogeochem. Cycles* 8(3): 279–293. doi: 10.1029/94GB00993.
- Schimel, D., M.A. Stillwell, and R.G. Woodmansee. 1985. *Biogeochemistry of C, N,*

- and P in a Soil Catena of the Shortgrass Steppe. *Ecology* 66(1): 276–282.
<https://www.jstor.org/stable/1941328>%0AREFERENCES.
- Schoeneberger, P.J., D.A. Wysocki, E.C. Benham, and S.S. Staff. 2012. *Field book for describing and sampling soils*. 3rd ed. Natural Resources Conservation Service, Lincoln, NE.
- Schwertmann, U. 1958. The Effect of Pedogenic Environments on Iron Oxide Minerals. *Advances in Soil Science*. Springer New York, New York. p. 171–200
- Sedov, S., E. Solleiro-Rebolledo, S.L. Fedick, J. Gama-Castro, S. Palacios-Mayorga, et al. 2007. Soil genesis in relation to landscape evolution and ancient sustainable land use in the northeastern Yucatan Peninsula, Mexico. *Atti della Soc. Toscana di Sci. Nat. Mem. Ser. A* 112: 115–126.
- Sedov, S., E. Solleiro-Rebolledo, S.L. Fedick, T. Pi-Puig, E. Vallejo-Gomez, et al. 2008. Micromorphology of a Soil Catens in Yucatan: Pedogenesis and Geomorphological Processes in a Tropical Karst Landscape. *New Trends in Soil Micromorphology*. Springer Berlin Heidelberg, Berlin, Heidelberg. p. 19–37
- Sevil, J., F. Gutiérrez, C. Carnicer, D. Carbonel, G. Desir, et al. 2020. Characterizing and monitoring a high-risk sinkhole in an urban area underlain by salt through non-invasive methods: Detailed mapping, high-precision leveling and GPR. *Eng. Geol.* 272(April): 105641. doi: 10.1016/j.enggeo.2020.105641.
- Shang, C., and H. Tiessen. 2003. Soil organic C sequestration and stabilization in karstic soils of Yucatan. *Biogeochemistry* 62(2): 177–196. doi: 10.1023/A:1021123728639.
- Shang, C., and L.W. Zelazny. 2008. Selective Dissolution Techniques for Mineral Analysis of Soils and Sediments. In: Ulery, A.L. and Drees, L.R., editors, *Methods of Soil Analysis. Part 5. Mineralogical Methods*. Soil Science Society of America, Inc. p. 33–80
- Silva, M.B., L.H.C. do Anjos, M.G. Pereira, J.A. Schiavo, M. Cooper, et al. 2017. Soils in the karst landscape of Bodoquena plateau in cerrado region of Brazil. *Catena* 154: 107–117. doi: 10.1016/j.catena.2017.02.022.
- SINGER, A. 1993. Weathering patterns in representative soils of Guanxi Province, south-east China, as indicated by detailed clay mineralogy. *J. Soil Sci.* 44(1): 173–188. doi: 10.1111/j.1365-2389.1993.tb00443.x.
- Soil Survey Staff. 1999. *Soil Taxonomy: A Basic System of Soil Classification for Making and Interpreting Soil Surveys*. 2nd ed. USDA- National Resources Conservation Service.
- Soil Survey Staff. 2014. *Kellogg Soil Survey Laboratory Methods Manual (Soil Survey Staff and R. Burt, editors)*. 5th ed. U.S. Department of Agriculture, Natural Resources Conservation Service.
- Sollins, P., P. Homann, and B.A. Caldwell. 1996. Stabilization and destabilization of soil organic matter: mechanisms and controls. *Geoderma* 74: 65–105.

- Soukup, D.A., B.J. Buck, and W. Harris. 2008. Preparing soils for mineralogical analyses. *Methods of Soil Analysis. Part 5. Mineralogical Methods*. Soil Science Society of America, Madison, WI. p. 13–31
- Spence, J., and K. Telmer. 2005. The role of sulfur in chemical weathering and atmospheric CO₂ fluxes: Evidence from major ions, $\delta^{13}\text{CDIC}$, and $\delta^{34}\text{SSO}_4$ in rivers of the Canadian Cordillera. *Geochim. Cosmochim. Acta* 69(23): 5441–5458. doi: 10.1016/j.gca.2005.07.011.
- Stockmann, U., M.A. Adams, J.W. Crawford, D.J. Field, N. Henakaarchchi, et al. 2013. The knowns, known unknowns and unknowns of sequestration of soil organic carbon. *Agric. Ecosyst. Environ.* 164(2013): 80–99. doi: 10.1016/j.agee.2012.10.001.
- Stokes, T., P. Griffins, and C. Ramsey. 2010. Karst Geomorphology, Hydrology, and Management. In: Pike, R.G., Redding, T.E., Moore, R.D., Winkler, R.D., and Bladon, K.D., editors, *Compendium of Forest Hydrology and Geomorphology in British Columbia*
- Stolt, M.H., J.C. Baker, and T.W. Simpson. 1993a. Soil-Landscape Relationships in Virginia: I. Soil Variability and Parent Material Uniformity. *Soil Sci. Soc. Am. J.* 57(2): 414–421. doi: 10.2136/sssaj1993.03615995005700020022x.
- Stolt, M.H., J.C. Baker, and T.W. Simpson. 1993b. Soil-Landscape Relationships in Virginia: II. Reconstruction Analysis and Soil Genesis. *Soil Sci. Soc. Am. J.* 57(2): 422–428. doi: 10.2136/sssaj1993.03615995005700020023x.
- Stumm, W., and J.J. Morgan. 1996. *Aquatic Chemistry, Chemical Equilibria and Rates in Natural Waters*. 3rd ed. John Wiley & Sons, New York.
- Sullivan, P.L., G.L. Macpherson, J.B. Martin, and R.M. Price. 2019. Evolution of carbonate and karst critical zones. *Chem. Geol.* 527(June): 119223. doi: 10.1016/j.chemgeo.2019.06.023.
- Šušteršič, F., K. Rejšek, M. Mišič, and F. Eichler. 2009. The role of loamy sediment (terra rossa) in the context of steady state karst surface lowering. *Geomorphology* 106(1–2): 35–45. doi: 10.1016/j.geomorph.2008.09.024.
- Swift, R.S. 1996. Organic Matter Characterization. In: Sparks, D., Page, A., Helmke, P., Loeppert, R., Soltanpour, P.N., et al., editors, *Methods of Soil Analysis. Part 3. Chemical Methods*. p. 1011–1069
- Taylor, C.J., and E.A. Greene. 2005. Hydrogeologic Characterization and Methods Used in the Investigation of Karst Hydrology. In: Rosenberry, D.O. and LaBaugh, J.W., editors, *Field Techniques for Estimating Water Fluxes Between Surface Water and Ground Water*. U.S. Department of the Interior, U.S. Geological Survey
- Ticehurst, J.L., H.P. Cresswell, N.J. McKenzie, and M.R. Glover. 2007. Interpreting soil and topographic properties to conceptualise hillslope hydrology. *Geoderma* 137(3–4): 279–292. doi: 10.1016/j.geoderma.2006.06.016.
- Tipping, E. 1981. The adsorption of aquatic humic substances by iron oxides. *Geochim.*

- Cosmochim. Acta 45(2): 191–199. doi: 10.1016/0016-7037(81)90162-9.
- Torn, M.S., S.E. Trumbore, O.A. Chadwick, P.M. Vitousek, and D.M. Hendricks. 1997. Mineral control of soil organic carbon storage and turnover. *Nature* 389(6647): 170–173. doi: 10.1038/38260.
- Wada, K. 1989. Allophane and Imogolite. In: Dixon, J.B. and Weed, S.B., editors, *Minerals in Soil Environments*. 2nd ed. Soil Science Society of America, Inc. p. 1051–1087
- Waele, J. De. 2017. Karst Processes and Landforms. *Int. Encycl. Geogr. People, Earth, Environ. Technol.*: 1–13. doi: 10.1002/9781118786352.wbieg0968.
- Waltham, T., F.G. Bell, and M.G. Culshaw. 2005. *Sinkholes and Subsidence: Karst and Cavernous Rocks in Engineering and Construction*. Springer/ Praxis.
- Weary, D.J., and D.H. Doctor. 2014. *Karst in the United States: A Digital Map Compilation and Database*. : 23. doi: <http://dx.doi.org/10.3133/ofr20141156>.
- Weatherburn, M.W. 1967. Phenol-Hypochlorite Reaction for Determination of Ammonia. *Anal. Chem.* 39(8): 971–974. doi: 10.1021/ac60252a045.
- White, W.B. 1997. Thermodynamic equilibrium kinetics, activation barriers, and reaction mechanisms for chemical reactions in Karst Terrains. *Environ. Geol.* 30(1–2): 46–58. doi: 10.1007/s002540050131.
- Worthington, S.R.H. 2009. Diagnostic hydrogeologic characteristics of a karst aquifer (Kentucky, USA). *Hydrogeol. J.* 17(7): 1665–1678. doi: 10.1007/s10040-009-0489-0.
- Xu, S., Y. Lang, J. Zhong, M. Xiao, and H. Ding. 2020. Coupled controls of climate, lithology and land use on dissolved trace elements in a karst river system. *J. Hydrol.* 591(July): 125328. doi: 10.1016/j.jhydrol.2020.125328.
- Xu, Z., and C.Q. Liu. 2007. Chemical weathering in the upper reaches of Xijiang River draining the Yunnan-Guizhou Plateau, Southwest China. *Chem. Geol.* 239(1–2): 83–95. doi: 10.1016/j.chemgeo.2006.12.008.
- Yeomans, J.C., and J.M. Bremner. 1991. Carbon and nitrogen analysis of soils by automated combustion techniques. *Commun. Soil Sci. Plant Anal.* 22(9–10): 843–850. doi: 10.1080/00103629109368458.
- Yoo, K., R. Amundson, A.M. Heimsath, W.E. Dietrich, and G.H. Brimhall. 2007. Integration of geochemical mass balance with sediment transport to calculate rates of soil chemical weathering and transport on hillslopes. *J. Geophys. Res. Earth Surf.* 112(2). doi: 10.1029/2005JF000402.
- Yoo, K., and S.M. Mudd. 2008a. Discrepancy between mineral residence time and soil age: Implications for the interpretation of chemical weathering rates. *Geology* 36(1): 35–38. doi: 10.1130/G24285A.1.
- Yoo, K., and S.M. Mudd. 2008b. Toward process-based modeling of geochemical soil

- formation across diverse landforms: A new mathematical framework. *Geoderma* 146(1–2): 248–260. doi: 10.1016/j.geoderma.2008.05.029.
- Yoo, K., S.M. Mudd, J. Sanderman, R. Amundson, and A. Blum. 2009. Spatial patterns and controls of soil chemical weathering rates along a transient hillslope. *Earth Planet. Sci. Lett.* 288(1–2): 184–193. doi: 10.1016/j.epsl.2009.09.021.
- Yue, F.J., S.L. Li, S. Waldron, Z.J. Wang, D.M. Oliver, et al. 2020. Rainfall and conduit drainage combine to accelerate nitrate loss from a karst agroecosystem: Insights from stable isotope tracing and high-frequency nitrate sensing. *Water Res.* 186: 116388. doi: 10.1016/j.watres.2020.116388.
- Zádorová, T., V. Penížek, R. Vašát, D. Žížala, T. Chuman, et al. 2015. Colluvial soils as a soil organic carbon pool in different soil regions. *Geoderma* 253–254: 122–134. doi: 10.1016/j.geoderma.2015.04.012.
- Zhu, M., Q. Feng, Y. Qin, J. Cao, M. Zhang, et al. 2019. The role of topography in shaping the spatial patterns of soil organic carbon. *Catena* 176(January): 296–305. doi: 10.1016/j.catena.2019.01.029.
- Zhu, J., A.M. Nolte, N. Jacobs, and M. Ye. 2020. Using machine learning to identify karst sinkholes from LiDAR-derived topographic depressions in the Bluegrass Region of Kentucky. *J. Hydrol.* 588(May): 125049. doi: 10.1016/j.jhydrol.2020.125049.

VITA

Anne McGraw graduated from Penn State in December of 2018 with a BS in Environmental Resource Management, Soil Science Option. She began work on her MS at the University of Kentucky in August of 2019.